Raman amplification in optical communication systems

Kjær, Rasmus

Publication date:
2008

Document Version
Publisher's PDF, also known as Version of record

Raman amplification in optical communication systems

Rasmus Kjær

Ph.D. thesis

20. June 2008

DTU Fotonik
Department of Photonics Engineering

Technical University of Denmark

Abstract

In this thesis, fiber Raman amplifiers (FRAs) are investigated with the purpose of identifying new applications and limitations for their use in optical communication systems.

To better understand the dynamics, gain and noise limitations of the amplifier, a numerical amplifier model is developed. The model is used to predict the performance of the amplifier in both static and dynamic cases and its results are shown to agree well with experimental amplifier measurements.

Due to its high Raman gain efficiency and large deployment numbers, dispersion compensating fiber (DCF) is a highly suitable Raman gain medium and new applications of so-called dispersion compensating Raman amplifiers (DCRAs) are presented. These applications are: Terminal dispersion compensation using DCRAs, the extension of the dynamic and flat gain range of a commercial erbium-doped fiber amplifier (EDFA) to support longer spans, and the use of a hybrid wide-band DCRA/EDFA to obtain 60 nm gain bandwidth, noise figure of less than 4.5 dB and a total output power of 22 dBm.

To extend the reach of future access networks, a long-reach passive optical network (PON) architecture is proposed and theoretically and experimentally evaluated. To compensate the fiber loss in the long-reach PON link, distributed Raman amplification (DRA) is used and different pumping schemes and their effect on the maximum reach and channel capacity are evaluated using a numerical model. A 120 km bidirectional link with sufficient output power for PON applications and no with additional penalty due to the bidirectional traffic is experimentally demonstrated. The dynamic properties of the PON link are tested with burst-mode traffic and the system is found to be a promising candidate for future long-reach access PONs with burst-mode traffic.

Inter-channel crosstalk in saturated fiber amplifiers and the resulting output transients is a serious issue, particularly in high-speed (e.g. 40 Gbit/s) and reconfigurable networks. Output power transients can lead to burst-errors during detection and in the worst case cause damage to vital system components. A new all-optical method for mitigating transients on a channel level is presented. The method is optimized using a numerical model and is simultaneously demonstrated on four 40 Gbit/s wavelength division

multiplexed (WDM) channels. The result on the transient-induced channels is a sensitivity improvement in excess of 5 dB.

Resumé

I denne afhandling undersøges fiberbaserede Raman-forstærkere (FRAs) med henblik på at identificere både deres begrænsninger og nye anvendelsesmuligheder i optiske kommunikationssystemer.

En numerisk forstærkermodel er blevet udviklet for bedre at forstå forstærkerens dynamik, dens gain- og støjbegrænsninger. Modellen bruges til at forudsige forstærkerens statiske og dynamiske egenskaber, og det eftervises at dens resultater er i god overensstemmelse med eksperimentelle forstærker målinger.

Dispersions-kompenserende fiber (DCF) er på grund af sin store udbredelse og fiberens høje Raman gain effektivitet et meget velegnet Raman gainmedium. Tre nye anvendelser af den såkaldte dispersions-kompenserende Raman-forstærker (DCRA) præsenteres, og disse er: Terminal dispersionskompensering vha. en DCRA, forlængelse det dynamiske område af en kommerciel Erbium-doteret fiberforstærker (EDFA), samt brugen af en hybrid bredbånds-DCRA/EDFA med 60 nm båndbredde, et støjtal under 4,5 dB og en samlet udgangseffekt på 22 dBm.

Med henblik på at forlænge rækkevidden af fremtidige access-netværk foreslås en ny arkitektur for såkaldte langdistance passive optiske netværk (PON). Dette system evalueres både teoretisk og eksperimentelt. Distribueret Raman-forstærkning bruges i PON-forbindelsen til at kompensere for fibertabet. Udvalgte pumpekonfigurationer, samt disses indvirkning på den maksimale rækkevidde og antal kanaler i systemet, undersøges numerisk. En bidirektionel 120 km fiberforbindelse demonstreres eksperimentelt uden at der observeres ekstra forringelse af modtagerfølsomheden p.g.a. den bidirektionelle trafik. De dynamiske egenskaber af PON-forbindelsen testes med forstyrrende trafik og som konklusion vurderes systemet at være en lovende kandidat til fremtidige langdistance access PONs med dynamisk trafik.

Krydstale mellem to eller flere kanaler i mættede fiberforstærkere kan medføre transienter i udgangseffekten, hvilket kan være et stort problem i rekonfigurérbare og højhastigheds- (f.eks. 40 Gbit/s) netværk. Effekttransienter kan medføre pludselige fejl i modtagelsen af signalet og i værste fald kan transienterne medføre beskadigelse af vitale komponenter. Her præsenteres en ny, rent optisk metode til at udbedre signaler, der er blevet forringet p.g.a. transienter. Metoden optimeres vha. en numerisk model og demonstreres samtidigt på fire 40 Gbit/s kanaler. Modtagerens følsomhed forbedres

med mere end 5 dB efter brug af metoden.

Preface

This project has been conducted at DTU Fotonik, Department of Photonics Engineering at the Technical University of Denmark and OFS Fitel Denmark ApS from June 2005 to May 2008. The project is co-sponsored by DTU Fotonik, OFS Fitel Denmark and Photonics Academy Denmark and has been supervised by Prof. Palle Jeppesen and Ass. Prof. Leif K. Oxenløwe from DTU Fotonik and manager Bera Pálsdóttir from OFS Fitel Denmark.

During the last three years, I have been surrounded by a large number of smart and competent people who have contributed to this work. First of all, I would like to extend my sincere gratitude to the great team of supervisors on this project, Palle, Bera and Leif. Thanks for all your encouragement and support throughout this project and for the great feedback I have received, during the writing of this thesis. Regarding the thesis, I would also like to thank Christophe Peucheret, Anders Clausen and Idelfonso Tafur Monroy for their good inputs and high-level proof-reading of several chapters.

I would also like to send a special acknowledgment to my office mates, Hans Christian Mulvad Hansen and Jesper Bevensee Jensen, for providing an enjoyable working atmosphere and good friendship. Also thanks to present and former colleagues of the former Systems and Nanophotonics group at DTU Fotonik. In particular, I would like to mention Jeppe, Torger, Yan, Emir, Ji, Michael, Darko, Jorge, Beata, Haiyan, Lara, Alexey and Tim.

Throughout this project, I have been provided my own office space at OFS, although my presence did perhaps not always earn it. I have always felt welcome at OFS and it has been a great experience to learn from some the true experts in the field of fibers and fiber-optic systems, like Lars Grüner-Nielsen, Carsten G. Jørgensen and Torben Veng. I would also like to extend a special thanks to Peter B. Gaarde for being a great friend and colleague at OFS.

I have been fortunate to participate in several conferences around the world and also had the pleasure of good company along the way. In particular, I would like to thank Filip Öhman, Christian Romer Rosberg, Idelfonso Tafur Monroy and Yi An for good times, and also the Idella foundation for supporting my trip to China.

Finally, thanks my lovely wife Annemarie and my two boys, Marius and Jonas, for all your love and support!

Rasmus Kjær
Kgs. Lyngby, 20. June 2008

Contents

1. Introduction

1.1. Background and motivation

Since the deployment of the first trans-Atlantic fiber-optic telephone cable, *TAT-8*, in 1988 [1], fiber-based optical communications has paved the way for high-speed communications over long distances, the Internet and the free flow of information that characterizes today's information society. In its time, TAT-8 was a revolution in telecommunications and consisted of two fiber pairs that each could carry 295 Mbit/s of traffic ($295 \cdot 10^6$ bits per second), corresponding to $\sim 40,000$ simultaneous phone calls or ten times that of the last deployed copper cable [2]. All along the 6430 km submarine cable, power-supplied regenerator stations were positioned with 40 km spacing in order to compensate for the fiber loss by electro-optic regeneration of the signal [3].

Twenty years later, as these lines are written, a consortium of six international telephone companies are deploying the so-called *Trans-Pacific Express*, a 17,700 km cable which will establish a direct communication link, for the first time, between China, South Korea, Taiwan and the United States [4]. The link is scheduled to be in operation in August 2008, just in time for the opening of the 2008 Olympic Games in Beijing. It will initially be configured to handle traffic at 1.28 Tbit/s, or 62 million simultaneous phone calls, but the system will have a design capacity up to 5.12 Tbit/s ($5.12 \cdot 10^{12}$ bits per second). Needless to say, this rate of development could hardly have been foreseen in 1988 and indeed the capacity of TAT-8, which was scheduled to be filled by the year 2000, was already filled in 1990 [5].

Most people are somehow affected, on a daily basis, by the technological advances in optical communications, which have occurred over the last two decades. Whenever we use the phone or Internet to communicate with colleagues in our daily work, whenever we share movies, music or pictures with friends and family, or whenever we watch a high-definition transmission of a football match from the Euro2008 — the information is brought to us through fiber-optic cables. The total rate of traffic is expected to increase significantly in the coming years, as more user bandwidth is made available and millions of homes will be connected through fiber-to-the-premises (FTTP) solutions [6]. Many people are not aware of it, but optical communications has profoundly changed the way we access

and share information.

1.1.1. The role of optical amplifiers

The emergence of efficient broadband optical amplifiers, in particular the erbium-doped fiber amplifier (EDFA), has more than anything spurred the enormous increase in capacity and reach in telecommunication networks, in recent years [7]. The large gain bandwidth of these amplifiers has enabled wavelength division multiplexed (WDM) technology, which is used to increase the single fiber capacity by adding many parallel channels positioned side-by-side on a wavelength grid. Furthermore, the low noise figure of these amplifiers has omitted the need for costly periodic electro-optic regeneration and today, a single state-of-the-art EDFA can simultaneously amplify close to a hundred 10 Gbit/s WDM channels[1], corresponding to ~ 1 Tbit/s worth of traffic, without electro-optic conversion or any use of high-speed electronics.

However, as a result of the large bandwidth of modern single-mode silica fibers, the capacity of today's optical communication systems is in reality limited by the bandwidth of the used optical amplifiers [6]. Similarly, the reach of present systems is also limited by the noise contributed by the used amplifiers, combined with nonlinear effects from transmission [8]. Furthermore, the tendency to make increasing use of meshed and reconfigurable networks impose new stringent requirements on the dynamic performance of modern amplifiers to sufficiently reduce inter-channel crosstalk and prevent the appearance of output power transients [9]. As such, new ways to extend the bandwidth, improve the noise and dynamic properties of present-day amplifiers are constantly pursued.

The most widely used amplifier today is the EDFA, which is a discrete amplifier that can be used to amplify signals in the C-band (1530 nm–1565 nm) or L-band (1565 nm–1625 nm) [7]. Years of development and optimization, since the early nineties, means that the EDFA technology is exploited very close to its fundamental limits. As such, the EDFA noise figure can be made very close to its quantum-limited value of 3 dB, with high power efficiency close to 80% and flat gain with less than 1 dB non-uniformity in its specified gain range [7]. It is therefore unlikely that new development in the EDFA design can dramatically improve performance of future systems.

[1] As an example, it is possible to fit 85 channels with 50 GHz channel spacing into the conventional band (C-band), which spans 35 nm, or roughly 4.4 THz.

1.1.2. Fiber Raman amplifiers

At the present time, the most promising technology for increasing the bandwidth and improving noise properties of today's systems is the *fiber Raman amplifier (FRA)* [6]. Raman amplification can be used to provide gain in the transmission fiber itself, a technique known as *distributed amplification*. This technique reduces the signal-to-noise ratio (SNR) degradation of the system, compared with a system that uses only discrete amplifiers. Furthermore, FRAs can provide gain in a bandwidth which is only limited by the available pump powers and wavelengths and using this technology, flat gain bandwidths up to 100 nm has been demonstrated [10]. Finally, these amplifiers also benefit from a very linear gain, which means that the FRA gain is less inclined to saturate and induce crosstalk between channels, when faced with high input powers, compared to EDFAs [11].

Like most technologies, FRAs also come with some drawbacks that should be taken into account, when the technology is evaluated. These include low power efficiency, safety issues related to having high optical powers in the fiber, as well as other sources of noise that are particular to FRAs, such as double Rayleigh backscattering (DRB), pump-mediated relative intensity noise (RIN) transfer and enhanced problems with nonlinearities, due to high path-average power in the fibers.

Today, Raman amplification is primarily used in the transmission fiber, and in some cases also the dispersion compensating fiber (DCF), of long-haul systems (>1000 km) employing high bit rates of 10–40 Gbit/s [12, 13]. Depending on the application, the merits and drawbacks of FRAs can be more or less important. But if FRAs are to be used to dramatically improve the capacity and reach of today's systems, it is imperative to identify new ways to utilize this amplifier along with its main limitations in systems.

1.2. Aim of this project

In general terms, this project investigates the use of FRAs from an application perspective. The object is to identify new areas where FRAs may find use, identify how these amplifiers can be exploited to their maximum limits and determine when it is advantageous to use this amplifier in place of another type. In other words, we seek to answer some of the questions related to "how", "where" and "when" FRAs can be advantageously used in a future system context.

Specifically, the research on FRAs performed in this project can be summarized in three main topics, namely:

- Limitations and applications of dispersion compensating Raman am-

plifiers (DCRAs).

- The use of Raman amplification in long-reach passive optical networks (PONs) for FTTP applications.
- Inter-channel transient crosstalk and how to remedy these unwanted effects.

Finally, it has been a goal to obtain a good physical understanding of gain and noise properties of FRAs and, hopefully, to provide a clear and self-consistent description of the amplifier in this thesis.

1.3. Structure of the thesis

The thesis chapters are organized as follows. Chapter 2 is a general introduction to Raman amplification in optical fibers. The first part of the chapter describes the fundamental amplifier gain, important noise sources and how the amplifiers are used in system contexts. The middle part is a description of a numerical FRA model, which has been developed in this project. In the final part of the chapter, the model is used to describe the static amplifier performance in terms of gain and noise, under various conditions. Chapter 3 is devoted to dispersion compensating Raman amplifiers (DCRAs) and how they can be used either as stand-alone amplifier/dispersion-compensating units, or in hybrid combinations with EDFAs. The main focus of the chapter is on three different DCRA applications which have been investigated over the course of this project. Chapter 4 focuses on the use of distributed Raman amplification to extend the reach of future access systems, the so-called long-reach PONs. Model results are used to predict the maximum reach and capacity of the proposed system and the results are supplemented by experimental demonstrations of the reach and dynamic performance of the system. Chapter 5 investigates the topic of transient impairments resulting from inter-channel crosstalk in EDFAs or FRAs. The chapter describes how transients are created and shows that this crosstalk can seriously impair the system performance. The last part of the chapter introduces a new all-optical method to equalize amplifier transients. The design of the equalizer is optimized using a numerical model and its functionality is experimentally demonstrated on 40 Gbit/s channels, which have been impaired by crosstalk in an EDFA. Chapter 6 concludes the thesis and provides a view on the future of Raman amplification in the context of optical communications.

The thesis is accompanied by five appendices, which can be of help during the reading. A short introduction to these is therefore in place. Appendix A contains figures in which the developed numerical amplifier model is directly

compared and validated with experimental data and a reference amplifier model. Appendix B contains plots of the different fiber data used in the numerical model. Appendix C lists the used acronyms and appendix D lists the fundamental constants, variables and symbols used in this thesis. Finally, appendix E lists the publications obtained by the author in collaboration with the co-authors. Enjoy the reading!

2. Raman amplification in optical fibers

In this chapter, Raman amplifiers based on silica fibers are introduced in relation to their use in optical communication systems. The principle of Raman scattering in optical fibers is presented along with a discussion of important applications and issues related to distributed and lumped Raman amplifiers. To study the static and dynamic properties of fiber Raman amplifiers (FRAs) throughout this thesis, a numerical amplifier model is developed and its features and limitations are described in detail in this chapter. Using the model, static properties of FRAs are modeled and discussed in relation to the amplifier design.

Section 2.1 introduces the basic principles of Raman amplifiers. These include Raman scattering, the Raman gain efficiency and the small-signal regime, in which the input powers are low and simple equations for the gain and optimum fiber length can be found. Section 2.2 describes the basic design and typical applications of Raman amplifiers. Here, the most important limitations and issues of these amplifiers are also discussed. Section 2.3 introduces a developed numerical amplifier model that can be used to model the static and dynamic behavior of Raman amplifiers. In section 2.4, the calculated results of gain, noise figure and multi-path interference (MPI) are presented and discussed in relation to the amplifier design.

2.1. Basic principles

This section presents some basic principles related to Raman amplification in optical fibers, in particular, Stokes scattering and the Raman gain efficiency, which represents the fiber's ability to provide Raman gain.

2.1.1. Raman scattering

The ability of light to scatter inelastically on a molecular structure (gas, liquid or solid) and exchange energy with the material was discovered by the Indian physicist C. V. Raman in 1928 [14]. Independently and around the same time, the effect was also observed by the Russian physicists G.

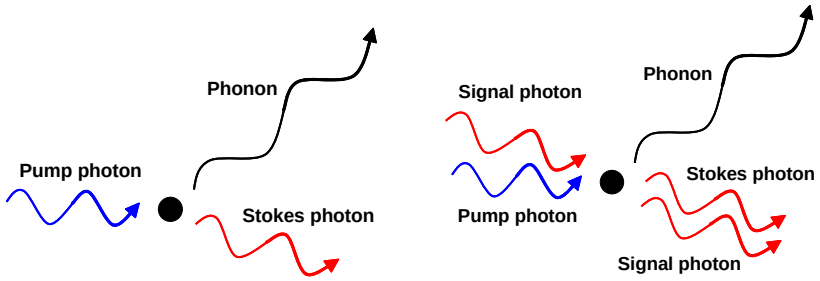

(a) Spontaneous emission (b) Stimulated emission

Figure 2.1.: Stokes scattering on a molecule.

Landsberg and L. Mandelstam [15]. The effect[1] is now known as *Raman scattering* and causes an incoming photon to be either red-shifted (known as the Stokes shift) or blue-shifted (known as anti-Stokes shift) by interaction with the medium. In either case, a fraction of the photon energy is absorbed or emitted by the material in terms of molecular vibrations (heat), also referred to as *phonons*. Raman scattering can occur in all materials, but in silica glass the dominant Raman transitions are due to the bending motion of the Si-O-Si bond [16].

Because Raman scattering is inelastic, the molecule will decay to a vibrational level that is different from its initial state. Stokes Raman scattering occurs when the final energy level of the molecule is higher than the initial level, while anti-Stokes Raman scattering occurs when the final energy level is lower than the starting level. Stokes scattering is much more common than anti-Stokes scattering because at any given time an electron in the most common temperature range is most likely to be in its lowest energy state, in accordance with the Boltzmann distribution [17]. Raman anti-stokes scattering is therefore unimportant in the context of optical communications [16].

For the Stokes shift, energy conservation yields

$$h\nu_s = h\nu_p - E_{phonon} \tag{2.1}$$

where ν_p and ν_s are the frequency of the pump and Stokes photon, respectively, E_{phonon} is the energy of the emitted phonon and h is Planck's constant. Stokes scattering can occur spontaneously, as shown in Fig. 2.1 (a). An incident pump is scattered on a molecule which causes a red-shift of the

[1] Raman scattering refers to the inelastic photon scattering with optical phonons, while a similar type of scattering, *Brillouin scattering*, refers to photon scattering with the acoustic phonons of the medium.

photon and simultaneously emits a phonon. The process can also be stimulated by the presence of a signal photon with a frequency equal to the Stokes frequency ν_s, as shown in Fig. 2.1 (b). Aside from contributing to the noise in Raman amplifiers and lasers, spontaneous Raman scattering is widely used in sensing and spectroscopy applications [18, 19]. The most important application of stimulated Raman scattering is to provide optical gain and as such, it is the key process in optical Raman amplifiers and lasers.

2.1.2. Raman gain efficiency

If contributions from the intrinsic loss and Rayleigh scattering are neglected, the growth of stimulated Raman scattered signal intensity in an optical waveguide grows proportionally with the pump and signal intensity and the *Raman gain coefficient*, γ_R, so that[2]

$$\frac{dI_s}{dz} = \gamma_R I_p I_s \tag{2.2}$$

where I_p and I_s are the intensities of the pump and Stokes waves, respectively.

γ_R describes the probability of stimulating Raman scattering during propagation in a nonlinear medium. γ_R depends on the pump-signal frequency detuning, $\Delta\nu = \nu_p - \nu_s$ as well as on the material composition of the waveguide. Vitreous silica, which is the main constituent of the optical fibers discussed in this context, has a main peak in its Raman cross-section at 440 cm^{-1}, or 13.2 THz. The use of different types of core dopants, such as germanium, can cause γ_R to vary significantly. The Raman cross section of germanium has a peak at 420 cm^{-1}, or 12.6 THz, and the value is more than 7 times higher than that of silica [21]. Because of its high γ_R value and peak close to that of silica, germanium is commonly used to increase the Raman gain response of silica fibers.

In order for stimulated emission to be generated, it is necessary that the Stokes and pump waves overlap in both time and space. For single-mode fibers, the power is found by integrating the intensity across the fiber cross section. By assuming the intensity to be invariant with the rotational angle, the power P can be defined as

$$P = 2\pi \int_{r=0}^{\infty} I(r) \cdot r \, dr \tag{2.3}$$

[2] Please note that equation (2.2) describes the intensity wave in a so-called retarded time frame [20] that follows the wave at the group velocity v_g. The frame is obtained by substituting $t = t' - z/v_g$ into the original wave equation $I(t', z)$, where t is the time in a moving reference frame. The retarded time frame is used throughout this chapter.

where r is the fiber radius. To take into account the spatial overlap of the two modes, eq. (2.2) should be integrated over the cross-section of the fiber to give the rate equation for the Stokes power P_s, i.e.

$$\frac{dP_s}{dz} = P_p P_s g \tag{2.4}$$

where P_p is the pump power and g is the *Raman gain efficiency*. By assuming that γ_R does not vary with radius, the Raman gain efficiency may be expressed as [22]

$$g = \gamma_R \frac{\int_{r=0}^{\infty} I_s(r)\, I_p(r)\, r\, dr}{2\pi \int_{r=0}^{\infty} I_s(r)\, r\, dr \int_{r=0}^{\infty} I_p(r)\, r\, dr} = \frac{\gamma_R}{A_{eff}^R} \tag{2.5}$$

In (2.5), the Raman gain efficiency is seen to contain both a material contribution from γ_R, as well as a contribution from the Raman spatial overlap between the two modes, A_{eff}^R. If the spatial distributions of the two modes are close to identical, the Raman spatial overlap can be approximated with the effective mode area, A_{eff} and the Raman gain efficiency becomes [23]

$$g \approx \frac{\gamma_R}{A_{eff}} \tag{2.6}$$

where A_{eff} is similar to the effective core area of self-phase modulation [20]. Hence, a large g can be obtained either by a large γ_R, or by a small A_{eff}. As an example of the former, coefficients of $g = 55$ $\mathrm{W^{-1}km^{-1}}$ has been reported using tellurite (TeO_2) fibers [24]. Ultra-small A_{eff} can be realized using novel designs of highly non-linear photonic crystal fibers (HNL-PCFs). As an example of this, a pure silica holey fiber with an effective area of 2.85 $\mu\mathrm{m}^2$ at 1550 nm and an experimentally expected γ_R value of 7.6×10^{-14} m/W has been demonstrated [25]. According to (2.6), these values give rise to a gain efficiency value of $g \approx 27$ $\mathrm{W^{-1}km^{-1}}$.

Fig. 2.2 shows measured values of the Raman gain efficiency for five different transmission fibers (TFs) and dispersion compensating fibers (DCFs) and as a function of the pump-signal detuning $\Delta\nu$. For all fibers, g is seen to peak between 13.0 THz and 13.3 THz. The TFs include standard single-mode fiber (SSMF), as well as two types of non-zero dispersion-shifted fiber (NZDSF), namely TrueWave®RS (TW-RS) and TrueWave®REACH (TW-REACH). These fibers show moderate peak values of g from 0.4 $\mathrm{W^{-1}km^{-1}}$ for SSMF up to 0.7 $\mathrm{W^{-1}km^{-1}}$ for TW-RS.

For the two DCFs compared in Fig. 2.2, g is considerably higher with peak values of 2.4 $\mathrm{W^{-1}km^{-1}}$ (DCF for SSMF) and 3.5 $\mathrm{W^{-1}km^{-1}}$ (DCF for TW-RS). The high g of DCF is both due to a high germanium (GeO_2)

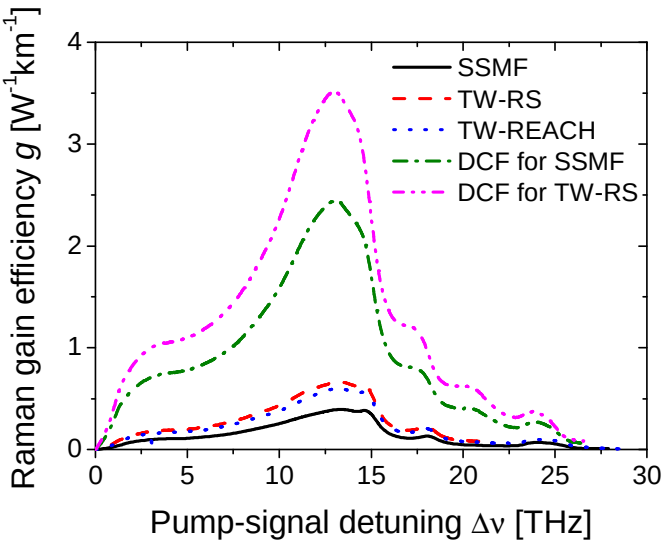

Figure 2.2.: Raman gain efficiency for different types of dispersion compensating fibers and transmission fibers. The parameters are measured at OFS Fitel Denmark ApS.

doping concentration in the core, as well as a small A_{eff} (see table 2.1 on page 12), both of which increase the nonlinearity of the fiber [26].

For easy reference, table 2.1 summarizes some important parameters of the fibers used in this project. These include three types of TF, two types of DCF and a single highly nonlinear fiber (HNLF). All parameters are specified at 1550 nm, except the pump loss $\alpha_{dB,1450}$, which is at 1450 nm. These are: The intrinsic fiber loss α_{dB}, the chromatic dispersion coefficient D, the dispersion slope S, the mode effective area A_{eff}, the Raman gain efficiency g and the Rayleigh back-scattering coefficient φ.

SSMF is the standard transmission fiber (G.652), designed for low loss and relatively high dispersion. TW-RS is a NZDSF (G.655) designed with low dispersion and slope for metro and long-haul transmission. TW-REACH is a NZDSF (G.656) with medium dispersion and optimized for long-haul transmission and use with distributed Raman amplification (DRA). Compared with G.652 fibers like SSMF, the G655 and G.656 has a more complex refractive index profiles, characterized by a larger GeO_2 core doping and a smaller effective mode area A_{eff}, involving strong differences in terms of Raman gain efficiency g, noise figure, and double Rayleigh backscattering (DRB) noise generation [27]. DRB explained further in section 2.2.2.

Name	**Type**	$\alpha_{dB,1550}$ [dB/km]	$\alpha_{dB,1450}$ [dB/km]	D $\left[\frac{\text{ps}}{\text{nm}\cdot\text{km}}\right]$	S $\left[\frac{\text{ps}}{\text{nm}^2\cdot\text{km}}\right]$	A_{eff} $[\mu\text{m}^2]$	g $\left[\frac{1}{\text{W}\cdot\text{km}}\right]$	φ $[10^{-8}\text{m}^{-1}]$
SSMF	TF	0.19	0.23	16.5	0.058	82	0.39	5.7
TW-RS	TF	0.20	0.25	4.5	0.045	52	0.71	9.4
TW-REACH	TF	0.20	0.25	7.1	0.042	55	0.63	8.2
DCF for SSMF	DCF	0.41	0.54	-120	-0.422	21	2.45	36
DCF for TW-RS	DCF	0.58	0.75	-160	-1.600	14	3.50	56
HNLF	HNLF	0.8	-	~ 0	0.019	12	11.0*	-

Table 2.1.: Parameters of fibers used in this project.
Taken from model parameters and [26–30]. (*)Nonlinear coefficient γ.

2.1.3. Small-signal approximation

If both gain and the intrinsic loss of the fiber is taken into account, the basic propagation equations for the power of a co-propagating signal[3] and pump in a fiber are

$$\frac{dP_s^+}{dz} = \left(gP_p^+ - \alpha_s\right) P_s^+ \tag{2.7}$$

$$\frac{dP_p^+}{dz} = -\left(\frac{\lambda_s}{\lambda_p} gP_s^+ + \alpha_p\right) P_p^+ \approx -\alpha_p P_p^+ \quad \text{for} \quad P_s^+ \ll \alpha_p/g \tag{2.8}$$

In (2.7) and (2.8), α_s and α_p is the fiber intrinsic loss coefficient at the signal and pump wavelengths, λ_s and λ_p, respectively. The ratio λ_s/λ_p takes into account the energy difference between the signal and pump photon.

If the signal power P_s at all positions satisfies the *small-signal condition*, $P_s \ll \alpha_p/g$, the gain term in eq. (2.8) can be neglected and the solution for the pump simplifies to $P_p^+(z) = P_p^+(0)\exp[-\alpha_p z]$, where $P_p^+(0)$ is the pump input power. Inserting this solution into (2.7) yields the *small-signal solution* for P_s^+ at the fiber output, $z = L$

$$P_s^+(L) = P_s^+(0)\exp\left[gP_{p,z=0}^+ L_{eff} - \alpha_s L\right] \tag{2.9}$$

where L is the length and L_{eff} is the *Raman effective length* of the fiber. The latter is given by

$$L_{eff} = \frac{1 - \exp[-\alpha_p L]}{\alpha_p} \tag{2.10}$$

and determines the effective interaction length of the pump. For a lossless fiber, L would be equal to L_{eff}, while for a real fiber L_{eff} is always smaller than L. Eq. (2.9) is seen to provide a way to estimate g from easily measurable quantities, such as the signal input and output power, the fiber length, the fiber loss at the signal and pump wavelength and the pump input power [26].

When the length of a short fiber is increased, the small-signal gain will increase up to a certain optimum fiber length, L_{opt}, whereafter it will gradually decrease , as the fiber loss starts to dominate over the gain, for long fiber lengths. L_{opt} can be found by differentiation of the exponential in (2.9)

[3] A note on the terminology: For the remainder of the thesis, the "Stokes beam" will be referred to as "signal beam", or simply "signal", to imply that we are dealing with the amplification of communication channels.

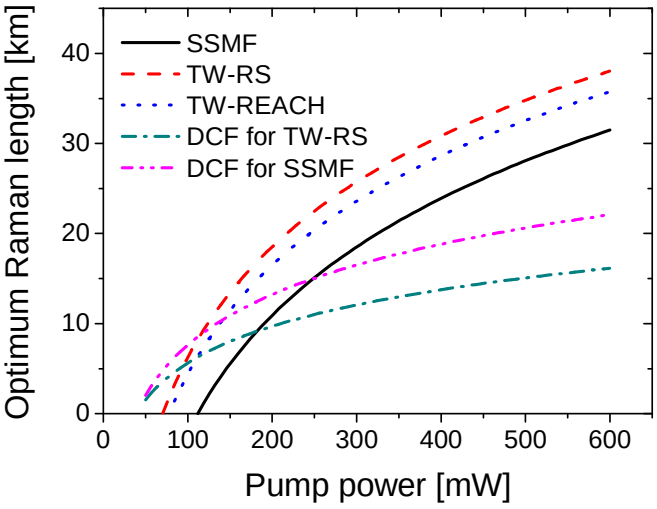

Figure 2.3.: Optimum Raman length of various fibers vs. pump power.

and setting it equal to zero, i.e.

$$L_{opt} = \frac{1}{\alpha_p} \ln \left[\frac{g_s}{\alpha_s} P_{p,in} \right] \tag{2.11}$$

In Fig. 2.3 L_{opt} is plotted vs. pump power for the same fibers plotted in Fig. 2.2. In general, L_{opt} increases with pump power and with a slope given by the inverse pump loss, $dL_{opt}/dP_{p,in} = 1/\alpha_p$. Due to lower pump loss in the transmission fibers, L_{opt} is larger for the transmission fibers than for the DCFs.

2.1.4. Properties of the Raman gain

Unlike other optical amplifiers, such as the erbium-doped fiber amplifier (EDFA) and the semiconductor optical amplifier (SOA), the gain of the FRA stems from a non-resonant process and does not depend on the specific wavelength of the optical signal, but instead on the pump-signal detuning $\Delta\nu$. This very special ability allows the gain to be wavelength tunable through tuning of the pump wavelength and this is one of the main attractions of Raman amplifiers. By combining pumps at several wavelengths, Raman amplifiers with more than 100 nm gain bandwidth has been demonstrated [10, 31].

Raman scattering is an ultra-fast process which occurs on the order of 100 fs [32]. Because of this, high frequency pump fluctuations due to laser relative intensity noise (RIN) can be transferred to the signal through the

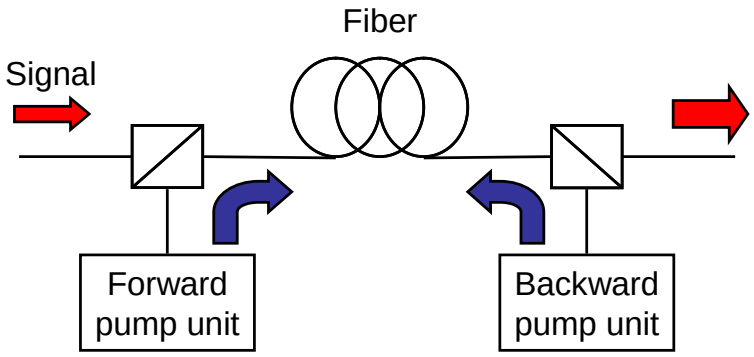

Figure 2.4.: General schematic of a bidirectionally pumped fiber Raman amplifier.

gain. In practice, the bandwidth of the transferred noise is limited by pump-signal walk-off, due to dispersion in the fiber or because the pump is counter-propagating to the signal [33]. For the bit rates found in this work, the Raman response can be assumed to be instantaneous.

The Raman gain is polarization dependent and is highest when the pump and signal are co-polarized. For a signal and pump with orthogonal polarizations, the gain is reduced by approximately an order of magnitude [16]. To overcome the issue of polarization-dependent gain, depolarized pumps are often used.

2.2. Design and applications

This section focuses on the design and applications of FRAs in optical communication systems. At the end of the section, important limitations and issues of this technology are discussed.

2.2.1. Distributed and lumped amplifiers

Raman amplifiers are generally divided into two categories, namely, distributed and lumped amplifiers. “Distributed” amplification refers to using the transmission fiber for amplification, while “lumped”, or “discrete”, amplifiers uses a fiber medium that is localized before or after transmission to fully or partially compensate for the transmission loss. When DCF is used as gain medium, it is referred to as a dispersion compensating Raman amplifier (DCRA). This type of amplifier is the topic of chapter 3.

A general layout of a bidirectionally pumped FRA is shown in Fig. 2.4. The signal enters from the left and is combined with the forward propagating pump in a coarse wavelength division multiplexer (CWDM). In the fiber,

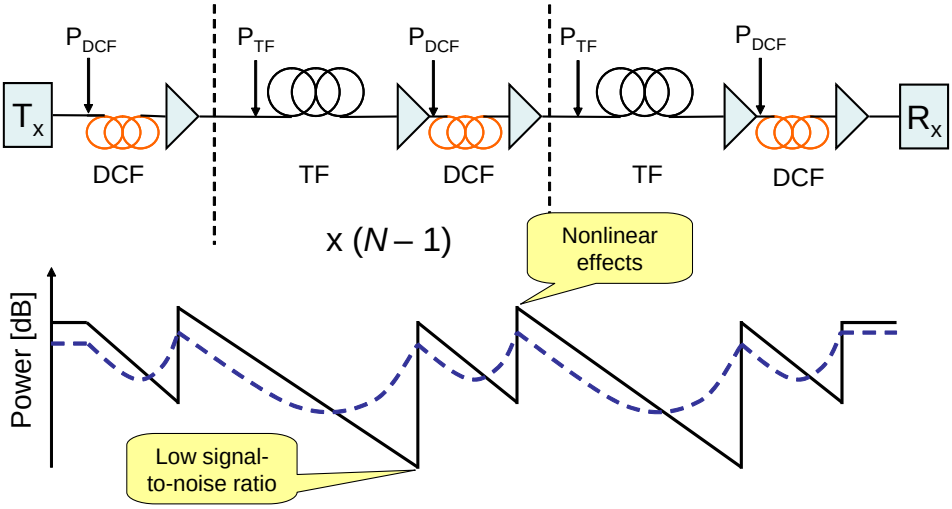

Figure 2.5.: Optical communication system with N spans and pre-, inline- and post-compensation of dispersion using DCF. Power profiles of the discrete- and Raman-amplified systems are shown with the solid and dashed line, respectively.

the signal is amplified by the forward and backward propagating pump and is separated from the pump in the output CWDM. Design parameters of the FRA include the fiber type, the fiber length, the pump power and the ratio of forward and backward pumping. These parameters and their influence on the performance of the amplifier are further discussed in section 2.4.

As an example of how Raman amplification can be used to improve the transmission performance in optical communications, a general point-to-point system link is shown in Fig. 2.5. The system consists of N spans of TF and the input power into each span is set to P_{TF}. To compensate for chromatic dispersion from the transmission fiber, the system includes DCF insertion points after the transmitter (T_X), between each span and before the receiver, a technique which is referred to as pre-, inline- and post-compensation of dispersion. In each TF and DCF span, intrinsic fiber loss will reduce the signal power along the length of the fiber. To obtain the highest possible signal-to-noise ratio (SNR) at the receiver (R_X), it is necessary to maintain as high a signal power as possible along the way, by re-amplifying the signal power periodically to compensate for the fiber loss.

In a system where only discrete amplifiers are used between the spans, the power variations along the fiber will be relatively large, as seen in Fig. 2.5 (black solid line). The high input powers into the span cause the impairments from nonlinearities to be high and the low signal power at the end of each span will limit the output SNR [34]. If the TF and DCF instead

are Raman-pumped to reduce the effective fiber loss, the power variations along the fiber will also be reduced, as seen in Fig. 2.5 (blue dashed line). The lower maximum power and higher minimum power of the distributed system are the reasons why this system is superior to a discrete amplifier system in terms of reducing impairments from nonlinearities and improving the output SNR.

In the last five years, Raman amplification has primarily found use in long-haul systems operating at bit rates of 10 Gbit/s and beyond [12, 13, 35] and trans-pacific transmission distances of 10.000 km in all-Raman amplified systems has been achieved at 40 Gbit/s [36]. The main reason for using FRAs in long-haul applications are that optical signal-to-noise ratio (OSNR) margins are more critical in these systems and DRA provides a way to improve the system noise figure. By increasing the bit rate, the OSNR margins decrease even further, due to a larger receiver bandwidth used in these systems [28].

Another important application is repeater-less systems, where practical issues prevent the use of repeaters in the field, e.g. when transmitting across large wastes or between islands. By using pure Raman pumping from the terminals, the repeater-less transmission distance can be greatly increased and up to 440 km of 10 Gbit/s transmission has been reported [37]. By using DRA along with a remote optically pumped amplifier (ROPA) up to 525 km has been achieved [38].

For lumped amplifiers, ultra-wide-band amplification is an important application and up to 100 nm bandwidth along with low noise figure has been achieved [31, 39]. These amplifiers are promising candidates for future wide-band systems and an example of such an amplifier design is presented in chapter 3.

2.2.2. Challenges

Compared to the EDFA, which is the most widely used amplifier in today's communication systems, the FRA may benefit from improved noise performance due to the distributed amplification, as well as the possibility of seam-less ultra-wide bandwidth. However, the FRA also suffers from several drawbacks. In particular, the power efficiency of the FRA is lower than that of the EDFA, where up to 80% efficiency can be achieved. Furthermore, EDFAs are capable of close-to quantum-limited noise figure of 3 dB and have very slow gain dynamics, which minimize fast pump-signal noise transfer and high frequency inter-channel crosstalk.

Pump lasers Compared to the pump lasers used in EDFAs, the requirements for Raman pump lasers are much more strict. The reasons for this are

several and will briefly be discussed in the following. The most important requirement for Raman pump lasers are stability, both in terms of power and wavelength. The reasons are that RIN fluctuations in the pump laser power are easily transferred to the signals through the ultra-fast response of the Raman gain. Furthermore, because the Raman gain depends strongly on the pump wavelength, drift in the pump emission wavelength over time will cause the gain spectrum to change.

To avoid problems with stimulated Brillouin scattering (SBS) (explained below), the laser line width is often required to be very broad (several nm). Therefore, in principle, high-power pump lasers tend to be of multilongitudinal mode entailing poor intensity noise performance in order to better avoid SBS [40]. The multi-mode operation is therefore contradictory to the requirement of low RIN in these lasers. Furthermore, depolarizers are necessary in state-of-the-art Raman pumps to remove the polarization dependence of the gain. Pumps where the degree of polarization of the output light is less than 5% are common [41].

For semiconductor-based lasers, more than 500 mW of output power has been achieved corresponding to a power density at the facet of 20 MW/cm^2, thereby nearly reaching the design limits of the material [40]. Today, technological advances has made low-noise inner-grating-stabilized multi-mode pump lasers available with RIN values of < 150 dB/Hz, which are suitable for forward-pumped amplifier configurations [42].

Safety A final issue of FRAs concerns the safety and optical damages due to the high powers present in the deployed distributed amplifier systems. This is a rather new topic and not much has been published at this time. The concern here is mainly eye damage and the handling of optical fibers with high powers, but also to connector damage and system reliability in connection with high powers.

2.2.3. Noise sources

Besides amplified spontaneous emission (ASE) noise, the most important noise sources in FRAs are pump-mediated RIN transfer [33] and multi-path interference (MPI) noise due to double Rayleigh backscattering (DRB) [34, 43, 44]. Pump-mediated RIN transfer is, however, mainly an issue when the pump and signal are co-propagating and depends largely on the RIN level of the pump laser. MPI noise is an important limitation in high gain amplifiers and will now be described below.

Noise from MPI occurs when signal light reaches the receiver by more than one optical path and the associated phase noise is converted to intensity noise [45]. MPI results from reflections which can be either dis-

crete, such as fiber splice and connection points, or distributed along the transmission path, such as Rayleigh scattering or SBS. Rayleigh scattering is a fundamental mechanism, where the light is elastically reflected by sub-micron inhomogeneities in a fiber's refractive index [16]. MPI occurs when the signal is back-scattered twice - a process which is known as double Rayleigh backscattering (DRB). As the double-reflected light passes through the fiber, it travels a distance which is longer than the length of the fiber and will therefore be more affected by the fiber loss, or gain, than the single-pass signal. In a FRA with positive gain, the level of the MPI light at the fiber output will therefore increase rapidly with the signal gain and fiber length and can become intolerably high for high gain values.

MPI is normally quantified by the ratio of the double-reflected power and the signal power at the amplifier output. This is described in section 2.3.3. The MPI contribution to the degradation of the signal SNR can also be included in the definition of the FRA noise figure, as described by Essiambre et al. in [34].

SBS is another source of noise which can limit signal power into long fibers with low loss or gain. SBS is a nonlinear scattering mechanism which causes the light to be reflected when the power exceeds a certain SBS threshold [46]. Problems with SBS can to a large extent be controlled by sufficient broadening of the signal spectrum, e.g. by phase-modulation, or by lowering the channel power into the spans. A simple method for evaluating the power budget requirements of a passive (non Raman-pumped) link due to SBS is presented in [47]. For Raman amplified links, the SBS threshold decreases with increasing fiber length, with the ratio of forward pumping and with increasing pump power [48]. The effect of Raman amplification on the SBS threshold value is further investigated in section 4.2.

2.3. Dynamic amplifier model

This section describes a numerical model of a fiber-based Raman amplifier, which has been developed over the course of this project. The model has primarily been developed to study dynamic transient effects arising from interactions between pump and signals during propagation in the fiber. The intent has also been to study how gain transients affect the dynamic noise properties of the amplifier and how the pump direction can "shape" the signal-signal crosstalk. Finally, the model has been used to study static gain and noise properties of FRAs. Results generated using this model are presented throughout this thesis to supplement the experimental results.

The section is structured as follows: A basic description of the included physical effects is described in section 2.3.1. The derived equations for each

amplifier section are presented in section 2.3.2. The macroscopic output variables, such as gain, noise figure and MPIs, are defined in terms of the model parameters in section 2.3.3, while the model parameters, model validation and limitations are discussed in section 2.3.4.

Static (no time-dependence) results generated using this model will be presented later in section 2.4 and in chapter 3 and 4, while dynamic (time-dependent) model results will be presented in chapter 4 and 5.

2.3.1. Basic equations of the amplifier

The equations in the Raman amplifier model are rate equations taken from the literature [16, 49]. These describe the propagation of the optical power in a one-dimensional waveguide/fiber. The equations do not include dispersion or nonlinear effects, such as the Kerr-effect (responsible for self-phase modulation (SPM), parametric effects etc.). In the following description, each signal, noise bin and pump component is characterized by a forward and backward power component P. Each variable belonging to a specific component is denoted by a subscript s, n or p to indicate whether it is a signal, noise or pump component, respectively. As an example, the center frequency is consequently denoted ν_s, ν_n and ν_p. The model supports only a single pump and the Raman gain efficiency for signal wave s and noise bin n therefore always refers to the single pump p.

Signals The model supports an arbitrary number of signals, each of which has a forward and backward propagating component. The equations for the forward and backward propagating power of signal s, P_s^+ and P_s^-, are [49]

$$\frac{dP_s^+}{dz} = (g_s P_p - \alpha_s) P_s^+ + \varphi_s P_s^- \tag{2.12}$$

$$\frac{dP_s^-}{dz} = -(g_s P_p - \alpha_s) P_s^- - \varphi_s P_s^+ \tag{2.13}$$

where g_s is the Raman gain efficiency, α_s is the intrinsic loss coefficient and φ_s is the Rayleigh back-scattering coefficient, at the signal wavelength λ_s. The sum of the forward and backward propagating pump power is denoted $P_p = P_p^+ + P_p^-$. The parenthesis in (2.12) and (2.13) represent the combined gain contribution due to pump p at λ_p and passive loss of the fiber. The last term accounts for power transfer from the counter-propagating signal due to linear Rayleigh back-scattering.

Amplified spontaneous emission In the model, ASE is represented as noise bins, that is, blocks of noise power with a certain bandwidth Δf.

Each noise bin n is centered at λ_n and contains the power P_n. As such, P_n^+ and P_n^- is the total ASE at λ_n propagating in the forward and backward direction, respectively. The equation governing the propagation of the ASE noise bin of spectral width Δf, is given by [16]

$$\frac{dP_n^+}{dz} = \left(g_n P_p - \alpha_n\right) P_n^+ + 2 \cdot g_n P_p \cdot \left(1 + \eta\left(T\right)\right) h\nu_n \Delta f \quad (2.14)$$

$$\frac{dP_n^-}{dz} = -\left(g_n P_p - \alpha_n\right) P_n^- + 2 \cdot g_n P_p \cdot \left(1 + \eta\left(T\right)\right) h\nu_n \Delta f \quad (2.15)$$

Compared to the signal equations (2.12) and (2.13), the noise equations include a second inhomogeneous term to account for the spontaneous emission generated during propagation. Also note that Rayleigh back-scattering is not included for the noise bins, as it is expected to have very little influence on the behavior of the amplifier. In equation (2.14) and (2.15), $\eta\left(T\right)$ is the phonon occupancy factor

$$\eta\left(T\right) = \frac{1}{\exp\left[\frac{h\Delta\nu_n}{k_B T}\right] - 1} \quad (2.16)$$

that accounts for the temperature dependence of the phonon density of states [16]. In (2.16), k_B is Boltzmann's constant, T is the fiber temperature in Kelvin and $\Delta\nu_n = \nu_p - \nu_n$ is the frequency separation between the pump and the spontaneously emitted photon. Assuming that pump p is depolarized (see section 2.2.2), the ASE will also be depolarized and so both polarizations must be accounted for. This is the origin of the factor of two in the source term in (2.14) and (2.15).

Pump propagation and depletion For pump p, the power propagation is described by equations similar to those of the signals, i.e. [16]

$$\frac{dP_p^+}{dz} = -\left(\sum_s \frac{\lambda_s}{\lambda_p} g_s P_s + \sum_n \frac{\lambda_n}{\lambda_p} g_n P_n + \alpha_p\right) P_p^+ \quad (2.17)$$

$$\frac{dP_p^-}{dz} = \left(\sum_s \frac{\lambda_s}{\lambda_p} g_s P_s + \sum_n \frac{\lambda_n}{\lambda_p} g_n P_n + \alpha_p\right) P_p^- \quad (2.18)$$

The negative gain terms signify depletion from the signals and the ASE. The depletion terms are also multiplied with a coefficient λ_s/λ_p, or λ_n/λ_p, to account for the difference in photon energy, at the pump and Stokes wavelength. In (2.17) and (2.18), the sum of the forward and backward propagating signal s and noise bin n is denoted $P_s = P_s^+ + P_s^-$ and $P_n = P_n^+ + P_n^-$, respectively. To include more than one pump in the model realistically,

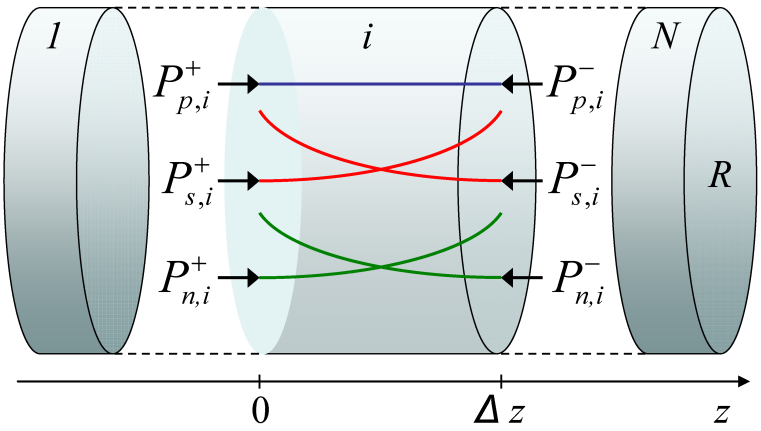

Figure 2.6.: The fiber amplifier is divided into N sections with reflectivity R at the fiber end connections. A single component of the forward and backward propagating pump, signal and ASE are seen to enter section i. In each section, the pump power due to pump p is assumed to be constant, thus providing a constant gain for the signal s and noise bin n across the section.

pump interactions would have to be included in equations (2.17) and (2.18). This can be done relatively easily by adding a gain and depletion summation over the pump wavelengths higher and lower to that of λ_p to the first parenthesis in (2.17) and (2.18). Due to limitations of time and to speed up calculations, this feature was abandoned.

2.3.2. Section equations

The following sectioned model is in large inspired by a similar sectioned model made for SOAs, which is fully described in [50]. The main work of developing the model has been to identify which effects to include and to adapt the rate equations above to a similar set of section equations for the Raman amplifier.

The general model assumption is that the spatial variation of the pump power can be approximated by dividing the amplifier into N sections of length Δz. In each section, the local pump power $P_{p,i} = P^+_{p,i} + P^-_{p,i}$ is assumed to be spatially invariant (not a function of z). Figure 2.6 shows a schematic of the sectioned amplifier and the respective power terms entering section i. The power of signal s, entering section i from from the left and right side, is labeled $P^+_{s,i}$ and $P^-_{s,i}$, respectively. Similarly, the spectral power component n of the ASE, entering section i from from the left and right side, is labeled $P^+_{n,i}$ and $P^-_{n,i}$, respectively.

Because the amplifier is spatially discrete, time is also discrete in steps

of $\Delta t = \Delta z / v_g$, where $v_g = c/n_g$ is the group velocity and n_g is the group index of the fiber. In this model, the fields are required to move with the same velocity from section to section, which means that chromatic dispersion cannot be included in the model. However, as will be explained in section 2.3.4, the lack of dispersion is not a serious limitation of the model for most contexts in which it is used. Because the pump power does not vary across section i, it follows that the gain term $gP_{p,i}$ is also spatially invariant across one section.

The sectioned equations for signal s are found in the following way. By integrating the power in (2.13) and neglecting the contribution from back-scattering, an approximate solution for P_s^- in section i can be obtained as

$$P_s^-(z) \approx P_{s,i}^- \exp\left[\left(g_s P_{p,i} - \alpha_s\right)(\Delta z - z)\right] \quad \text{for} \quad 0 \le z < \Delta z \tag{2.19}$$

Eq. (2.19) is a good approximation for $0 \le z < \Delta z$ because the contribution from Rayleigh scattering is very small across the short length. By inserting the approximate solution for $P_s^-(z)$ into (2.12) and integrating P_s^+ from $z = 0$ to $z = \Delta z$, the forward traveling power at section $i+1$ is found to be

$$\begin{aligned} P_{s,i+1}^+ &= \exp\left[\left(g_s P_{p,i} - \alpha_s\right)\Delta z\right] P_{s,i}^+ + \varphi_s P_{s,i}^- \frac{\exp\left[2\left(g_s P_{p,i} - \alpha_s\right)\Delta z\right] - 1}{2\left(g_s P_{p,i} - \alpha_s\right)} \\ &= G_{s,i} P_{s,i}^+ + \varphi_s P_{s,i}^- \frac{G_{s,i}^2 - 1}{2\left(g_s P_{p,i} - \alpha_s\right)} \end{aligned} \tag{2.20}$$

where $G_{s,i}$ is the *single-pass gain* of channel s in section i, defined as

$$G_{s,i} = \exp\left[\left(g_s P_{p,i} - \alpha_s\right)\Delta z\right] \tag{2.21}$$

The first term in (2.20) stems from the net gain of section i and the last term is the power transferred from $P_{s,i}^-$ due to back-scattering. Similarly, the expression for the backward traveling field power in signal s at section $i-1$ is found to be

$$P_{s,i-1}^- = G_{s,i} P_{s,i}^- + \varphi_s P_{s,i}^+ \frac{G_{s,i}^2 - 1}{2\left(g_s P_{p,i} - \alpha_s\right)} \tag{2.22}$$

The result for the forward and backward propagating spectral component n of the ASE power in both orthogonal polarization states and bandwidth Δf, is found by integrating (2.14) and (2.15) across one section. The result

is

$$P^{\pm}_{n,i\pm1} = G_{n,i}P^{\pm}_{n,i} + \frac{G_{n,i}-1}{g_nP_{p,i}-\alpha_n}\cdot 2\cdot g_nP_{p,i}\cdot(1+\eta(T))\,h\nu_n\Delta f \qquad (2.23)$$

where the + and the – in ± denotes the forward and backward propagating part, respectively. In (2.23), $G_{n,i}$ is the single-pass gain of noise bin n in section i, defined similarly to $G_{s,i}$ in (2.21). The first term is therefore responsible for the gain and loss contributions from section i, while the second term quantifies the amount of spontaneous emission power added by the section to noise bin n.

The equations for pump p are found by inserting approximate solutions for $P^+_{s,i}$, $P^-_{s,i}$, $P^+_{n,i}$ and $P^-_{n,i}$ (given below) into equations (2.17) and (2.18) and solving the homogeneous equations. The approximate solutions for signal s are obtained by neglecting the contribution from Rayleigh scattering in (2.12) and (2.13) and using the boundary conditions $P^+_s(0) = P^+_{s,i}$ and $P^-_s(\Delta z) = P^-_{s,i}$, i.e.

$$P^+_s(z) \approx P^+_{s,i}\exp\left[(g_sP_{p,i}-\alpha_s)\,z\right] \qquad (2.24)$$

$$P^-_s(z) \approx P^-_{s,i}\exp\left[(g_sP_{p,i}-\alpha_s)\,(\Delta z - z)\right] \qquad (2.25)$$

The approximate solutions for noise bin n comes from solving (2.14) and (2.15) with the conditions $P^+_n(0) = P^+_{n,i}$ and $P^-_n(\Delta z) = P^-_{n,i}$. These yield

$$P^+_n(z) \approx P^+_{n,i}e^{[(g_nP_{p,i}-\alpha_n)z]} + \frac{e^{(g_nP_{p,i}-\alpha_n)z}-1}{g_sP_{p,i}-\alpha_s}\cdot q(\nu,T) \qquad (2.26)$$

$$P^-_n(z) \approx P^-_{n,i}e^{[(g_nP_{p,i}-\alpha_n)(\Delta z-z)]} + \frac{e^{(g_nP_{p,i}-\alpha_n)(\Delta z-z)}-1}{g_sP_{p,i}-\alpha_s}\cdot q(\nu_n,T) \qquad (2.27)$$

where $q(\nu_n,T) = 2g_nP_{p,i}(1+\eta(T))\,h\nu_n\Delta f$ is the spontaneous emission driving term. The result for the forward and backward propagating pump p is

$$P^+_{p,i+1} = P^+_{p,i}\exp\left[-\left(\sum_s g_s\frac{\lambda_s}{\lambda_p}P^{av}_{s,i} + \sum_n g_n\frac{\lambda_n}{\lambda_p}P^{av}_{n,i} + \alpha_p\right)\Delta z\right] \qquad (2.28)$$

$$P^-_{p,i-1} = P^-_{p,i}\exp\left[-\left(\sum_s g_s\frac{\lambda_s}{\lambda_p}P^{av}_{s,i} + \sum_n g_n\frac{\lambda_n}{\lambda_p}P^{av}_{n,i} + \alpha_p\right)\Delta z\right] \qquad (2.29)$$

where $P^{av}_{s,i}$ and $P^{av}_{n,i}$ are the average power, in section i, of signal s and noise

bin n, respectively. These are given by

$$\begin{aligned} P_{s,i}^{av} &= \frac{1}{\Delta z}\int_0^{\Delta z}\left[P_s^+(z)+P_s^-(z)\right]dz \\ &= \left(P_{s,i}^+ + P_{s,i}^-\right)\frac{G_{s,i}-1}{\left(g_s P_{p,i}-\alpha_s\right)\Delta z} \end{aligned} \tag{2.30}$$

and

$$\begin{aligned} P_{n,i}^{av} &= \frac{1}{\Delta z}\int_0^{\Delta z}\left[P_n^+(z)+P_n^-(z)\right]dz \\ &= \left(P_{n,i}^+ + P_{n,i}^- + 2q(\nu,T)\right)\frac{G_{n,i}-1}{\left(g_n P_{p,i}-\alpha_n\right)\Delta z} - 2q(\nu_n,T) \end{aligned} \tag{2.31}$$

The assumption of constant pump power in each section will cause the gain to be somewhat overestimated across the amplifier, since the pump power in reality decreases exponentially in every section. By increasing the number of sections and shortening the section length, however, the gain will converge toward the correct value.

Time-dependence and boundary conditions To complete the model description, the boundary conditions for the two end sections, $i = 1$ and $i = N$, must be defined. Since model time is quantized in steps of Δt, the powers at a specific time sample t is related to the powers and gain at the previous time instant $t - \Delta t$. In the following, this is specified by the use of super indexes, i.e. P^t or $P^{t-\Delta t}$.

The boundary conditions for the left side of the first section, $i = 1$, are given by

$$P_{s,out}^{-,t} = (1-R)\left(P_{s,1}^{-,t-\Delta t}G_{s,1}^{t-\Delta t} + \varphi_s P_{s,1}^{+,t-\Delta t}\frac{\left(G_{s,1}^{t-\Delta t}\right)^2-1}{2\left(g_s P_{p,1}^{t-\Delta t}-\alpha_s\right)}\right) \tag{2.32}$$

$$P_{n,out}^{-,t} = (1-R)\left(P_{n,1}^{-,t-\Delta t}G_{n,1}^{t-\Delta t} + \frac{G_{n,i}^{t-\Delta t}-1}{g_n P_{p,i}^{t-\Delta t}-\alpha_n}\cdot q(\nu_n,T)^{t-\Delta t}\right) \tag{2.33}$$

$$P_{p,out}^{-,t} = (1-R)\,P_{p,1}^{-,t-\Delta t}G_{p,1}^{t-\Delta t} \tag{2.34}$$

$$P_{s,1}^{+,t} = (1-R)\,P_{s,in}^{+,t} + R\left(P_{s,1}^{-,t-\Delta t}G_{s,1}^{t-\Delta t} + \varphi_s P_{s,1}^{+,t-\Delta t}\frac{\left(G_{s,1}^{t-\Delta t}\right)^2-1}{2\left(g_s P_{p,1}^{t-\Delta t}-\alpha_s\right)}\right) \tag{2.35}$$

$$P_{n,1}^{+,t} = R\left(P_{n,1}^{-,t-\Delta t}G_{n,1}^{t-\Delta t} + \frac{G_{n,i}^{t-\Delta t}-1}{g_n P_{p,i}^{t-\Delta t}-\alpha_n}\cdot q(\nu_n,T)^{t-\Delta t}\right) \tag{2.36}$$

$$P_{p,1}^{+,t} = (1-R)\,P_{p,in}^{+,t} + RP_{p,1}^{-,t-\Delta t}G_{p,1}^{t-\Delta t} \tag{2.37}$$

where R is the power reflectivity at the end interface of section 1, e.g. due to a non-ideal splice or fiber connection. $P_{s,out}^{-,t}$, $P_{n,out}^{-,t}$ and $P_{p,out}^{-,t}$ are the output powers at time sample t of signal s, noise bin n and pump p, respectively. Similarly, the input power of signal s and pump p at time sample t is $P_{s,in}^{+,t}$ and $P_{p,in}^{+,t}$, respectively. The pump single-pass gain $G_{p,1}^{t-\Delta t}$ accounts for pump depletion and fiber loss across section 1 and is equal to the exponential in (2.28) and (2.29).

The main function of the boundary conditions is to relate the time-dependent input and output signal, pump and noise powers to the respective powers inside the fiber. For each power component, each term therefore constitute a specific physical contribution to the power entering and exiting the amplifier front at a specific time sample. The contributions are identical to the already described effects with the inclusion of the signal and pump input powers. A more detailed explanation of each term will therefore be omitted here in favor of keeping up the pace.

A symmetric and similar set of boundary conditions for the end interface of section $i = N$ exists, but has been left out to focus on the essential model description.

Dynamics The time-varying output powers of the model are partly a result of the time dependent input of signals $\sum_s P_{s,in}^{+,t}$ and pump $P_{t,in}^{+,t}$, and partly due to the time constants of the amplifier. Of the latter, the transit time of the amplifier, $\tau_{transit} = L/v_g$, where L is the length of the fiber and v_g is the group velocity, and the section gain terms $gP_{p,i}$ are important parameters. If both the pump and signal input are continuous waves (CWs), the model output powers simply relax into steady state after a certain relaxation time.

The sampling rate $f_s = 1/\Delta t$ is related to the number of sections N, by $f_s = v_g N/L$. It is therefore possible to maintain a specific sampling rate for different fiber lengths, by adjusting N correspondingly. Due to calculation time, however, there is a practical upper boundary on N. For a fixed model time, the calculation time t_{calc} will increase with the square of section number, i.e. $t_{calc} \propto (\text{model time})\, v_g N^2/L$. In practice, the maximum number of sections is therefore limited to ~ 5000 in this work. Typical fiber lengths used for Raman amplification range between 1 km and 100 km. At these lengths, the maximum obtainable sampling rate is therefore limited to 1 GHz and 10 MHz, respectively. For results presented in this report, the minimum section number is at no point less than 100.

Because the maximum sampling rate is limited to less than 1 GHz, the model can not be used for modeling data at typical optical communication

Parameter	Symbol	Value
Min. no. of noise bins	n_{min}	50
Typical noise bin width	Δf	250 GHz
Min. no. of sections	N_{min}	100
Reflectivity at section 1 and N end face	R	10^{-4}
Fiber temperature	T	300 K
Group index	n_g	1.46

Table 2.2.: Model parameters.

bit rates. Instead, the model is used to predict static small-signal saturation results, as well as study dynamic effects of gain, ASE and MPI when the amplifier is subjected to fluctuating input powers. In the following, amplifier parameters such as gain, noise figure and MPI will be defined in terms of the model variables.

For reference, some important parameters of the model are summarized in table 2.2.

2.3.3. Gain, noise figure and MPI

The amplifier *net gain*, often just referred to as the amplifier *gain*, quantifies the combined contributions from gain, intrinsic loss and reflections experienced by the signal during propagation. In terms of model variables, the net gain of a single channel s is defined as the ratio of its amplifier output and input powers, i.e.

$$G_s = \frac{P_{s,out}}{P_{s,in}} \tag{2.38}$$

Please note the absence of a section sub-index i in writing G_s, to avoid confusion with the single-pass gain of a single section $G_{s,i}$.

The noise figure of the amplifier is a well-established measure of the build-up of noise in electrical components. It quantifies the degradation of the electrical SNR of a signal due to the insertion of a component, such as an amplifier, in the transmission path [45]. The general definition is

$$F = \frac{SNR_{in}}{SNR_{out}} \tag{2.39}$$

where SNR_{in} and SNR_{out} are the electrical SNRs measured at the amplifier input and output, respectively. It has been the convention in optical communications to define the SNR in terms of electrical powers at an ideal

receiver. The optical powers and noise contributions must therefore be converted to electrical currents [51]. It is common practice to define an *optical noise figure* in terms of directly measurable quantities where only contributions from shot noise and signal-spontaneous beat noise are included [45,51]

$$F = F_{shot} + F_{sig-spon} = \frac{1}{G} + \frac{2\rho_{ASE}}{h\nu G} \tag{2.40}$$

In (2.40) ρ_{ASE} is the optical power spectral density (PSD) of the ASE in the same polarization state as the signal. The noise figure definition in (2.40) includes a contribution from shot noise F_{shot} and from signal-spontaneous beat noise $F_{sig-spon}$. This assumption is generally valid when the received signal power is high, reflections are low and a filter is used in front of the receiver to minimize spontaneous-spontaneous beat noise.

In the described model, the pump and the ASE are assumed to be depolarized. ρ_{ASE} at a specific wavelength λ_n is therefore related to the total ASE PSD by a factor of two, i.e. $\rho_{ASE} = P_{n,out}/2\Delta f$. In terms of the model variables, the noise figure F_s at $\lambda_s$is therefore defined as

$$F_s = \frac{P_{s,in}}{P_{s,out}} \left[1 + \frac{P_{n,out}(\lambda_s)}{h\nu_s \Delta f} \right] \tag{2.41}$$

where $P_{n,out}(\lambda_s)$ is noise bin output power interpolated at λ_s. In case of static input powers, the noise figure is a good parameter to describe the amount of amplifier noise added to the signal. Because the definition in (2.40) relies on the instantaneous input and output powers, it is often more meaningful to characterize the dynamic OSNR at the amplifier output, when the average input power contains large variations in time. Because the OSNR can strongly influence the bit-error rate (BER) at the point of signal detection, sudden changes in the OSNR can result in burst-errors in the receiver (see chapter 5). The OSNR is defined as the ratio of the combined power in the signal and the combined noise power in bandwidth B, i.e.

$$OSNR = \frac{P_s}{P_{noise,B}} \tag{2.42}$$

In optical communications, a bandwidth of $B = 0.1$ nm is often used and this bandwidth is also used throughout this thesis. If the noise is unpolarized, the noise power is equal to $P_{noise,B} = 2\rho_{ASE}B$.

The combination of long fibers and low loss makes double Rayleigh backscattering (DRB) a major noise source in Raman amplified systems [16, 43]. Because the reflected light is in-band, it cannot be filtered away and must be kept at a minimum during transmission. The amount of reflected light in a signal can be quantified using the MPI noise ratio, which is the ratio of the double

reflected power $P_{s,DRB}$ traveling in the same direction as the signal, and the power in signal s

$$MPI = \frac{P_{s,DRB}}{P_s} \tag{2.43}$$

In the model, the reflected power from all sections, whether due to end reflections or Rayleigh scattering, is kept track of in a separate DRB component of signal s. This component does not contribute to the pump depletion, but serves merely as a tool for the MPI evaluation.

2.3.4. Model parameters, validation and limitations

The model uses three sets of wavelength dependent parameters for each fiber type supported by the model. The parameters have been provided by OFS Fitel Denmark ApS and have been characterized experimentally at their production facility in Brøndby, Denmark. The parameters are the Raman gain efficiency g, intrinsic loss α_{dB} and Rayleigh back-scattering coefficient φ as a function of wavelength. These parameters are plotted for all the used fiber types in appendix B.

Model validation In the static case, the model has been validated by comparing the gain, noise figure and MPI with experimental data and results from a reference amplifier model developed at OFS Fitel Denmark ApS. The reference model is called Raman-OASIX and it uses the same fiber parameters as used by the model described here. Because Raman-OASIX is a static amplifier model, it cannot be used for dynamic modeling of gain and noise and this has been the main motivation for developing this model. A comparison of gain, noise figure and MPI results from the two models and model results with experimental gain measurements can be found in appendix A. Good agreement is found between the model and the reference data - both in the small-signal and saturated gain regime.

The dynamic properties of the model has been validated by comparing calculated output power transients with experimental measurements. By using the same input powers, fiber properties and switching frequencies as in the experiment, good agreement has also been found between model and experiment. These results are presented in chapter 4.

Limitations of the model As discussed in the previous section, the sampling rate of the model is too small to model data at standard communication bit rates. Because the average signal power is modeled instead, effects, such as dispersion and nonlinearities, which degrade the quality of data signals, are unimportant for interpretation of these model results. In some specific cases, however, the lack of dispersion can be a problem if the

dispersion-induced group delay between a co-propagating pump and signal is comparable to the sampling time $1/f_s$. For purposes of transient and response modeling, the lack of dispersion can result in inaccuracies in the fast transient rise and fall times and in the high-frequency response of a co-propagating pump and signal, as discussed in chapter 4. In general, however, this limitation is not expected to be a problem for the results presented in this thesis, due to the low sampling rate used (typically ~ 1 MHz), and the few places it is, it will be mentioned in the text.

An important limitation of the model is the lack of signal-signal gain, in which lower wavelength division multiplexed (WDM) channels provide gain to the higher wavelength channels through stimulated Raman scattering (SRS). This effect is mainly important when the channel number is high, the signal band is large and the channel power is high [52]. With this in mind, the model has only been used in limits where signal-signal interactions could safely be neglected, that is, to calculate the small-signal gain for multiple channels or to generate high-power results using only one or two channels positioned within a few nm of each other.

2.4. Static performance of fiber Raman amplifiers

In this section, calculated results regarding the static performance of lumped and distributed Raman amplifiers are presented. The results include gain, noise figure and MPI noise ratio and are calculated using the numerical model presented in section 2.3. Due to the large parameter space of various fiber lengths, fiber types, pump levels and pump configurations, the presented results have been selected in order to show some general properties of fiber-based Raman amplifiers and is not an attempt to provide a complete picture, which would be beyond the scope of this work.

The results are divided into small-signal results, where the combined input power is low enough to neglect pump depletion (see section 2.1.3), and gain saturation results, where the input power is high and the static effects of gain saturation are studied. For simplicity, only one pump wavelength is considered and is kept at 1453 nm throughout this section. The pump can be both co- or counter-propagating with the signal, or a combination of the two (bi-directional pumping). Unless otherwise indicated, the signal wavelength is at all times 1550 nm.

2.4.1. Small-signal regime

In the small-signal regime, the signal input power is sufficiently low to, in practice, neglect pump depletion (see section 2.1.3). The gain is therefore solely determined by the pump power and fiber properties (most importantly

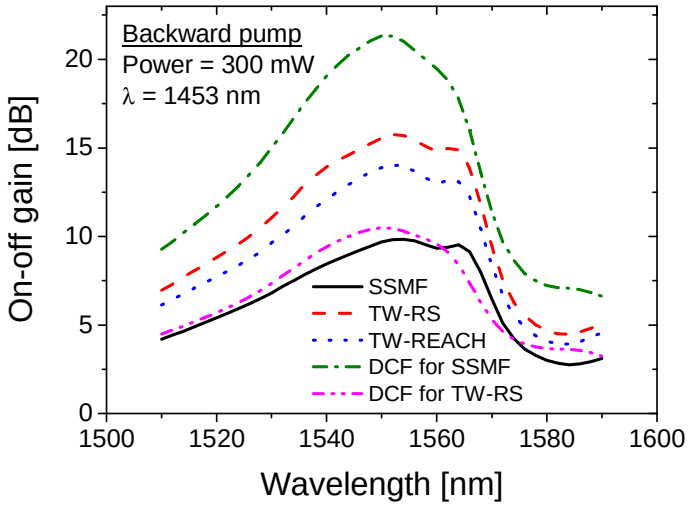

Figure 2.7.: Small-signal on-off gain vs. wavelength in various types of TF and DCF. The TF lengths are 100 km and the DCF lengths are 14.0 km and 2.9 km for SSMF and TW-RS, respectively.

the length, loss, and Raman gain efficiency). For all typical FRAs, the input can be regarded as small-signal, when the input power is less than ∼-20 dBm. Although the small-signal limit for FRAs are often much larger than this value, the combined signal input power used in this section is kept below −20 dBm.

It is common practice to define the on-off gain of a Raman amplifier as the increase in signal output power when the pumps are turned on, i.e.

$$G_{on-off} = \frac{P_{out} \text{ with pumps on}}{P_{out} \text{ with pumps off}} \tag{2.44}$$

Fig. 2.7 shows calculated on-off gain vs. wavelength for three types of TF (SSMF, TW-RS and TW-REACH) and two types of DCF (DCF for SSMF and DCF for TW-RS). The fibers are counter-pumped with 300 mW of input power. The lengths of the transmission fibers are $L_{TF} = 100$ km, while the DCF lengths L_{DCF} are chosen to fully compensate dispersion after 100 km of transmission, i.e.

$$D_{DCF}L_{DCF} = D_{TF}L_{TF} \tag{2.45}$$

where D_{TF} and D_{DCF} is the C-band dispersion of the TF and DCF, respectively. With $L_{TF} = 100$ km, the DCF lengths for SSMF and TW-RS becomes 14.0 km and 2.9 km, respectively.

In Fig. 2.7, the available fiber gain is seen not only to depend on the

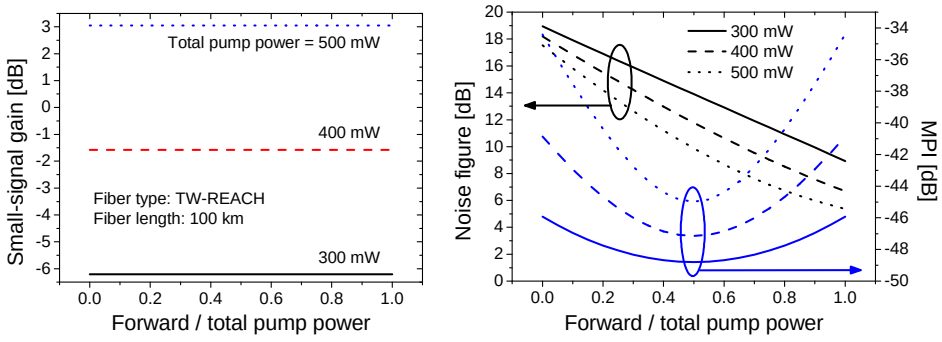

Figure 2.8.: (a) Gain, (b) noise figure and MPI vs. input power in 100 km backward pumped TW-REACH. pump powers are 300 mW, 400 mW and 500 mW. The signal input power is < -20 dBm.

fiber Raman gain efficiency g (see Fig. 2.2 on page 11), but largely on the length of the fiber. DCF for TW-RS, for instance, has the highest g of the compared fibers, but the available on-off gain in a 100 km span module is seen to be limited to 10 dB, at this pumping level. The reason for the low gain is the short fiber length of 2.9 km. The pump-signal interaction length is too short for the signal to take full advantage of the pump power. The 14 km of DCF for SSMF is seen to make more efficient use of the pump and provides more than 21 dB of on-off gain. As the TF lengths are all 100 km, their gain is a result of the fiber gain efficiency and loss. Of these, TW-RS provides the highest gain of 15.7 dB and SSMF the lowest of 9.8 dB. When considering Raman amplification for system applications, it is therefore clear that both the available fiber types and lengths must be taken into account. The previous discussion suggests that it is more beneficial to pump the DCF rather than the TF for a SSMF-based system, while it is most beneficial to pump the TF, in a TW-RS system.

However, as will be discussed in the following, gain is not the only parameter to take into account and furthermore, DCF modules can be designed to compensate several spans.

Apart from length and fiber properties, the ratio between the amount of forward and backward pumping has a large influence on the amplifier noise properties. Fig. 2.8 (a) shows the calculated small-signal gain in 100 km TW-REACH fiber. The gain is calculated for three different levels of total pump power and displayed as a function of the forward pumping ratio, defined as the amount of forward pump divided by the total pump power, i.e. $P_p^+(0) \,/\, \left[P_p^+(0) + P_p^-(L)\right]$. Because the signal is sufficiently low to not deplete the pump, the gain is unaffected by the forward pumping ratio.

As shown in Fig. 2.8 (b), however, the amplifier noise figure and MPI are very much affected by the direction of the pumps. The noise figure is seen to improve (decrease) gradually as the forward pump ratio increases. By increasing the forward pump ratio, the amplification is moved further to the front of the amplifier and this will cause the minimum signal power in the fiber to increase and ensure that the signal power is high at the position in the fiber where most of the amplification take place, i.e. in the front as opposed to the back of the fiber [16]. The small-signal MPI is seen to vary with the forward pump ratio, in a symmetric manner. The minimum MPI occurs for bidirectional pumping, where the gain is most widely distributed in the fiber, and the maximum MPI occurs when the amplifier is either purely forward- or backward-pumped. The MPI level is also seen to depend on the pumping level, corresponding to the different gain levels in Fig. 2.8 (a). Similar behavior vs. forward pump ratio has been found by Nissov et al. in [44].

Although forward-pumping is seen to improve the noise figure of the amplifier in Fig. 2.8 (b), this type of pumping can have some serious negative effects, however. First of all, the path-average power in the fiber will increase and thereby increase the effect from nonlinear distortion [34], which means that the signal input power might have to be lowered to avoid nonlinear impairments. Secondly, the impact from pump-signal and signal-pump-signal crosstalk will also increase significantly in this pump configuration. The former can be reduced by using pumps with low RIN, while inter-channel crosstalk can still be significant, if the input power is high enough to saturate the pump [53]. Crosstalk effects in FRAs will be studied further in chapter 4 and 5.

2.4.2. Gain saturation

The small-signal gain of the FRA is limited by the combined rate of spontaneous emission and stimulated emission due to the ASE, as well as the fiber loss at the pump wavelength. This is the linear regime in which the output power of the amplifier is proportional to the power at the input. The constant of proportionality is the amplifier gain, referred to as the small-signal gain G_0, i.e.

$$P_{out} = G_0 P_{in} \tag{2.46}$$

As the input power is increased and the rate of stimulated emission starts to compete with the recombination rates of the spontaneous emission and ASE, the gain starts to saturate, i.e. decrease, due to decreasing available pump power. The input power required to reduce the gain by a factor of 2 (on a linear scale), compared to the small-signal gain, is the saturation input

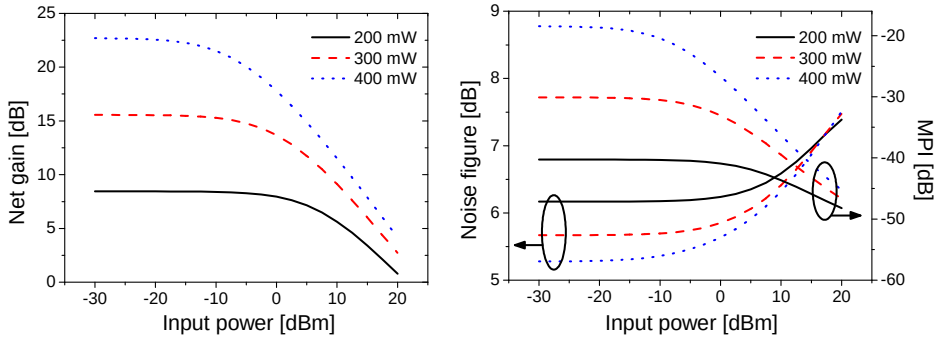

(a) (b)

Figure 2.9.: (a) Gain, (b) noise figure and MPI vs. input power in 14 km backward pumped DCF for SSMF. The pump power is 200 mW, 300 mW and 400 mW.

power $P_{sat,in}$. The corresponding output power is the saturation output power $P_{sat,out}$ and they are related by

$$P_{sat,out} = \frac{G_0}{2} P_{sat,in} \tag{2.47}$$

Gain saturation is important to quantify because the saturated gain limits the output power from the amplifier and because gain saturation can be a source of cross talk between two WDM channels, where fluctuating input power of one channel can cause the output power of the other channel to also fluctuate through cross-gain modulation (XGM) [53].

Fig. 2.9 (a) shows calculated gain vs. input power, for different pump powers, in a 14 km backward pumped DCF for SSMF. The saturation input power can be identified as the power at which the gain has dropped by 3 dB and $P_{sat,in}$ is seen to decrease with pump power. Fig. 2.9 (b) shows calculated noise figure and MPI as a function of input power for the same fiber and pump configurations. The noise figure is seen to decrease with pump power, as a result of higher gain and in accordance with eq. (2.40). At high input powers, gain saturation cause the noise figure to increase and the pump power dependence is reduced. In the same figure, MPI is seen to increase with pump power, similarly to the gain, as discussed in section 2.2.2. As the gain begins to saturate (decrease) at high input powers, MPI is also seen to decrease.

Saturation power The previous discussion shows that saturation not only affects the gain, but also the noise figure and MPI of the amplifier. From a practical point-of-view, it is therefore important to know how much power it

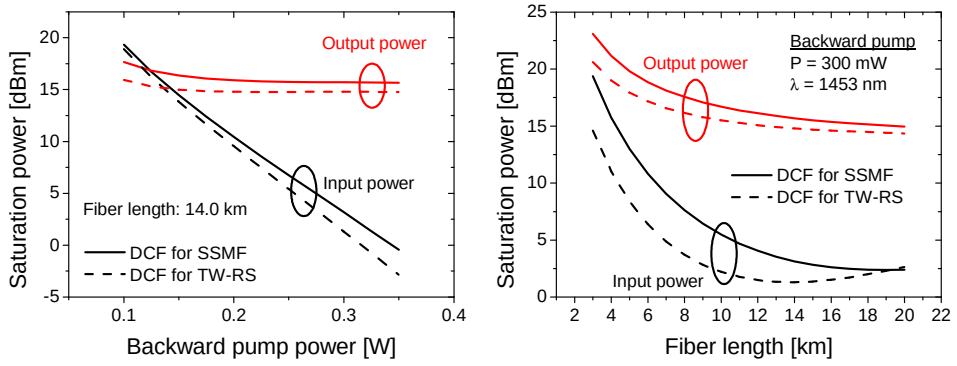

Figure 2.10.: Saturation input and output power vs. (a) pump power and (b) fiber length. The fibers are DCF for SSMF and DCF for TW-RS.

takes to saturate the amplifier under different circumstances, but also how much output power the amplifier can deliver. In the following, calculations of saturation powers $P_{sat,in}$ and $P_{sat,out}$ is presented as a function of the pumping level, the direction of the pumping and the length of the fiber.

Fig. 2.10 (a) and (b) show calculated input and output saturation power vs. pump power and fiber length, respectively, in two backward pumped DCRAs. In Fig. 2.10 (a), the fiber used is DCF for SSMF and DCF for TW-RS and the length of both fibers is 14.0 km. This length corresponds to compensation of dispersion after transmission through 100 km of SSMF or 500 km of TW-RS. In the figure, $P_{sat,in}$ is seen to decrease with pump power, while $P_{sat,out}$ remains almost unaffected by the increasing pump power. When comparing these results with eq. (2.47), it is clear that $P_{sat,in}$ drops because the gain increases with pump power, cf. Fig. 2.9 (a).

In Fig. 2.10 (a), $P_{sat,out}$ is almost independent of the pump power, which unfortunately gives the impression that the output power of the amplifier is also independent of pump power. This is not the case, however, and experimental measurements and model results both show that increasing the pump power, in general, will increase the signal output power [20]. In contrast to EDFAs and SOAs, the gain in FRAs saturates over a large output power range (typically of several dB), which means that the 3 dB saturation output power $P_{sat,out}$ in itself is not a good measure of the available output, for this type of amplifier. However, provided that the gain does not change notably under certain conditions, $P_{sat,out}$ can be used as an indicator of how the available output power changes, e.g. as in Fig. 2.11.

In Fig. 2.10 (b), the length of the two DCFs is varied, while the backward pump power is fixed at 300 mW. For short fibers, $P_{sat,out}$ is seen to decrease

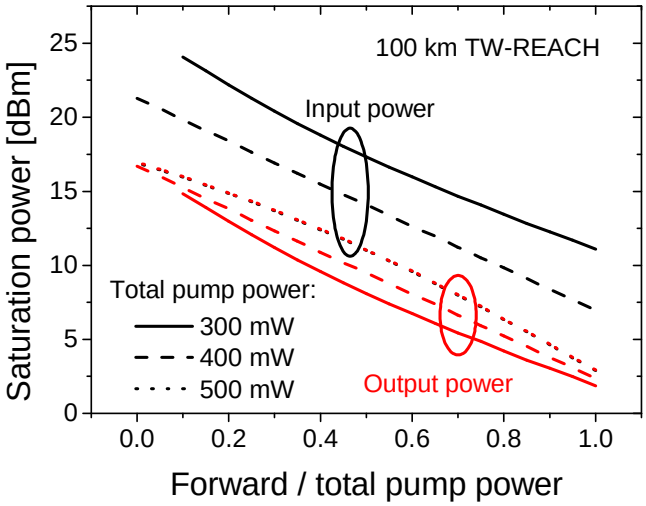

Figure 2.11.: Saturation input and output power vs. forward pump power ratio in 100 km TW-REACH. The total pump power is 300 mW, 400 mW and 500 mW.

with increasing fiber lengths and stabilize close to 15 dBm at longer lengths. $P_{sat,in}$ decreases with fiber length and experiences a minimum value close to 13 km and 18 km. The minimum is a result of the small-signal gain, G_0, which experiences a maximum at the optimum length, L_{opt}, of 12.1 km and 16.5 km (see Fig. 2.3 on page 14), for DCF for SSMF and DCF for TW-RS, respectively. At low input powers, the output power was found to peak at $L \approx L_{opt}$, corresponding to the highest available gain in the amplifier. As the gain starts to saturate, the fiber length at which maximum output power is obtained moves towards shorter fiber lengths, as fiber loss becomes more significant.

In both Fig. 2.10 (a) and (b), DCF for SSMF is seen to have higher $P_{sat,in}$ than DCF for TW-RS. Although an analytical expression for $P_{sat,in}$ is missing, we note that $P_{sat,in}$ should be related to the pump loss and gain ratio, α_p/g, through the small-signal condition, $P_s \ll \alpha_p/g$. Since this ratio is slightly higher for DCF for SSMF, it helps to explain why $P_{sat,in}$ is higher for this fiber.

In Fig. 2.11, the saturation powers are plotted vs. the forward pump ratio. The fiber used is 100 km of TW-REACH and the total pump powers are 300 mW, 400 mW and 500 mW. Note that for 500 mW pump power, the gain at the saturation point is ~ 0 dB , meaning that $P_{sat,in} \approx P_{sat,out}$ at this pump level. As the forward pump ratio change from pure backward to pure forward pumping, the saturation powers decrease by roughly 15 dB and are lowest for pure forward pumping. The results show that forward pumped

amplifiers saturate at much lower input powers than backward pumped amplifiers. The higher $P_{sat,out}$ for pure backward pumping shows that higher output powers can be obtained from backward pumped amplifiers.

To summarize the results on gain saturation, the input saturation power $P_{sat,in}$ was found to

- decrease with increasing pump power
- decrease with fiber length up to the optimum Raman length L_{opt} of the fiber
- decrease with the forward pump ratio

The output saturation power, $P_{sat,out}$, was found *not* to be a good indicator of output power in itself, due to the large output power range over which the gain saturates. But in general, the output power was found to increase with pump power and to be highest for backward pumped amplifiers. For input powers lower than $P_{sat,in}$, the output power peaks at the fiber length $L \approx L_{opt}$, given by eq. (2.11).

2.5. Summary

The fiber Raman amplifier (FRA) has been introduced and the basic principles of Raman scattering and the Raman gain efficiency has been presented. In the small-signal limit, the gain of the amplifier was shown to peak at a specific optimum length, L_{opt}, which depends on fiber parameters and the pumping level. From a systems perspective, the most important applications of FRAs has been discussed and recent state-of-the-art results was reviewed. This was followed by a discussion of the most important limitations and noise sources of the technology. To study the static and dynamic amplifier properties in detail, a new numerical FRA model has been developed. The model includes ASE and Rayleigh back-scattering and can be used to model time-dependent input and output powers, OSNR and MPI noise due to DRB. In the final part of the chapter, generated model results was used to describe various fundamental behaviors of FRAs when the pump power, fiber length and forward pump ratio was varied. The static amplifier behavior was studied both in the small-signal and saturated gain regime.

3. Dispersion compensating Raman amplifiers

Dispersion compensating fiber (DCF) has undergone considerable progress over the last decade and has become the preferred method for compensating chromatic dispersion in optical communication systems today [54]. The merits of DCF include well-controlled dispersion profiles, slope matching of dispersion over tens of nanometers, high reliability and passive operation [55]. The high Raman gain efficiency is the main reason for using DCF as gain medium in discrete Raman amplifiers. In this chapter, we describe how Raman amplification can be used in DCF to realize discrete dispersion compensating Raman amplifiers (DCRAs).

An introduction to DCRAs is given in section 3.1, followed by a discussion on various design parameters and a method for optimizing the design of backward-pumped DCRAs in section 3.2. The main focus of the chapter is on system applications and results demonstrated using DCRAs. Selected applications are presented in section 3.3, 3.4 and 3.5 and they include terminal compensation using DCRAs, a method to extend the dynamic range of inline erbium-doped fiber amplifiers (EDFAs), and a hybrid EDFA/DCRA with ultra wide gain bandwidth.

3.1. Introduction

A typical optical communication link consists of a number of transmission spans inter-spaced by repeater stages, consisting of EDFAs with DCF to provide inline amplification and dispersion compensation along the link. In such a system, the majority of the transmission loss is allocated in the transmission fiber and for this reason, Raman amplification has primarily been used to minimize the loss in the transmission fiber [56]. The idea to use Raman amplification in DCF was put forth by Hansen et al. in 1998 [57] and quickly followed by a broadband, loss-less WDM transmission demonstration by Emori et al. [58].

DCF has two main advantages that advocate for its use in Raman applications: First of all, it is a highly efficient gain medium due to its high GeO_2 doping concentration as well as smaller effective mode area, compared to standard transmission fiber. This results in a high Raman gain efficiency

(a) (b)

Figure 3.1.: (a) Rack-mountable DCF modules and (b) DCRA. The DCRA includes DCF module, pump unit, power supply and all required optical components. Courtesy of OFS Fitel Denmark ApS.

g, which determines the conversion efficiency of power from the pump to the signal along the fiber, as described in section 2.1. Secondly, DCF is at the present time deployed in many systems around the world and therefore widely available.

A DCRA essentially consists of a spool of DCF that is pumped to provide Raman gain, similarly to the amplifier schematic shown in Fig. 2.4 on page 15, where the fiber is replaced by DCF. Because the primary objective of the fiber is to compensate dispersion, the length of the DCF is determined by the amount of dispersion needed. In some cases, as will be shown later, this length is not always practical for the purpose of Raman amplification.

Fig. 3.1 (a) shows a photograph of two DCF modules, ready for rack mounting. Fig. 3.1 (b) shows a packaged and rack-mountable DCRA fully included with DCF module, power supply, pump unit and other optical components needed to combine and separate the pump and signal light. The figure shows that the module can be made to fit in a standard size rack for repeater or terminal applications.

Some important applications of DCRAs are

- to provide gain and compensate for fiber loss and thereby improve the overall noise figure of the stage (the typical DCF loss ranges from a few dB and up to 10 dB).

- to provide gain tilt adjustments, e.g. to compensate for gain tilt from

other amplifiers or wavelength dependent transmission loss.

- to provide ultra-wide-band gain beyond the standard C-band.

Examples of all three applications will be given later in the chapter. DCRA design is the topic of the next section.

3.2. Amplifier design

Perhaps the most important parameter when optimizing the design of DCRAs is the fiber. As such, the effect of the index profile of DCF for use in DCRAs has been investigated in [59]. As a design parameter for Raman fibers, the Raman figure-of-merit, $FOM_R = g/\alpha_{dB,p}$, has been proposed [60], where g is the peak value of the Raman gain efficiency and $\alpha_{dB,p}$ is the pump loss in dB/km. FOM_R can be shown to scale almost linearly with maximum unsaturated gain obtainable in the fiber, which is reached at the optimum Raman length of the fiber (see section 2.1.3) [54]. The highest reported value of the Raman figure-of-merit is $FOM_R = 10.3$ $\mathrm{W}^{-1}\mathrm{dB}^{-1}$ [61]. Using micro-structured fibers, high numerical dispersion values and high Raman gain efficiencies are predicted based on recent modeling results [62, 63], but excess background and scattering loss are still a major obstacle in these fibers [62].

As a way to better utilize the pump power in short fibers, double-pass DCRA designs have been shown to improve the pump efficiency while providing a high gain up to 30 dB and high output power of 17 dBm [64–66]. On the downside, double-pass configurations add to the design complexity with its need for optical circulators and fiber Bragg gratings and also suffers from increased multi-path interference (MPI) noise due to use of discrete reflectors [65]. Because there is a certain amount of forward co-pumping in these configurations, pump-signal relative intensity noise (RIN) transfer can also limit the amplifier performance in double-pass configurations [65].

In single-pass configurations, MPI can be reduced by using bidirectional pumping, as shown in section 2.4. However, the benefit is much smaller in DCRAs than in distributed amplifiers, due to the relatively short length of typical DCF modules [26]. Another way to reduce the impact from MPI is to use mid-stage isolators, which is an effective [67] but not always practical method, since it splits the fiber onto several spools. When it comes to minimizing the impact from pump-signal RIN transfer and nonlinearities, backward-pumped DCRAs are always preferable to forward-pumped DCRAs [51].

In the following we therefore choose to focus on the backward-pumped

single-pass DCRA as a simple and realistic configuration, but also a worst-case configuration, when it comes to MPI.

3.2.1. MPI threshold

As discussed in section 2.2.2, MPI noise due to double Rayleigh backscattering (DRB) is an important noise source in fiber Raman amplifier (FRA) and one that limits the available gain in the amplifier. System vendors are therefore likely to have a maximum limit on the MPI noise allowed by the installed DCRA. It would therefore be helpful to know the maximum pump power and gain that can be used and provided by the module, without sacrificing a low MPI noise ratio. From these figures it would be easy to evaluate the benefit of using Raman pumping in a particular module. Other important parameters are the noise figure and the power efficiency of the DCRA.

The most important macroscopic design parameters for DCRAs are the fiber type and length and the pump power and directionality of the pumping. Often the length and type of fiber will be given in advance, since the total dispersion of module should match that of the transmission fiber and system dispersion map. An example of this is an upgrade situation, where passive inline DCF modules are targeted for Raman pumping. In the following, a method is proposed for determining the optimum pump power in a backward pumped DCRA with low MPI, based on the equivalent transmission length of the compensating module and type of DCF.

Fig. 3.2 (a) and (b) show the maximum gain, the maximum pump power and the corresponding noise figure at an MPI value of -37 dB. The pump and signal wavelengths are 1453 nm and 1550 nm, respectively, and the signal input power is -20 dBm. The results are shown for two different DCF types and as a function of the compensated transmission length matched by the total dispersion of the DCF. The fully compensated transmission length L_{TF} is related to the DCF length L_{DCF} through

$$L_{TF} = -\frac{D_{DCF}}{D_{TF}} L_{DCF} \tag{3.1}$$

where D_{DCF} and D_{TF} are the dispersion coefficients at the signal wavelength, of the DCF and transmission fiber (TF), respectively. Because the compensation efficiency ratio, $-D_{DCF}/D_{TF}$, is roughly five times larger for TW-RS than for SSMF (see table 2.1 on page 12), L_{DCF} is almost five times longer in a SSMF system than in a TW-RS system, for a specific transmission length.

In generating the results in Fig. 3.2 (a) and (b), it was used that both MPI and gain increase with the pump power level. For a specific length of DCF, the max. pump power was found by increasing the pump power

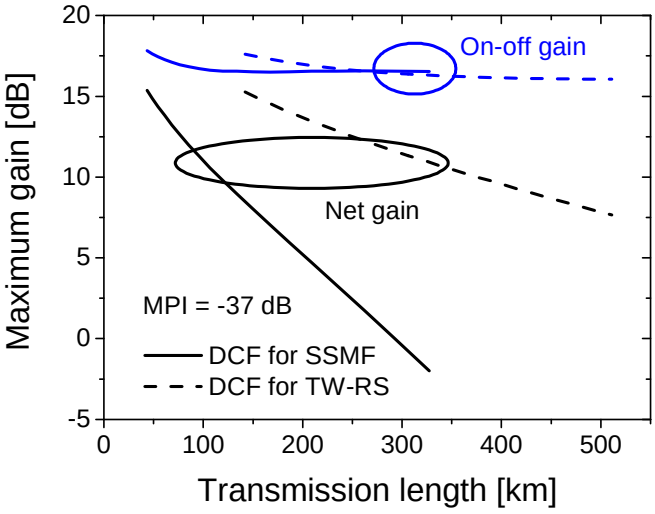

(a)

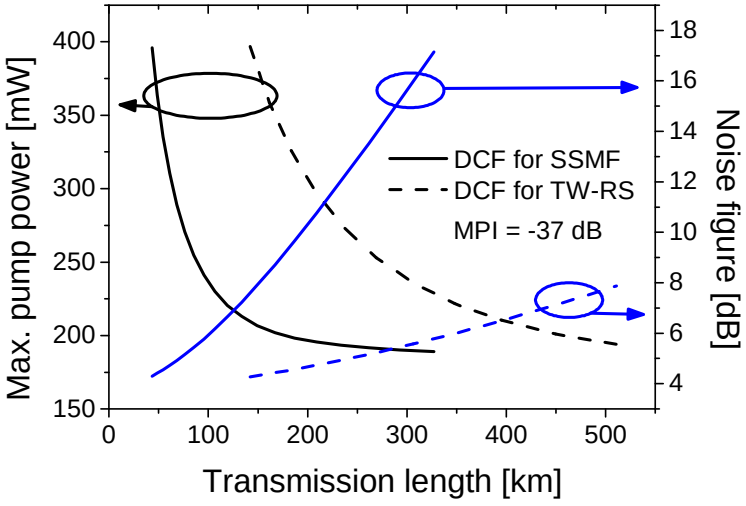

(b)

Figure 3.2.: Calculated (a) max. gain and (b) max. pump power and corresponding noise figure vs. transmission length in a backward-pumped DCRA. MPI is -37 dB and the two fibers are DCF for SSMF and DCF for TW-RS.

until MPI equaled the threshold value of −37 dB. The gain and noise figure at this maximum pump level were subsequently noted down. The MPI threshold of −37 dB is judged to be realistically low for system applications and corresponds to an electrical MPI value of approximately -40 dB (see footnote).[1] The penalty due to MPI can be evaluated by using a relation derived in [70]. For an electrical MPI of -40 dB per span, a 1 dB penalty at a bit-error rate (BER) of 10^{-9} can be found to correspond to 30 spans of transmission. The maximum pump power used in these simulations is 400 mW.

In Fig. 3.2 (a), the maximum net gain is seen to peak close to 15 dB at transmission lengths of 44 km and 142 km, corresponding to DCF lengths of 6.0 km and 4.0 km, for SSMF and TW-RS systems, respectively. For shorter transmission/DCF lengths, MPI was less than -37 dB in the entire pump power range and was therefore not a limitation. As the transmission length increases, the maximum net gain drops almost linearly in dB, however, much faster for DCF for SSMF. For a fixed transmission length, DCF for TW-RS can clearly provide the highest gain, due to the much higher compensation efficiency/shorter length of this fiber. The maximum on-off gain is almost independent of the fiber length (and type) and is approximately 17 dB for both fibers. It is clear from the figure, that the DCF length should be short if the DCRA is to deliver high positive net gain. The downside of making the fiber very short is that the amount of unused pump power also will increase and lower the power efficiency of the amplifier.

The results show that multiple-span compensation (transmission lengths of 160 km or more) is indeed possible with positive net gain in the DCRA. The number of spans that can be compensated by a single DCRA with positive net gain is clearly higher for TW-RS systems.

In Fig. 3.2 (b), the maximum pump power drops rapidly with transmission length for short fibers and approaches a long-fiber limit between 150 mW and 200 mW, for both DCF types. When using the same pump powers, the noise figure increases with the transmission length, as the DCF loss increases and the gain in the beginning of the amplifier starts to drop. For a fixed transmission length, DCF for TW-RS clearly tolerates higher pump powers and with significantly lower noise figure.

Note, that at all lengths, the noise figure of the backward-pumped DCRA is larger than the 3 dB quantum limit, which is obtainable in an ideal high-gain amplifier [71]. Compared to a passive DCF, followed by an ideal

[1] The calculation of MPI gives the worst-case result because all polarizations of both the DRB noise and the signal are included in eq. (2.43). In the electrical measurement, the MPI is dependent on the degree of polarization of the DRB noise [68]. For unpolarized DRB noise, the electrically measured MPI will be around 3 dB lower than the optical measurements [69].

discrete amplifier, however, the noise figure of the backward pumped DCRA is still superior [16]. The noise figure in Fig. 3.2 (b) can be improved by using a certain amount of forward pumping, as discussed in section 2.4.

Fig. 3.3 (a) and (b) show the same parameters as Fig. 3.2 (a) and (b), but now the fiber type is limited to DCF for TW-RS. The lower abscissa axis is the DCF length, while the upper axis is the corresponding transmission length. The maximum gain, pump power and corresponding noise figure are now plotted for MPI thresholds of −34 dB, −37 dB and −40 dB. It is clear from the figures that decreasing the MPI threshold will cause both the maximum gain and pump power to drop significantly. The effects on the noise figure are on the other hand quite small and are probably insignificant for most purposes. The dashed blue line in Fig. 3.3 (b) indicates the 3 dB quantum limit on the noise figure. Note, that Fig. 3.3 (a) predicts that it is possible to compensate up to 1000 km of transmission with positive net gain, corresponding to 10 spans of 100 km.

Together, Fig. 3.2 and 3.3 can be used to estimate the maximum obtainable gain in a backward-pumped DCRA, as well as the maximum pump power that can be used to maintain MPI below a certain value in the component. For a specific fiber type and transmission length, the expected noise figure can also be estimated and thereby indicate whether it is comparable to the noise figure of a passive DCF/EDFA solution.

In the following three sections, selected DCRA applications that have been investigated, in the course of this project, will be presented.

3.3. Terminal dispersion compensation

In dispersion-managed systems designed for long-haul transmission, DCF is used both in the transmitter (pre-), between transmission spans (inline-) and in the receiver (post-compensation). Such an N-span system is depicted in Fig. 3.4 (a). The location of the DCF depends on the dispersion map of the link, which ideally should be optimized to minimize unwanted distortion of the signal [72, 73]. The optimum map for a given link depends on a number of system parameters, including the optical power into each span, the length and number of spans, and the fiber type. By limiting the dispersion compensation to the transmitter and receiver terminals, the dispersion map and transmission link will benefit from reduced complexity, as well as from potentially simpler and cheaper in-line amplifier stages. This is because traditional multiple-stage amplifiers, in this case, can be replaced by simpler amplifiers without mid-access points for DCF. Such a dispersion map could be used in an upgrade situation, where a low bit rate system is to be upgraded to a higher bit rate, e.g. from 2.5 Gbit/s to 10 Gbit/s, without

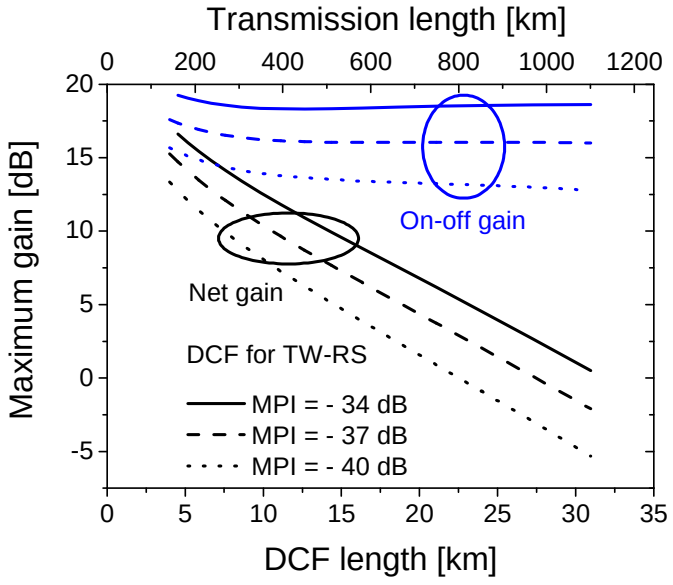

(a)

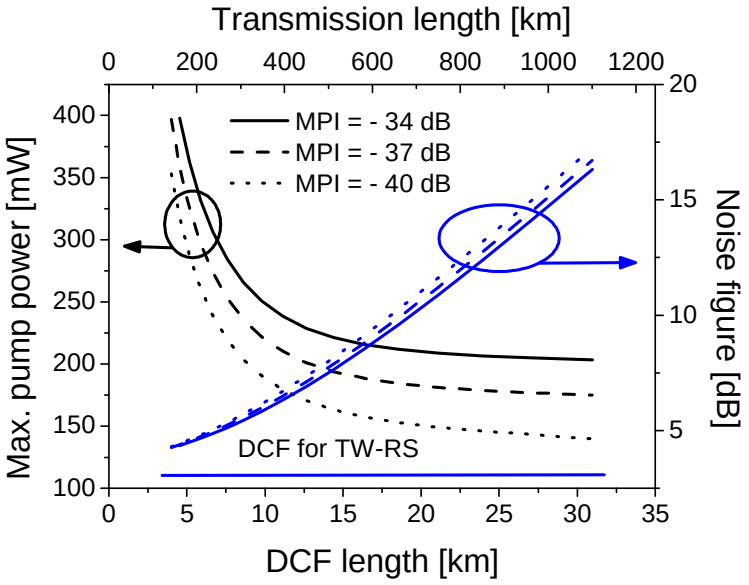

(b)

Figure 3.3.: Calculated (a) maximum gain and (b) maximum pump power and corresponding noise figure vs. DCF/transmission length in a backward-pumped DCF for TW-RS. MPI threshold is varied between -34 dB, -37 dB and -40 dB.

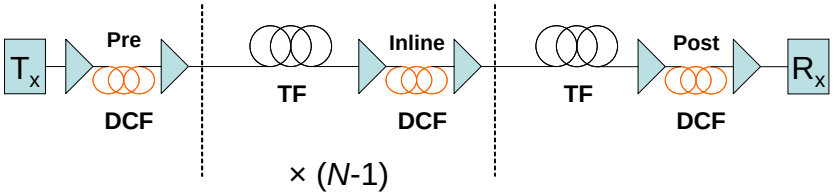

(a) Conventional dispersion map

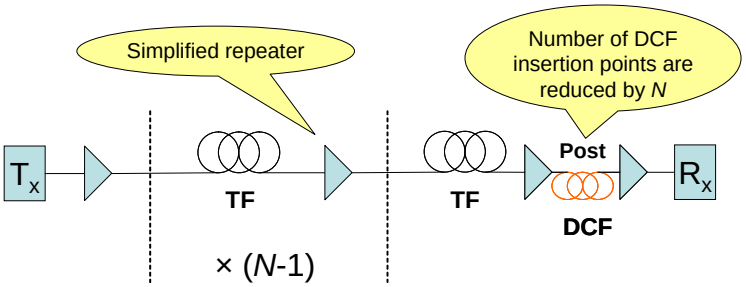

(b) Post compensation only

Figure 3.4.: (a) Conventional inline dispersion map and (b) a simplified dispersion map, where only post-compensation is used.

altering the link. Furthermore, by using Raman amplification in the dispersion compensating module, the minimum signal power in the DCF span is increased, potentially lowering the noise figure of the combined module. Terminal-only compensation has previously been investigated for SSMF, where both pre- and post-compensation were used [74].

In this experiment, which was published at the Conference on Lasers and Electro-Optics (CLEO) 2006 [75], further simplification is introduced by limiting the number of DCF points to one, namely after transmission (post-compensation). An example schematic of a purely post-compensated link (without Raman gain) is shown for comparison in Fig. 3.4 (b). In our setup, Raman gain is used in the DCF to provide gain in the module and thereby improve the optical signal-to-noise ratio (OSNR) into the receiver. Transmission of 16×10 Gbit/s with 50 GHz channel spacing is demonstrated, over 240 km non-zero dispersion-shifted fiber (NZDSF), TW-RS, using this technique.

3.3.1. Experimental setup

The setup is shown in Fig. 3.5. In the transmitter, 16 co-polarized channels, in the wavelength region from 1547 nm to 1554 nm, are modulated with a 10 Gbit/s non-return-to-zero (NRZ) signal, using a Mach-Zehnder

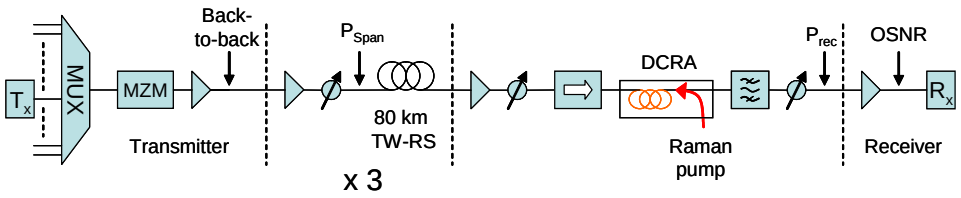

Figure 3.5.: Experimental setup for 16 WDM channel, post-compensated 10 Gbit/s system.

modulator (MZM) and subsequently amplified. The transmission link consists of 3×80 km spans of TW-RS (D = 4.6 ps/nm/km at 1550 nm). The average input power into the span is -2 dBm per channel and the power is set using variable optical attenuators (VOAs) before each span. The channels are further amplified and sent through a VOA and an isolator before entering the DCRA. The DCRA is backward-pumped using two depolarized pumps, with center wavelengths at 1428 nm and 1456 nm, to obtain a Raman on-off gain of 12 dB and a gain ripple less than 0.3 dB for the combined module in the given wavelength region. The length of the DCF is 7090 m and the residual dispersion of the combined system is 78 ps/nm at 1550 nm. The channels are selected using a tunable band pass filter and detected in a pre-amplified receiver, where BER measurements of all channels are performed. The BER dependence on the received power, P_{rec}, measured at the input to the pre-amplifier, is measured back-to-back (right after the transmitter) and after transmission. The receiver sensitivities are evaluated as the received power required to obtain a BER = 10^{-9}. The BER dependence on the received OSNR is also recorded. The OSNR is monitored just after the pre-amplifier and varied by changing the power into the preamplifier.

3.3.2. Results and discussion

Fig. 3.6 (a) shows receiver sensitivities of all 16 channels measured back-to-back and after 240 km, post-compensated transmission. All channels are seen to be successfully transmitted with error-free performance and with a spread of no more than 1 dB across all channels. Fig. 3.6 (b) shows the receiver sensitivity and OSNR penalties for all 16 channels, evaluated as the difference in sensitivity between back-to-back and after 240 km. The average channel penalty is 1.1 dB and good agreement between the sensitivity and OSNR penalties is found. It should be noted that to make a general conclusion as to the dispersion map used here, a longer transmission distance would be needed.

To summarize, this work demonstrates and evaluates a post-compensated

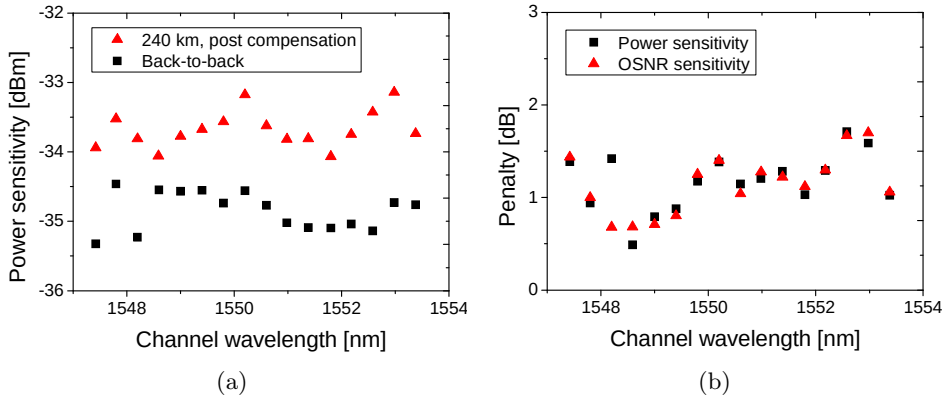

(a) (b)

Figure 3.6.: (a) Receiver sensitivities measured before and after transmission. (b) Sensitivity and OSNR penalties after 240 km for all 16 channels.

16×10 Gbit/s wavelength division multiplexed (WDM) system using only a single dispersion compensation/amplifying DCRA module inserted after transmission. After 240 km of NZDSF transmission, the sensitivity and OSNR penalties are found to be limited to 1.1 dB $\pm$ 0.6 dB. The results show that post-compensation using DCRAs could be of considerable practical interest for simplifying short- to medium-range optical transmission links or upgrading a 2.5 Gbit/s systems to a 10 Gbit/s.

3.4. Dynamic range extension of inline EDFA

Hybrid combinations of EDFAs and Raman amplifiers utilize the high conversion efficiency of the EDFA and versatile bandwidth, low noise and high linearity of the Raman amplifier [39, 76]. Hybrid combinations of remotely pumped EDFAs and distributed Raman amplification have been shown to increase the maximum transmission distance of repeater-less systems beyond 400 km [77], as well as increase the span lengths of ultra-long haul transmission systems up to 150 km using a discrete EDFA and a single Raman pump wavelength to pump the transmission fiber [56]. As a discrete amplifier, a hybrid EDFA/DCRA has been used to demonstrate $>$ 20 dB gain in a 100 nm bandwidth, thereby covering the entire S+C+L band [39]. Furthermore, DCRAs in combination with semiconductor optical amplifiers (SOAs) have been used as discrete linear amplifiers for metro WDM networks with mixed span losses [78].

The possibility of extending conventional span lengths by up to 50% or 100% is attractive, since it lowers the "first cost" of the system [56] and provides larger freedom in the positioning the repeater along the link. Some-

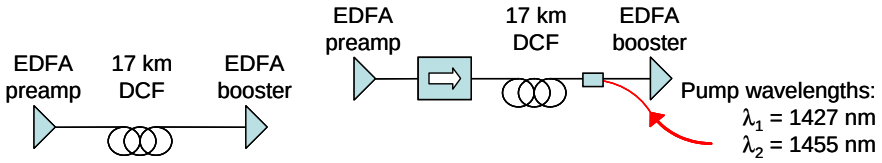

(a) Dual-stage EDFA (b) Hybrid DCRA/EDFA

Figure 3.7.: (a) Conventional dual-stage EDFA with passive DCF module. (b) Hybrid configuration with active DCRA.

times, however, distributed amplification is not an option, either because the vendor is concerned about high optical powers in the field, or because the transmission fiber is not suited for distributed amplification (e.g. fiber has a low Raman gain efficiency). In this case, discrete repeater amplifiers must instead be used to compensate the increased span loss and these should be optimized for high gain and low input powers. Furthermore, to find use in broadband applications and spans with varying loss, the repeater is also required to provide flat gain in a wide wavelength and dynamic range.

In this work, which was published at the Optical Amplifiers and Their Applications (OAA) conference in 2006 [79], a new hybrid amplifier is demonstrated, based on a commercial dual-stage EDFA, with high gain and low gain ripple. The hybrid amplifier is capable of compensating both loss and dispersion after 120 km transmission through SSMF. The amplifier consists of a commercially available and field-deployed EDFA combined with a DCRA. The addition of the Raman gain allows for an increase of the operational gain range with a minimum influence on the gain ripple in the C-band (1530 nm - 1565 nm), as well as an increase of the maximum gain up to 33 dB.

3.4.1. Experimental setup

The two configurations tested in this work are pictured in Fig. 3.7. Fig. 3.7 (a) shows the dual-stage EDFA with a 17 km long passive DCF inserted between the two stages. The EDFA consists of a preamp and a booster stage that are optimized for low noise figure and high output power, respectively. The DCF has a total dispersion of $D_{DCF} = -2291$ ps/nm at 1550 nm and this is chosen to fully compensate 120 km of SSMF. The passive loss in the DCF is 10.0 dB. Fig. 3.7 (b) shows the hybrid amplifier. The DCF, preamp and booster are the same as used in the EDFA configuration. The DCF is now pumped using two pump lasers that are centered at 1427 nm and 1455 nm. The maximum pump power input into the DCF is 278 mW and 279 mW, respectively. The pump wavelengths are chosen to provide

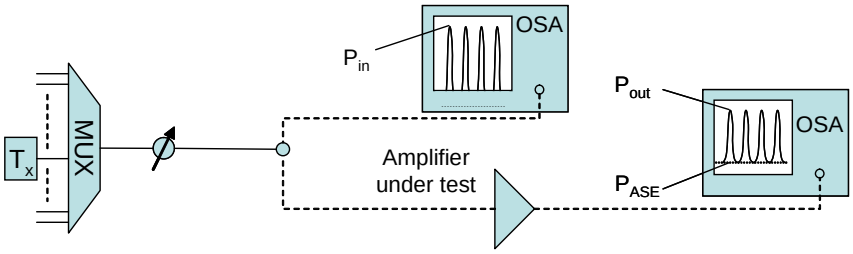

Figure 3.8.: Gain and noise figure characterization setup.

a broadband gain across the C-band and can be used to provide a gain tilt across the band by adjustment of the pump powers. Before and after the DCF is an isolator to ensure that the backwards traveling pumps are blocked from exiting at the amplifier front. A coarse wavelength division multiplexer (CWDM) is used to couple the pumps into the back of the DCF. The gain non-uniformity (GNU) is defined as the ratio between the maximum and minimum gain value in a given wavelength range. For the combined EDFA, the GNU is from the manufacturer specified to be less than 1 dB in the C-band under optimum input power. The output power from the EDFA is measured to 20.1 dBm, at 0 dBm input power. The EDFA pump powers are fixed during the measurements.

To characterize the gain and noise figure of the two amplifiers, we use the setup shown in Fig. 3.8. The input signal consists of 50 continuous wave (CW) laser sources spaced by 100 GHz and ranging from 1528.0 nm to 1567.9 nm. The power ripple after the multiplexer (MUX) is < 1 dB. An attenuator after the multiplexer is used to adjust the input power to the amplifier. To measure the individual channel power before and after the amplifier, an optical spectrum analyzer (OSA) is used. By measuring the channel input and output power, P_{in} and P_{out}, and the amplified spontaneous emission (ASE) noise output power, P_{ASE}, in a specific noise bandwidth and at the channel wavelength, the channel gain and noise figure are evaluated. The noise interpolation and correction for the actual noise bandwidth of the OSA is performed using the internal software of the OSA (ANDO 6317 model).

3.4.2. Results and discussion

The measured channel gain at different input power levels is shown in Fig. 3.9 (a) and (b) for the EDFA and hybrid amplifier, respectively. As the input power is increased, the average gain of both amplifiers is seen to drop, as the amplifiers become increasingly saturated. In Fig. 3.9 (a), the slope of the EDFA gain is also seen to change with input power, caused by the changing

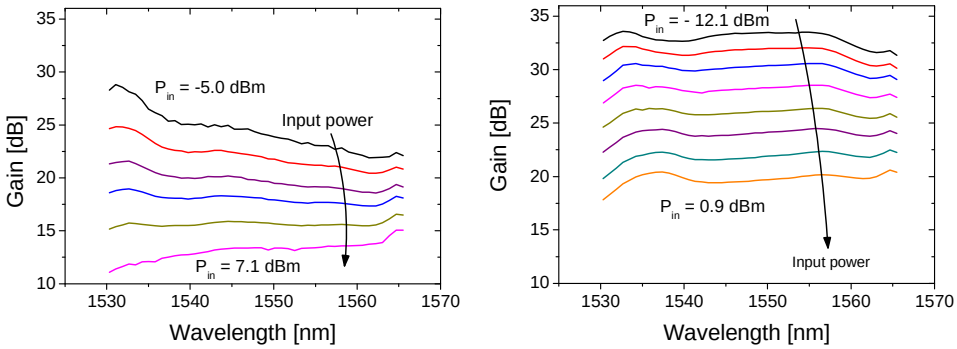

(a) EDFA (b) Hybrid DCRA/EDFA

Figure 3.9.: Measured C-band gain spectra at different signal input powers.

levels of amplifier inversion. For this particular EDFA, the flattest gain is obtained at average gain values between 16 dB and 18 dB, corresponding to combined input powers between 2.5 dBm and 3.5 dBm. Please note, that it is possible to obtain flat gain at higher input powers by increasing the attenuation between the EDFA stages, thereby maintaining a constant average inversion level of the EDFA. This technique is commonly used in commercial amplifiers and typically done using a built-in VOA. Increasing the mid-stage attenuation will, however, cause the amplifier noise figure to increase [7] and more importantly, this technique cannot be used to obtain flat gain at low input powers (below 2.5 dBm, in this case).

For the hybrid amplifier, Fig. 3.9 (b) shows that it is possible to compensate for the EDFA-induced gain tilt by adjusting the power from the Raman pumps while lowering the input signal power. In each trace in Fig. 3.9 (b), the Raman pump powers have consequently been optimized, to minimize the GNU in the 1530 nm to 1565 nm range. The results show that it is possible to produce flat gain in a 13 dB input power range, corresponding to a gain ranging from 20 dB to to 33 dB. The 33 dB average gain makes the hybrid amplifier a candidate for 120 km repeater applications in accordance with the V-span system in recommendation G.692 from the International Telecommunication Union (ITU) [80].

The flattest measured gain is shown in Fig. 3.10 (a) vs. wavelength for both amplifiers. For the EDFA, the optimum input power is 3.4 dBm, while it is -8.2 dBm for the hybrid amplifier. The large difference in input power is the main reason for the large difference in average gain, which is 16.8 dB in case of the EDFA and 29.3 dB for the hybrid amplifier. The GNU is slightly larger in the hybrid case (1.6 dB) than for the EDFA (1.0 dB). The higher hybrid GNU is attributed to the gain flattening filter of the EDFA,

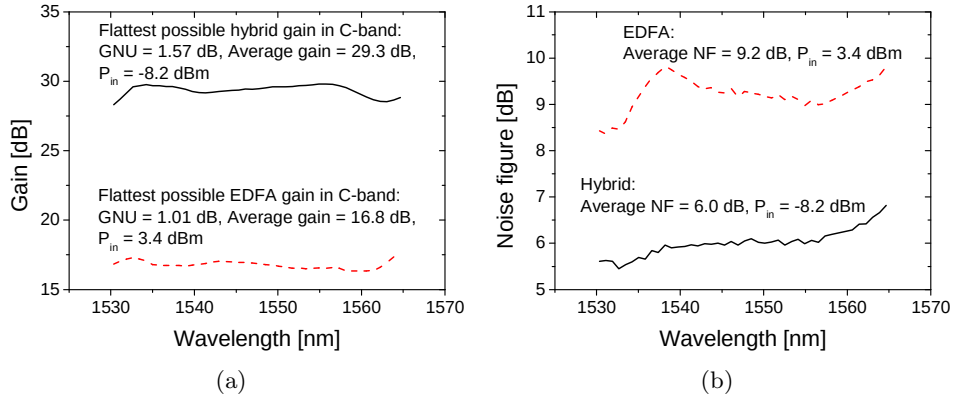

(a) (b)

Figure 3.10.: (a) The flattest possible gain using the hybrid amplifier (solid) and the EDFA (dashed). (b) The noise figure of the hybrid amplifier (solid) and the EDFA (dashed). The input powers are -8.2 dBm and 3.4 dBm, respectively.

which is not optimized for use with Raman amplification. Fig. 3.10 (b) shows noise figure vs. wavelength at the input powers used in Fig. 3.10 (a). The EDFA noise figure is roughly 3 dB larger than the hybrid noise figure and this is due to the large difference in input power in the two cases. The noise figure of both amplifiers are primarily limited by the noise figure of the preamp stage.

The GNU of both amplifiers is shown in Fig. 3.11 as a function of input power. The solid line shows the GNU of the hybrid amplifier across the C-band. The hybrid GNU varies with < 1.5 dB in the 13 dB power range and has a minimum value of 1.6 dB at -8.2 dBm of input power. By narrowing the wavelength range to 30 nm, it is possible to further improve the GNU, as shown in the dashed and dotted line plots. The minimum GNU value and optimum input power can be changed by changing the considered wavelength range, resulting in a minimum GNU value of 0.7 dB in the displayed ranges. The EDFA GNU is shown with the diamond symbols and has a minimum of 1.0 dB at an input power of 3.4 dBm and rises rapidly as the input power changes from the optimum value. As mentioned earlier, the GNU of the EDFA can be kept low at input powers higher than 3.4 dBm by increasing the mid-stage attenuation. However, the relevant parameter is the minimum power at which flat gain can be obtained, as this limits the maximum gain of the EDFA. High and flat gain can therefore only be obtained through the addition of the Raman gain, as in the case of the hybrid amplifier.

To summarize, a hybrid EDFA/DCRA has been demonstrated, which extends the EDFA's specifications both in terms of gain and dynamic range.

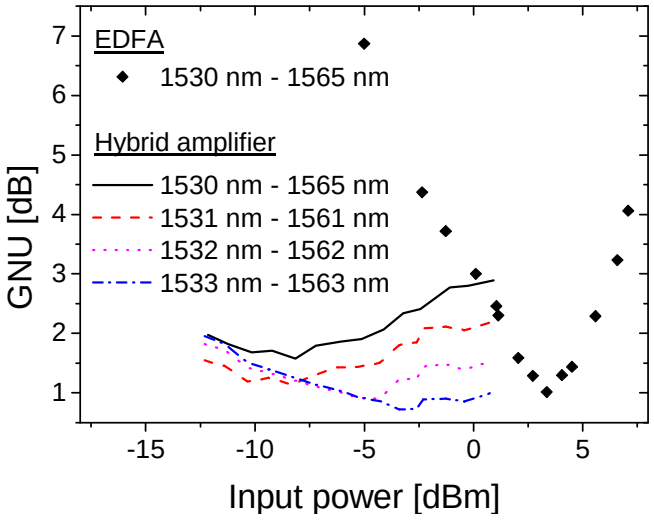

Figure 3.11.: GNU vs. input power for the hybrid amplifier (lines) and EDFA (diamonds).

The amplifier is capable of both high gain and low gain ripple for use in long span (120 km and beyond) broadband amplification. By replacing the passive DCF with a dual-pump DCRA in a standard dual-stage EDFA, a method for upgrading standard dual-stage repeaters to support increased span loss (up to 120 km) has been proposed and demonstrated.

3.5. Wide-band EDFA/DCRA

The increasing demand for bandwidth in today's backbone networks makes it increasingly necessary to extend the effective transmission bandwidth of the deployed fibers beyond the widely used C-band (1530 nm – 1565 nm) [6]. As the transmission bandwidth is mainly limited by today's amplifier-of-choice, the EDFA, new ways of extending the amplifier bandwidth must be pursued. EDFAs designed to amplify in the L-band (1565 nm – 1625 nm) are commercially available and has been demonstrated with high gain and relatively low noise figure [81]. Such an amplifier can be combined with a C-band EDFA, to obtain composite C+L band EDFAs. However, because the fiber lengths used for L-band amplifiers are typically more than five times longer than those used in C-band EDFAs, the signal band must be split prior to amplification and separate amplifiers for each band of amplification are therefore required. After amplification, a combiner is needed to combine the bands again. The splitter and combiner will contribute loss to the signals and hence increase the noise figure of the amplifier. Furthermore,

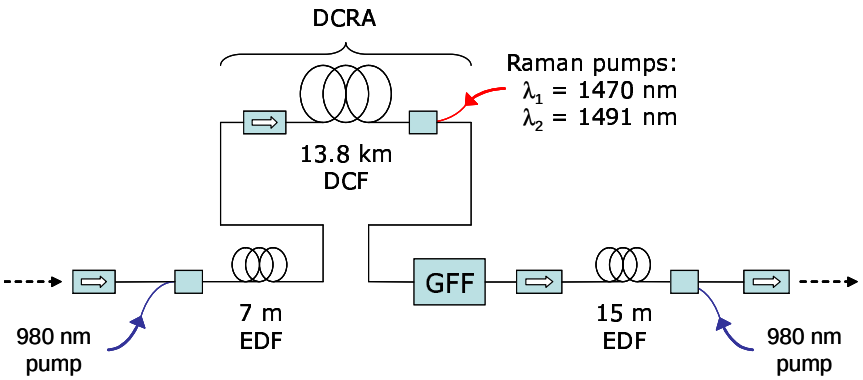

Figure 3.12.: Design of the hybrid wide-band amplifier, as used in the simulations. The amplifier consists of an erbium preamplifier stage, a mid-stage DCRA and an erbium booster stage.

a "seam" of useless bandwidth will be created between the bands, due to low gain and high noise figure in this region [82]. While the bandwidth of single EDFAs are limited, their power efficiency is high compared to that of Raman amplifiers. From an efficiency point of view, it is therefore attractive to make as much use of the EDFA gain as possible and use other means of amplification beyond the EDFA bandwidth. As an example, hybrid combinations of EDFAs and Raman amplifiers have been used to extend the seamless bandwidth of discrete amplifiers up to 80 nm [83] and 100 nm [39]. Although high gain was demonstrated in these references, the total output power was limited to $\sim$ 10 dBm, which is not sufficient to be shared among 50-100 channels, which is a realistic number of channels in future $>$ 60 nm systems.

In the following, numerical simulations of a hybrid EDFA/DCRA with high output power of 22 dBm, as well as high gain and low noise figure, will be presented. The amplifier bandwidth is 60 nm and ranges from 1530 nm to 1590 nm. Because the simulations involve both Raman and EDFA modeling, they are performed using the Raman-OASIX model, which is an in-house model of OFS Fitel Denmark.

3.5.1. Design and static performance

Fig. 3.12 shows the design of hybrid amplifier. Essentially, the amplifier consists of three stages, an erbium preamplifier stage, a mid-stage DCRA and an erbium booster stage. Four pumps are used to provide gain in the amplifier. Two 980 nm pumps are used to forward and backward pump the pre- and booster stages, respectively, using a total pump power of 505 mW.

A 1470 nm and a 1491 nm pump are used to provide gain in the DCF through backward pumping, using a combined pump power of 515 mW. The DCF is designed for SSMF, has a length of $L = 13.8$ km and compensates 100 km of SSMF. MPI is calculated to be < -36 dB across the specified 60 nm wavelength range. A gain flattening filter (GFF) is placed between the DCRA and the booster stage and serves to minimize the GNU imposed by the wavelength dependent gain. The filter has been optimized through a numerical iteration process to provide flat gain with the desired gain slope, at the amplifier output.

Due to stimulated Raman scattering (SRS), a transfer of power from the shorter to the longer wavelength channels will occur during transmission. The span input power (and hence the amplifier output power) and fiber parameters will determine the amount of inter-channel SRS and hence the induced power tilt after transmission. The output power from the amplifier is calculated to 22 dBm. Based on this value and a previous study of the induced gain tilt due to inter-channel SRS in SSMF [52], the gain tilt across the 60 nm gain bandwidth and 100 km fiber is estimated to -5 dB across the 60 nm bandwidth and a slope that is very close to being linear in dB.

Fig. 3.13 (a), (b) and (c) show calculated values of the optimized GFF attenuation, amplifier net gain and noise figure as a function of signal wavelength. In Fig. 3.13 (b) and (c), the dashed lines represent the contribution from the EDFA preamplifier section only, while the solid lines represent the total amplifier. In the simulation, 75 channels are used with 100 GHz spacing in the wavelength interval from 1530 nm to 1590 nm. The peak attenuation of the GFF in Fig. 3.13 (a) is 18.0 dB at 1560 nm, corresponding to where the DCRA and EDFA gain overlap. In Fig. 3.13 (b), the amplifier gain has an average value of 24.1 dB in the specified gain range. The EDFA can be seen to primarily provide gain in the C-band, while the DCRA provides the L-band gain. The difference between the maximum and minimum channel gain is 5 dB to compensate for the previously mentioned inter-channel SRS. The total input power used in the calculation is -2.3 dBm and this is equally shared among the 75 channels. Inter-stage losses due to isolators and CWDMs are included in the amplifier model along with a 1.1 dB output power loss. The noise figure of the amplifier is shown in Fig. 3.13 (c). Because the total noise figure is primarily determined by the noise figure of the highly-inverted first stage, the average noise figure is very low with an average of 4.1 dB and less than ~ 4.5 dB across the entire spectrum. This is in spite of the high maximum loss in the GFF which, surprisingly, has only a small effect on the total noise figure.

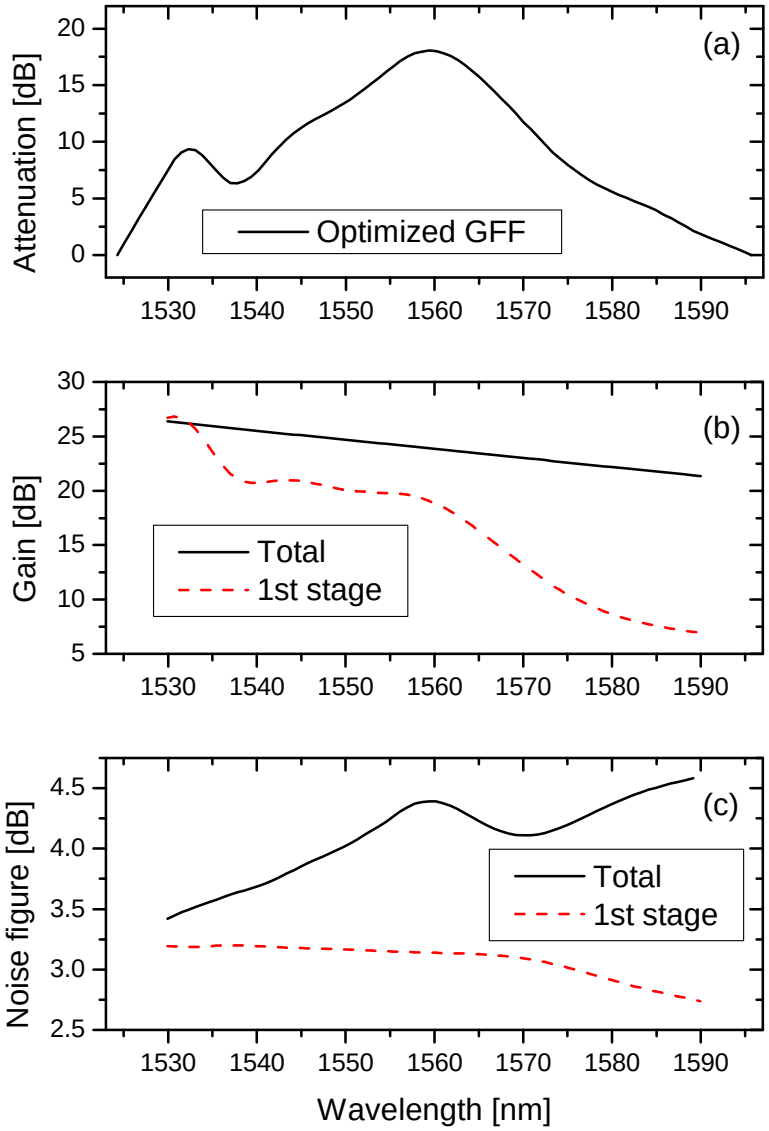

Figure 3.13.: Calculated specifications of the hybrid wide-band amplifier: (a) Attenuation of the optimized GFF, (b) net gain and (c) noise figure of the total amplifier (solid) and first stage only (dashed).

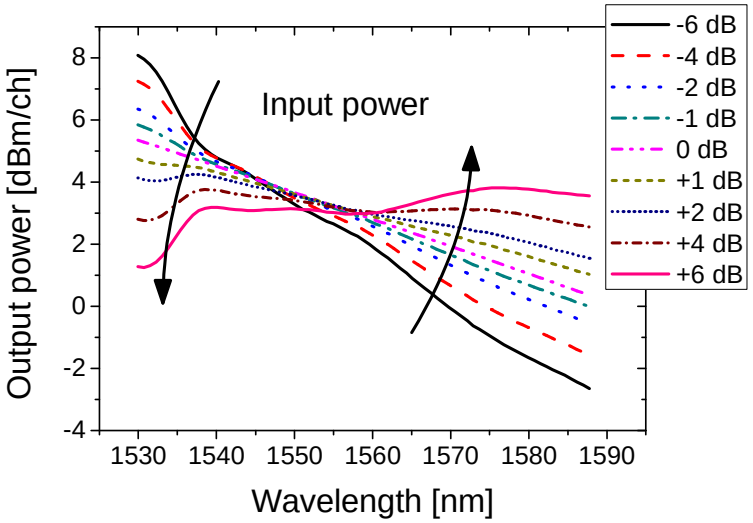

Figure 3.14.: Calculated output power per channel when the total input power is varied from -6 dB to 6 dB with respect to the specified input power of 2.25 dBm (-21.0 dBm/ch).

3.5.2. Dynamic range and limitations

As discussed in section 3.4, state-of-the-art EDFAs have functionality to regulate gain tilt according to the span parameters and input power. In order for the hybrid amplifier to be useful in system applications, it must also be able to accommodate input powers in a certain dynamic range due to mixed span losses and input powers. Furthermore, the gain tilt at the output should be adjustable, so it is possible to match the gain tilt to a specific combination of fiber type, fiber length, channel loading and input power to the span.

Fig. 3.14 shows the channel output power of all 75 channels as a function of the channel wavelength. The total input power ranges from -6 dB to +6 dB with respect to the specified total input power of 2.25 dBm. From the figure, it is clear that the power slope at the output is quite dependent on the total input power and average inversion of the amplifier, while the total output power is remains fairly constant. Fig. 3.15 shows the average gain and noise figure as a function of the total input power to the amplifier. The average gain is mainly dominated by the saturation output power of the booster EDFA and is seen to decrease on a one-to-one basis with input power. As the gain becomes more saturated, the noise figure starts to increase from ∼3.5 dB, at low input powers, to 5.5 dB, at 4 dBm input power.

Although the channel output power in Fig. 3.14 becomes less uniform

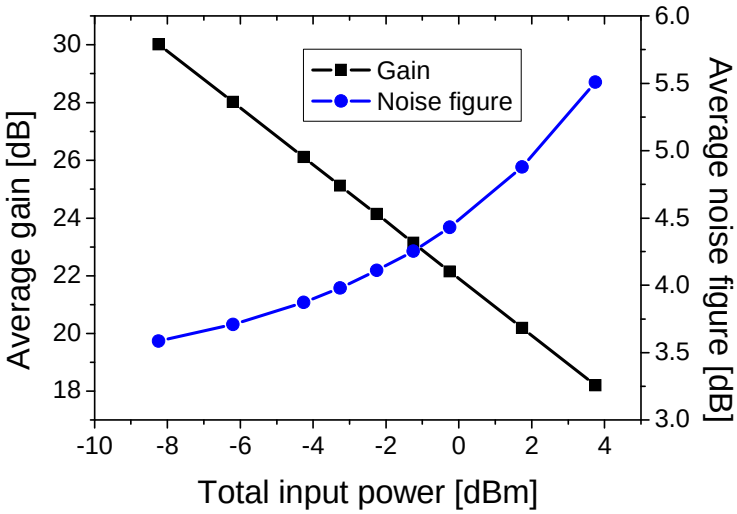

Figure 3.15.: Calculated average channel gain and noise figure vs. total input power.

and linear as the input power changes from the 0 dB optimum (corresponds to a total input power of 2.25 dBm), it does remain close-to-linear across the entire wavelength range, in particular in the range from 1537 nm and up. This means that the amplifier input power, to some extent, can be used to regulate the output power slope of the amplifier. Because there is a limit on the amount of power available after transmission, this way of regulating the gain slope is not very good, however. Another way of affecting the output power slope is by changing the amplifier pump powers. This method assumes there is a way to optimize the pump powers and thereby obtain linear gain slope for different input powers. Due to lack of time, however, this pump optimization scheme has not been further investigated.

In summary, modeled results on a new hybrid EDFA/DCRA with 22 dBm output power, 60 nm gain range and less than 4.5 dB noise figure in the specified wavelength range has been presented. The results indicate that DCRAs used in combination with EDFAs is a feasible and powerful method for increasing the transmission bandwidth in future high-capacity links. The results also show that issues related to the dynamic range and control of the gain tilt still need further investigation for this type of amplifier.

3.6. Summary

DCF is a very appropriate gain medium for use in discrete FRAs, due to its high Raman gain efficiency and large deployment numbers. Using the

developed model, a method has been presented for evaluating the maximum gain and allowed pump power in backward-pumped DCRAs, while MPI is kept at an acceptable low level.

Three recently demonstrated applications of DCRAs have also been presented in this chapter. In the first application, DCRAs are used for terminal compensation, where all dispersion compensation is handled by DCRAs in the transmitter and/or receiver terminal of a link only. The method provides a simple way of upgrading low bit-rate links without performing link alterations and the potentially long DCF modules used in the terminals could make efficient use of the Raman pump light and thereby improve the efficiency of the pumping. DCRAs were also used to extend the gain and dynamic range of commercially deployed inline EDFAs to provide flat gain with up to 33 dB average gain in the entire C-band. Thus, by addition of the DCRA, the EDFA usage is extended to support 120 km spans with up to 33 dB loss. Finally, a DCRA in combination with an EDFA has been shown to increase the gain bandwidth of future inline amplifiers. By providing flat gain and 22 dBm output power in a 60 nm range, as well as low noise figure of < 4.5 dB, the detailed simulations of a hybrid EDFA/DCRA shows promising results for future inline wide-band amplifiers with bandwidths of 60 nm and beyond.

4. Raman-based passive optical networks

Long reach access networks have been proposed as a promising way to reduce the unit cost of bandwidth in fiber-to-the-premises (FTTP) solutions [84,85]. Long-reach access is based on the idea of using a high-capacity, high-split passive optical network (PON), with a reach of $\sim$ 100 km, to combine optical access and metro into a single system [86]. To extend the reach of today's 20 km systems, the long-reach PON makes use of an amplified feeder link to bridge the metro and passive access network. Systems with symmetric upstream (US) and downstream (DS) data rates of 10 Gbit/s, split factors of 1024 and link lengths up to 135 km have been reported [84, 86]. These demonstrations, however, make use of more complicated schemes such as forward error correction (FEC) and electronic dispersion compensation (EDC) [84] and separate fibers and amplifiers for the US and DS channels [84, 86]. Interesting proposals for scalable extended reach PONs have also been put forth by the SARDANA project [87] and a hybrid Raman-semiconductor optical amplifier (SOA)-amplified PON with 60 km reach has also been proposed by AT&T [88].

We have recently proposed a simple, bi-directional, 80 km PON link based on distributed Raman amplification (DRA) and non-zero dispersion-shifted fiber (NZDSF) [89]. This link design is advantageous since it combines the US and DS signals on a single fiber and features superior noise performance compared to terminal-based amplification, due to the distributed Raman gain. Furthermore, the low dispersion coefficient of the NZDSF omits the need for dispersion compensation for reaches up to 120 km [90].

In this chapter, Raman-based PONs with extended reach up to 120 km are discussed and evaluated. The focus is entirely on physical layer and back-haul part of the network, which consists of the amplified feeder/PON link between core/central node in the metro network and the splitting point at the local exchange in the access network.

The network architecture is presented in section 4.1 and a power budget for the access part is estimated. In section 4.2, calculations of the maximum reach and channel capacity of the link are performed and discussed with the purpose of identifying an optimum system configuration. An experimental demonstration of a bidirectional PON link with 120 km reach is presented in

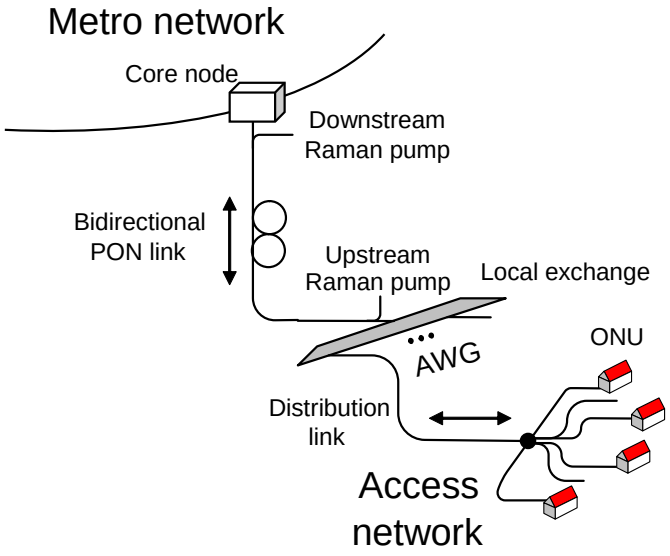

Figure 4.1.: Raman-based long-reach PON architecture. The PON link consists of a single fiber and employs bidirectional traffic and Raman pumping.

section 4.3. Finally, the dynamic performance of a bi-directionally pumped link is investigated experimentally and theoretically in section 4.4.

4.1. Architecture and power budget

The proposed bidirectional long-reach PON link [89] is pictured schematically in a network context in Fig. 4.1. The PON link connects the metro core node to the local exchange, where the DS wavelength division multiplexed (WDM) channels are demultiplexed and further distributed to the splitting points in the access part of the network. In this proposal, the link consists of a single fiber carrying bidirectional traffic. There are no standards for the long-reach PON at this time, but it has been suggested to use a 10 Gbit/s channel base rate and to split the C-band into an up- and downstream band, and thereby utilize the well-known amplification band of the erbium-doped fiber amplifier (EDFA) [84].

In our proposed PON architecture, NZDSF is used in the PON link for improved Raman gain efficiency and low dispersion compared to standard single-mode fiber (SSMF). This choice of fiber relaxes the pump power requirements and the need for dispersion compensation in these networks [90].

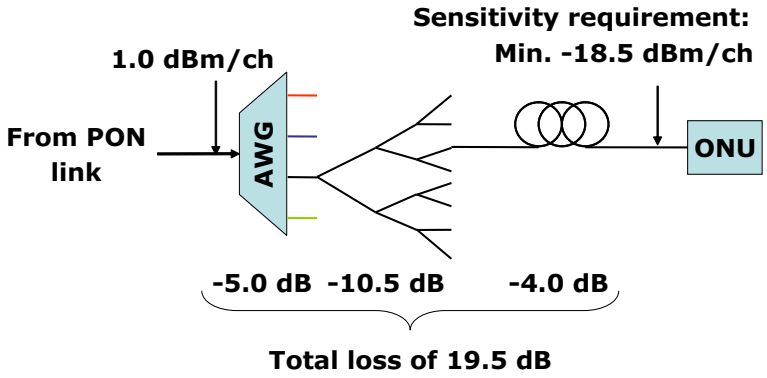

Figure 4.2.: Power budget for a 1:8 split PON.

4.1.1. Power budget

Figure 4.2 shows a power budget for the access part of a long-reach PON with a splitting ratio of 1:8. This splitting ratio is considered to be a minimum ratio for a practical system and the budget thus constitutes a minimum loss to be expected in a practical access network. For a 10 Gbit/s channel base rate, this split ratio ideally supplies each end user with a symmetric bandwidth of 1.25 Gbit/s. The budget assumes an insertion loss of 5 dB in the local exchange arrayed waveguide grating (AWG), a non-ideal splitting loss of 10.5 dB and up to 4 dB of loss due to transmission ($1 - 20$ km) in the access network. The total access loss adds up to 19.5 dB. The receiver sensitivity is assumed to be -18.5 dBm and corresponds to typical sensitivity value for a 10 Gbit/s PIN receiver at a bit-error rate (BER) of 10^{-9} (see section 4.3).

The budget shows that a minimum link output power of $P^{min}_{s,DS,out} =$ 1.0 dBm per channel is required of the DS channels to manage error-free detection at the optical network unit (ONU). This parameter is used in the following section to evaluate the channel capacity as a function of PON link length, total link input power and pumping configuration.

4.2. Link reach and channel capacity

Several effects limit the available output power and contribute to the added noise in an amplified link, such as the described PON link. As discussed in section 3.2, multi-path interference (MPI) noise due to double Rayleigh backscattering (DRB) is an important source of noise that limits the maximum gain in long fibers employing distributed amplification. Another important noise source in low loss fibers is stimulated Brillouin scattering

(SBS) [46], which is a nonlinear scattering process of light from sound waves (acoustic phonons). In this process, most of the input signal light can be converted into backward-traveling Stokes light, if the signal input power exceeds some threshold level. As a result, the forward travelling signal light suffers additional nonlinear loss [91].

To evaluate the potential of the long-reach Raman PON link, we want to estimate the maximum reach of the link as well as the maximum number of symmetric (up- and down-stream) channels that can be transmitted using such a system. This estimate is difficult to make due to the vast parameter space and uncertainty of these parameters. While the link gain, noise figure and MPI can be calculated with good accuracy, SBS is harder to calculate accurately. This is because accurate SBS modeling requires detailed knowledge of the Brillouin gain (magnitude, spectral shape, bandwidth, frequency shift) for the particular fiber used, as well as detailed knowledge of the signal spectrum. Furthermore, the SBS threshold, P_{th}, changes with the length of the fiber and also depends largely on the loss profile of the fiber. The latter is critical in Raman pumped fibers, where the distributed gain can cause P_{th} to drop by tens of dB's compared to the unpumped case.

In the following, the inclusion of SBS in the amplifier model from chapter 2 is described and followed by a description of the model setup. Finally, calculated results on the maximum reach and channel capacity of Raman-based PON links are presented for three different pump configurations.

4.2.1. SBS model

To model the SBS threshold in the bidirectionally pumped PON link, we follow an approach by Kobyakov et al. in [48]. In this paper, the threshold power is defined as the input signal power that generates the output Stokes power $P_{ref}(0)$ of the same magnitude as the maximum signal power, i.e.

$$P_{ref}(0) = P_{max} \tag{4.1}$$

where P_{max} is the maximum signal power between $z = 0$ and $z = L$. For an unpumped fiber, P_{max} equals the signal input power. Using this definition, the threshold power for a continuous wave (CW) signal in a bidirectionally pumped fiber can be written as [48]

$$P_{th} = \frac{\gamma_B \alpha_s A_{eff}}{g_B} \tag{4.2}$$

where α_s is the fiber loss, A_{eff} is the effective mode area and g_B is the Brillouin gain coefficient - all at the signal/Stokes wavelength. g_B/A_{eff} has been measured to 0.67 $\mathrm{W^{-1}m^{-1}}$ for TrueWave®RS (TW-RS) [30] and this

value is used in the simulations. The dimensionless parameter γ_B must be solved numerically using the following implicit equation, given by eq. (43) in [48]

$$\gamma_B^{3/2}\sqrt{\alpha_s L_{eff}^R}\exp\left[-\alpha_s\gamma_B L_{eff}^R - \frac{g_s P_p^+(0)}{\alpha_p}\left(1-e^{-\alpha_p L}\right)+\alpha_s L\right]G_{max} = C \tag{4.3}$$

where g_s is the Raman gain efficiency at the signal wavelength, $P_p^+(0)$ is the forward pump input power, α_p is the fiber loss at the pump wavelength and L is the fiber length. The constant C is given by

$$C = \sqrt{\pi}k_B T\frac{\nu_s}{\nu_a}\Delta\nu_B\frac{g_B}{\alpha_s A_{eff}} \tag{4.4}$$

where k_B is Boltzmann's constant, $T = 300$ K is the fiber temperature, ν_s is the signal optical frequency, $\nu_a = 10$ GHz is the frequency difference between the Stokes and signal beam and $\Delta\nu_B = 20$ MHz is the full width at half maximum (FWHM) of the Brillouin gain. $A_{eff} = 52\,\mu\text{m}^2$ is used as the effective mode area at the signal wavelength (1550 nm).

In (4.3), $G_{max} = \max_{z\in|0,L|} G(z)$, where $G(z)$ is the local net gain from $z' = 0$ to $z' = z$, which depends on the level of forward and backward pumping, i.e.

$$G_s(z) = \exp\left[\int_0^z \left(g_s\left(P_p^+(z') + P_p^-(z')\right) - \alpha_s\right)dz'\right] \tag{4.5}$$

where $P_p^+(z')$ and $P_p^-(z')$ is the forward and backward propagating local pump power, respectively. In our implementation, the gain profile takes the following form in terms of the model parameters

$$G_{s,i}(z_i) = \exp\left[\sum_{k=1}^{i}\left(g_s P_{p,k} - \alpha_s\right)\Delta z\right] \tag{4.6}$$

where Δz is the model section length (see section 2.3.2) and $P_{p,i}$ is the total pump power entering section i. Finally, in (4.3), L_{eff}^R is the effective nonlinear Raman length, given by

$$L_{eff}^R = \int_0^L G(z)\,dz \tag{4.7}$$

In (4.7), L_{eff}^R is seen to be proportional to the path-average gain/signal power along the fiber length. By using the saturated gain profile $G_{s,i}(z_i)$

in the calculation of L_{eff}^{R} in (4.7), gain saturation effects due to amplified spontaneous emission (ASE) and large signal input power are therefore taken into account in the final evaluation of γ_B and P_{th} in (4.2). From analytical approximations the threshold condition in [48], P_{th} is found to scale inversely with L_{eff}^{R}, i.e.

$$P_{th} \approx \frac{const \cdot A_{eff}}{g_B L_{eff}^{R}} \tag{4.8}$$

where *const* is a constant that depends on the pumping conditions and only slightly on the fiber parameters. This approximate relationship was also observed in our modeling. Since saturation is a reduction of the gain, the use of high input powers can in some cases increase P_{th}.

To summarize: For a specific set of parameters, which includes the signal input power, the pump input powers, the pump direction and fiber parameters, such as the length, the SBS threshold power P_{th} can be found by solving (4.3) for γ_B numerically and then use (4.2) to calculate P_{th}. The calculation of P_{th} and L_{eff}^{R} has been validated by reproducing several of the results from [48], using the exact same parameters and with ASE modeling turned off. The accuracy of eq. (4.3) is discussed in [48] and based on figures (3) and (5) in the paper, we expect P_{th} to be accurate within ∼1 dB up to fiber lengths of ∼100 km. This estimate does not take the uncertainty of the parameters used into account, however.

The above equations can be used to calculate the threshold power for a CW signal in an arbitrarily pumped fiber of length L. For a signal carrying high-speed data (>100 Mbit/s), the threshold will be higher due to the relatively narrow bandwidth of the Brillouin gain. For the amplitude-shift-keying (ASK) non-return-to-zero (NRZ) modulation format, the P_{th} has been found to increase by a factor of two (3 dB) compared to the CW threshold power [91]. In the same reference, threshold improvements for frequency-shift-keying (FSK) and phase-shift-keying (PSK) formats were found to be even higher. In the following, the presented values of P_{th} is therefore multiplied by a factor of two to account for the threshold modulation dependence.

4.2.2. PON link model and parameters

The modeled bidirectional link is depicted in Fig. 4.3. The link consists of TW-RS fiber and is bidirectionally pumped using two pumps at 1450 nm. The fiber type is identical to the fiber used in our experimental demonstrations [89, 90, 92] (see table 2.1 on page 12). The pump power, the direction of the pumping and fiber length are independent parameters in the model.

To simplify the parameter space, we consider a single DS and US channel

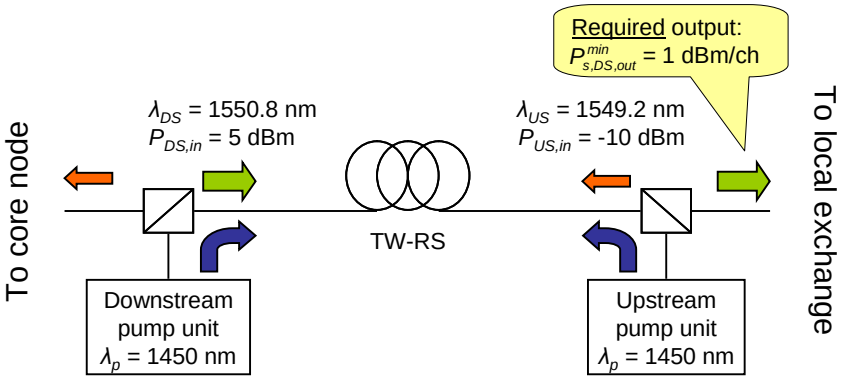

Figure 4.3.: PON link setup used for modeling maximum reach and channel capacity.

which are positioned at 1550.8 nm and 1549.2 nm, respectively. The average input powers of the two channels are $P_{DS,in} = 5$ dBm and $P_{US,in} = -10$ dBm respectively. As will be discussed in the following, these powers constitute the *total* DS and US power into the link, which can be shared among several DS and US channels. The lower upstream input power reflects the large loss in the passive part of the network. Due to the large difference in input power between the two types of channels, we assume that SBS will only be a problem for the DS channels.

For the DS channels, we require the channel output power from the link to be $P_{s,DS,out} \geq P^{min}_{s,DS,out} = 1$ dBm/ch, in accordance with the power budget presented in section 4.1.1. The sensitivity and output power requirements for the US channels are much more relaxed, because the use of preamplified receivers and therefore much lower sensitivity can be expected in the metro part of the network.

For a specific fiber length and pump configuration (power and forward pump ratio), the input power of each DS channel will be limited to minimum input power, given by $P^{min}_{s,DS,in} = P^{min}_{s,DS,out}/G$, where G is the net gain of the link. Similarly, the threshold power P_{th} puts an upper boundary on channel input power of a single DS channel. The ratio of the maximum and minimum input power of the DS channel is the dynamic range of the system, i.e.

$$Dynamic\,range = \frac{P_{th}}{P^{min}_{s,DS,in}} = \frac{P_{th}}{P^{min}_{s,DS,out}}G \tag{4.9}$$

In the minimum dynamic range limit of unity, or 0 dB, the gain is exactly large enough to deliver the required output power at the maximum allowed

input power and is therefore referred to as the *required gain*

$$G_{req} = P^{min}_{s,DS,out}/P_{th} \tag{4.10}$$

in the following. It is clear that $G > G_{req}$ to simultaneously be able to obtain the required output power and avoid SBS for the DS channels.

MPI is evaluated using the same method used in chapter 3, where the maximum gain and pump power is found at a MPI threshold of -37 dB (see section 3.2.1 for closer description). Because the DS and US channels are located close to each other in wavelength, the gain and MPI values of the two channels are almost identical.

As mentioned previously, only a single DS and US channel is modeled in this context. However, by assuming that the gain is "flat" within a certain bandwidth and the wavelength dependence of the noise figure, MPI and SBS is small, the maximum number of channel pairs supported by the link, or *channel capacity*, can be estimated from the ratio of the available DS output power and the required minimum output power per DS channel, i.e.

$$Channel\,capacity = \frac{P_{DS,out}}{P^{min}_{s,DS,out}} = \frac{P_{DS,in}}{P^{min}_{s,DS,out}}G \tag{4.11}$$

The channel capacity only indicates the available power in the system and how many pairs of DS and US channels the system can support from a power perspective. As such, it does not take into account any limitations imposed by MPI and SBS.

The flat-gain assumption is not unreasonable as the Raman gain of a single pump is relatively flat in itself, as shown in Fig. 2.7. For instance, the 1 dB gain bandwidth in 100 km TW-RS is 20 nm and the 3 dB bandwidth is 31 nm. An obvious way of extending the flat gain bandwidth is to use pumps at several wavelengths. To compare the multiple-pump case with our single-pump case, the pump powers would have to be adjusted to match the gain in our simulations across the considered bandwidth. The noise figure depends only weakly on the wavelength for constant gain and this is also the case for MPI.

4.2.3. Results

In this section, the maximum reach and channel capacity of Raman-based PON links is numerically assessed for three different pump configurations. The configurations include pure DS pumping, 50% bidirectional pumping and pure US pumping. The results are calculated using the amplifier model described in section 2.3 and 4.2.1 with the amplifier configuration described in section 4.2.2. For each configuration, the net gain G, the SBS thresh-

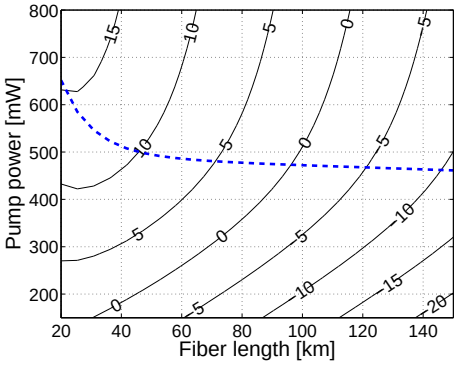

(a) Net gain (dB)

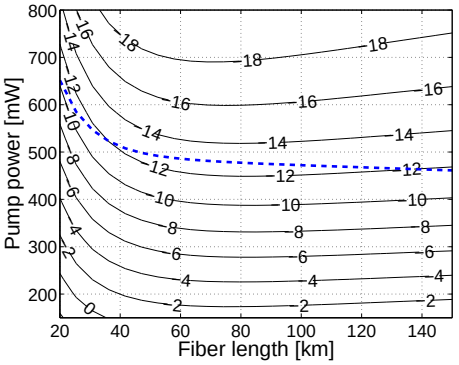

(b) SBS threshold power for ASK-NRZ (dBm)

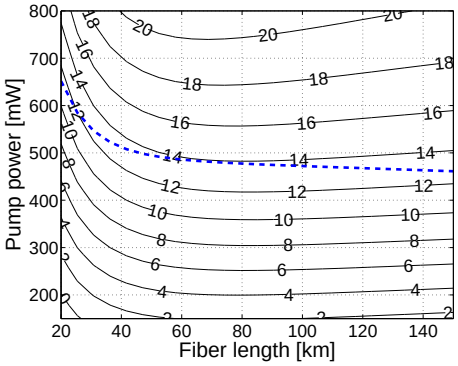

(c) Required gain (dB)

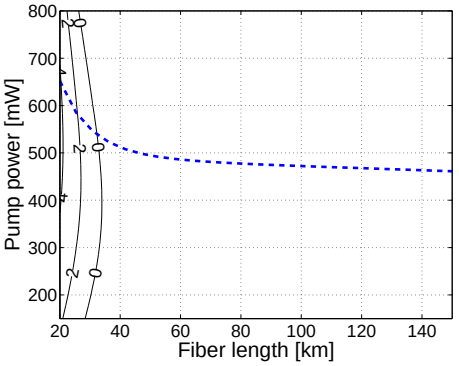

(d) Dynamic range (dB)

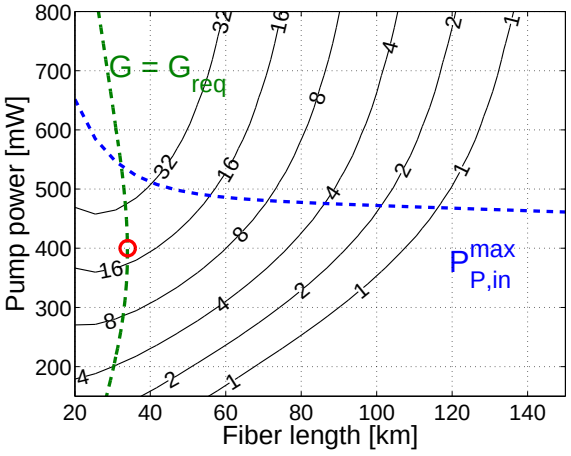

(e) Channel capacity

Figure 4.4.: Calculated results for a pure DS pumped link.

old power P_{th}, the required gain G_{req}, the dynamic range and the channel capacity are shown in contour plots as a function of the fiber length and total pump power. The fiber lengths ranges between 20 km and 150 km and the total pump power range from 150 mW to 800 mW. In all the figures, a dashed blue line indicates the maximum pump power to be used at a given fiber length, while maintaining a MPI< -37 dB.

Fig. 4.4 (a)–(e) shows the results for pure DS pumping. In this pump configuration, the high input power channels (DS) will be amplified mostly in the beginning of the fiber. The high average power in the fiber associated with DS pumping makes P_{th} very sensitive to changes in the pump power, as can be seen in Fig. 4.4 (b). In fact, Fig. 4.4 (c) shows that the net gain requirements for this type of pumping are the highest of the considered configurations, due to the low input power allowed by SBS. The high gain requirements result in low dynamic range and an almost vertical $G = G_{req}$ contour around $L = 30$ km, corresponding to 0 dB dynamic range. This means the maximum length of this link configuration is almost unaffected by the pumping level, as an increase in gain from more pumping requires the input power to be lowered by the same relative amount to avoid SBS. The point of maximum reach is marked with a red circle at 34 km and 400 mW. The channel capacity at this point is 19.

The results for 50% bidirectional pumping are shown in Figs. 4.5 (a) - (e). Due to better distribution of the pump power in the fiber, the gain increases with pump power, even for fibers longer than 120 km. In this configuration, P_{th} ranges between -11 dBm and 2 dBm in the pump power range allowed by MPI, which means the gain requirements are not as high as for pure DS pumping. Also, the maximum pump power is high due to the reduced MPI impairments associated with bidirectional pumping. This means that relatively high gain values of 10 dB can be obtained without MPI limitations, even for $L > 100$ km. The slope of the dynamic range contours are less steep compared to the pure DS pumping case, which makes it possible to overcome SBS limitations in a certain range of fiber lengths by increasing the pump power and lowering the signal input power. In Fig. 4.4 (e), the channel capacity is seen to be high throughout the allowed lower left region of the plot. The point of maximum reach is found at 110 km length and 790 mW pump power.

The results for pure US pumping are shown in Figs. 4.6 (a) - (e). In this configuration, the path-average power of the DS channels is the lowest of the three compared configurations. Therefore, P_{th} is also highest in this configuration and experiences less variation. The maximum pump power allowed by the MPI threshold is similar to the max. power found in the DS pumped configuration, but lower than for bidirectional pumping. The slope of the dynamic range contours are also the smallest for this configura-

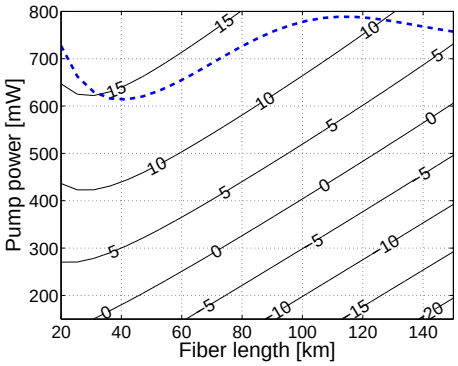

(a) Net gain (dB)

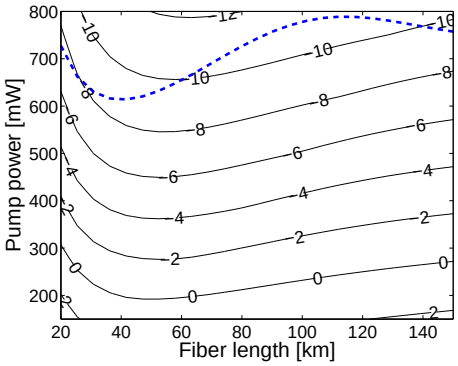

(b) SBS threshold power for ASK-NRZ (dBm)

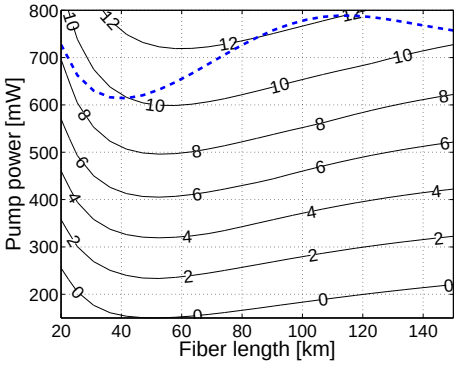

(c) Required gain (dB)

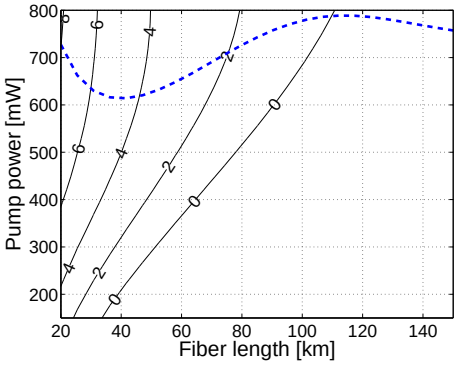

(d) Dynamic range (dB)

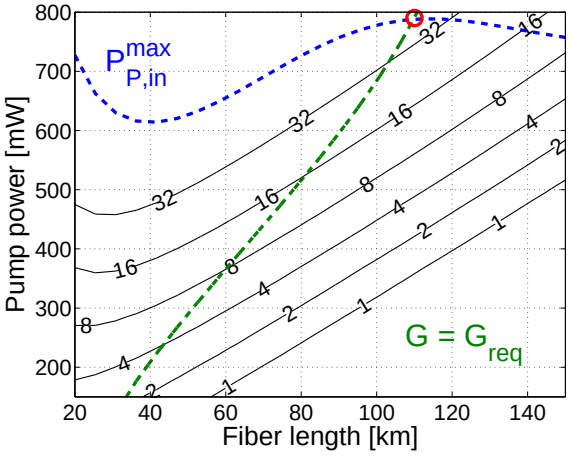

(e) Channel capacity

Figure 4.5.: Calculated results for a 50% bidirectionally pumped link.

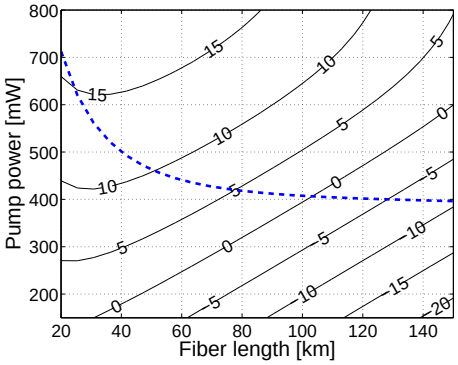

(a) Net gain (dB)

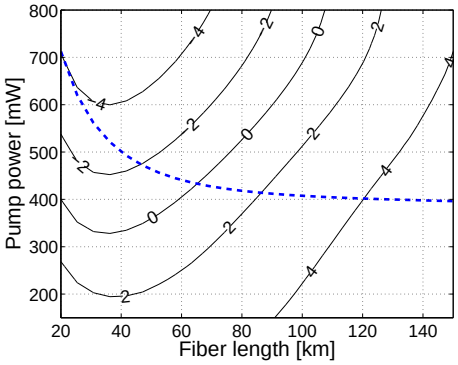

(b) SBS threshold power for ASK-NRZ (dBm)

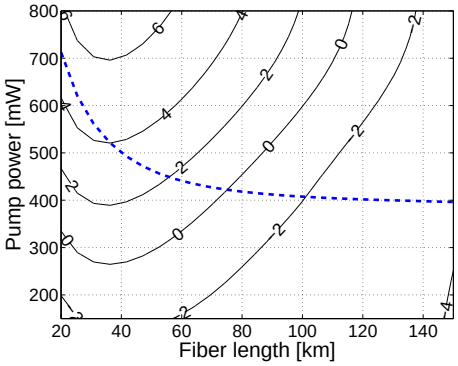

(c) Required gain (dB)

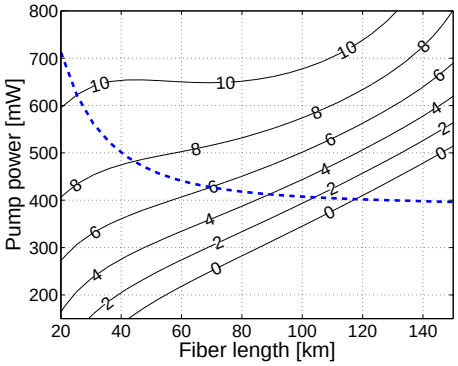

(d) Dynamic range (dB)

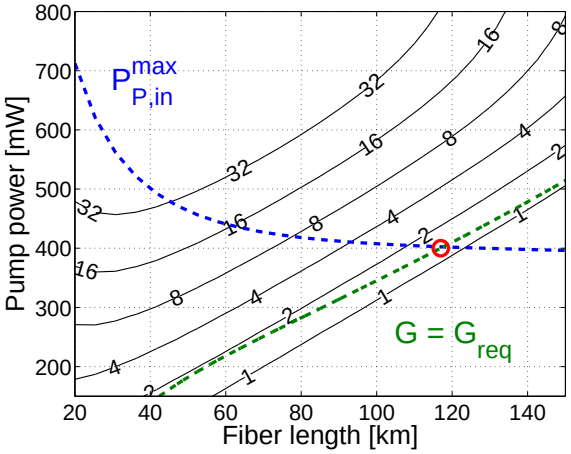

(e) Channel capacity

Figure 4.6.: Calculated results for an US pumped link.

Forward pump ratio	L_{max} [km]	$P_{p,in}$ [mW]	Channel capacity	P_{th} [dBm]	G [dB]	NF_{DS} [dB]	NF_{US} [dB]
1	34	400	19	-7.8	8.9	4.7	7.0
0.5	110	790	>32	-11.1	12.1	7.2	7.6
0	117	400	1	3.8	-2.9	21.2	7.0

Table 4.1.: Link parameters calculated at the point of maximum reach for a 100%, 50% and 0% forward pumped link.

tion meaning that increasing the pump power and lowering the signal input powers can be quite beneficial for avoiding SBS. The point of maximum reach is 117 km at 400 mW of pump power and is the longest reach found of the three configurations. The channel capacity at this point is less than two, however, which means that one would have to increase the total input power or reduce the fiber length to transmit more than a single channel pair.

4.2.4. Discussion and evaluation

Table 4.1 summarizes some important link parameters for the three pump configurations tested in this section. The parameters are calculated at the pump power and fiber length, L_{max}, corresponding to the point of maximum reach, marked with a red circle in Figs. 4.4–4.6 (e). From the table it is clear that DS pumping is not very suitable for extending the reach of existing PONs. On the other hand, to extend the link reach to a maximum and maintain a moderate pump level, US pumping is a good solution. Please keep in mind, however, that this analysis assumes the US channel input power to be 15 dB lower, i.e. much smaller, than the DS channel input power. To maintain a balance of a large channel capacity, $>$ 100 km reach and low noise figure, bidirectional pumping should be used. The trade off here is that pumps must be installed in two locations rather than one and that more pump power is required.

For all three configurations, the dynamic range at the point of maximum reach is one. This means the DS channel input power must be equal to P_{th}, which varies a lot between the configurations. For DS and bidirectional pumping, the channel input power must be relatively low, -7.8 dBm and -11.1 dBm, respectively, while maximum reach in an US pumped system requires almost 4 dBm of input power per channel. Finally, the high noise figure of 21.2 dB for the DS channels in the US pumped system should be

noted. Although this figure is high, the noise figure is still lower than the noise figure of a passive link followed by a discrete amplifier[1] and should not be a problem in these short range systems.

In these simulations, the total input power has been fixed at 5 dBm and -10 dBm for the DS and US channels, respectively. At these input powers, the link gain shows only moderate signs of gain saturation, depending on the pumping level. In general, the channel capacity was found to increase with the total input power, while we only observed a small input power dependence of the $G = G_{req}$ contour. In the limit of high input power (>10 dBm), $G = G_{req}$ contour was found to move toward shorter fiber lengths, the maximum pump power increased and the maximum reach was reduced due to increased gain saturation.

The considered fiber for the PON link in this context is TW-RS. The main reason is its high Raman gain efficiency and low dispersion parameter. By choosing a G.652 fiber instead, like SSMF, the sensitivity to DRB would be relaxed [27], but the price would be higher required pump power and required dispersion compensation. It should also be noted TW-RS has a better Raman gain spectral flatness than SSMF [27].

To support larger splitting ratios in the system, EDFAs could be used at the point between the link and local exchange. EDFAs are normally designed for one-way traffic, however, so such an addition would require the DS and US channels to be amplified separately using an amplifier/circulator pair - one for each signal direction. By using EDFAs in the local exchange, one would also need to pay attention to the US input power, which could limit the amount backward pumping to avoid SBS. Furthermore, due to the heavily saturated gain in these amplifiers, the EDFA gain would have to be carefully controlled to avoid unwanted cross gain effects between the channels. This point is discussed more in-depth in section 4.4.

In the simulations, the required channel output power for the DS channels, $P^{min}_{s,DS,out}$, was fixed at 1.0 dBm. This parameter determines the loss that can be tolerated in the passive part of the network and may change depending on the used splitting ratio, bit rate and receiver type. In the following, the effect of such a change is briefly discussed.

An increase in $P^{min}_{s,DS,out}$ has the following effect on the system results:

[1]The noise figure of system consisting of a passive lossy element with loss G_1, where $G_1 < 1$, followed by an amplifier with gain G_2 and signal-spontaneous noise figure NF_2, is given by [45]

$$NF = \frac{NF_2}{G_1} = \frac{2\rho_{ASE}}{G_1 G_2 h\nu_s}$$

where ρ_{ASE} is the optical power spectral density of the amplifier output ASE at the signal wavelength, h is Planck's constant and ν_s is the signal frequency. Setting $G_1 = -24$ dB, or approximately equal to the loss in 117 km of TW-RS, and $NF_2 = 3$ dB, the total noise figure of the system can be evaluated to $NF = 27$ dB.

- G_{req} scales linearly with $P^{min}_{s,DS,out}$ in (4.10) and will therefore increase with $P^{min}_{s,DS,out}$.
- The channel capacity and dynamic range scale inversely with $P^{min}_{s,DS,out}$ in (4.11) and (4.9), respectively, and these will therefore decrease.
- The $G = G_{req}$ contour in Fig. 4.4–4.6 (e) will move towards shorter fiber lengths and thereby lower the maximum reach of the system.

A change in $P^{min}_{s,DS,out}$ of a few dB will thus affect the values of L_{max} and the channel capacity somewhat, but will not change the overall conclusions made for the different pumping schemes.

4.3. Long-reach Raman PON architecture with 120 km reach

In this section, experimental results [90] regarding a bidirectional 10 Gbit/s per channel PON link with 120 km reach is presented. The single-fiber link is tested with two counter-propagating channels with identical input powers and bit rate. The fiber is bidirectionally pumped to provide positive net gain for both channels and no additional penalty due to bi-directional traffic is observed. The high on-off gain and good noise performance is obtained using a bidirectional pumping scheme with roughly 60% DS pumping. The link output powers indicate potential use in $>$ 100 km long reach PONs with low split ratio and high symmetric bandwidth to the end user. No dispersion compensation was used.

4.3.1. Experimental setup

The experimental setup is shown in Fig. 4.7. Two $LiNbO_3$ Mach-Zehnder modulators (MZMs) are used to generate the US and DS signals. The electrical signals are obtained from the data and inverted data outputs of a pulse pattern generator (PPG) and consists of a $2^{31} - 1$ pseudo-random bit sequence (PRBS) pattern. The center wavelengths of the US and DS channel are 1548.0 nm and 1550.4 nm, respectively. The PON link is composed of 120 km TW-RS with a total passive loss of 24.6 dB and a total chromatic dispersion of 550 ps/nm at 1550 nm. The employed optical receiver consists of a 0.8 nm bandpass filter (BPF) placed before PIN photodiode, which is connected to the bit-error rate testset (BERT). No optical preamplification is used in the receiver.

The US and DS signals are coupled into the PON link using two optical circulators placed at each end of the link. Before transmission, the signals

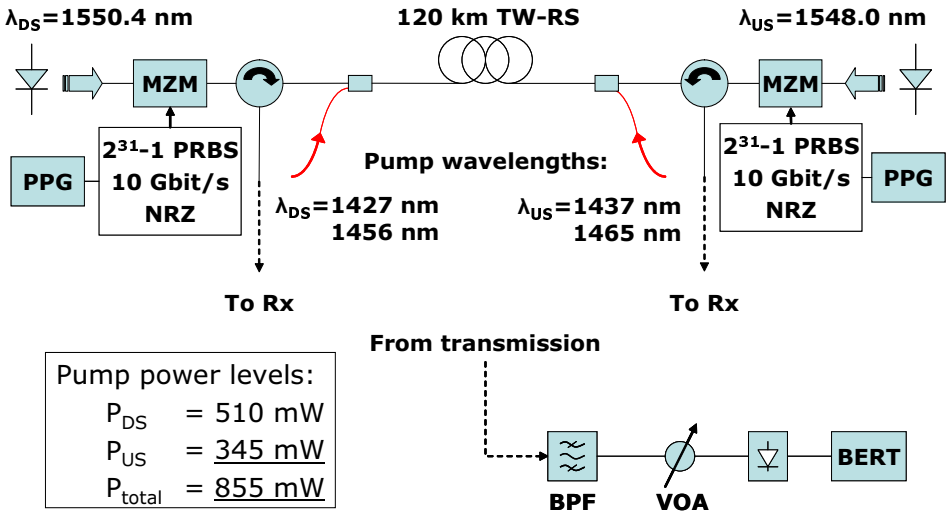

Figure 4.7.: Experimental setup of the bi-directional 120 km PON link.

are combined with two co-propagating Raman pumps using a coarse wavelength division multiplexer (CWDM). In this setup, the channels will see both co- and counter-propagating pumps during transmission. The US and DS signal power into the link (measured after the CWDM) is -1.3 dBm and -2.3 dBm, respectively. The wavelengths of the upstream pumps are 1437 nm and 1465 nm and the optical input powers are 165 mW and 180 mW. The wavelengths of the downstream pumps are 1427 nm and 1456 nm with respective input powers of 231 mW and 279 mW. At the end of the link, the circulator routes the signal to the receiver, where an optical BPF is used to reject the ASE and back scattered power from the counter-propagating channel.

4.3.2. Results and discussion

Fig. 4.8 (a) and (b) show the spectra measured at the fiber ends corresponding to the US and DS channel outputs, respectively. A substantial amount of channel light is seen to be reflected back from the link. The DS channel reflects the most light, -10 dBm, while the reflected power from the US channel peaks at -24 dBm. Inspection of the reflected spectra reveals that the longer-wavelength 10 GHz clock tone is significantly larger than the shorter ditto. The enhanced clock tone of the reflected DS spectrum is even 5 dB larger than the carrier. The large amount of reflected power combined with the significantly enhanced longer-wavelength clock tone shows that channels suffer nonlinear loss from SBS. The 10 GHz frequency separation

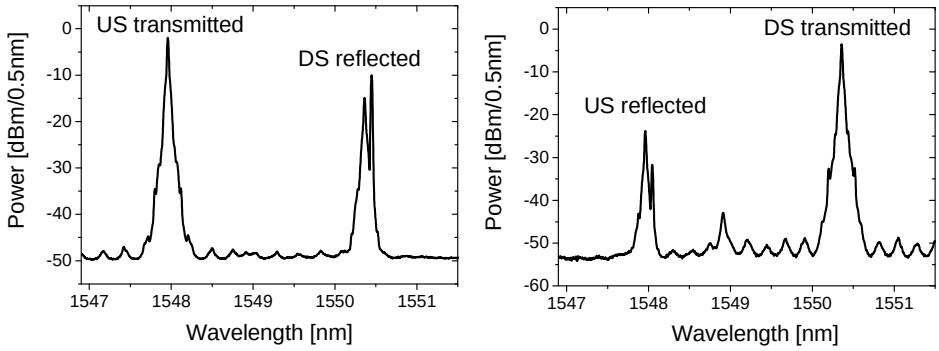

Figure 4.8.: (a) and (b) measured output spectra at the two fiber ends.

Channel	P_{in} [dBm]	G^{bi}_{on-off} [dB]	G^{bi} [dB]	G^{uni} [dB]
US	-1.3	27.5	2.9	3.3
DS	-2.3	26.8	2.2	2.4

Table 4.2.: Uni- and bi-directional gain of the two channels.

between the carrier and clock tone corresponds to the typical Stokes shift in a Brillouin amplifier [91] and effectively causes the carrier to act as a pump for the counter-propagating Stokes light at the clock frequency. Although SBS is clearly an issue at these channel input powers and pumping levels, the effect on the BER was not significant, as will be shown in the following.

The measured gain of both channels are summarized in table 4.2. In the bi-directional case, when both the US and DS channels are on, the net gain is measured to 2.9 dB and 2.2 dB, respectively. The corresponding on-off gain is 27.5 dB and 26.8 dB, which gives rise to a signal power at the output of the link of 1.6 dBm and -0.1 dBm for the US and DS channel, respectively. The received optical signal-to-noise ratio (OSNR) (noise spectral density measured in a 0.1 nm resolution bandwidth) is measured before the BPF and is found to be 40.9 dB and 41.9 dB for the US and DS channel, respectively. With only a single channel turned on (uni-directional case), the gain and OSNR of both channels increase by 0.2 dB, thereby indicating a very low level of gain saturation.

Eye diagrams measured before and after transmission, using the optical input of a high-speed sampling oscilloscope, are shown in Fig. 4.9 (a), (b), (c) and (d). A BPF is used in front of the oscilloscope to select the channel and reject ASE noise and reflections. Notable pulse broadening due to fiber dispersion is detected, but the eye is still wide open after 120 km

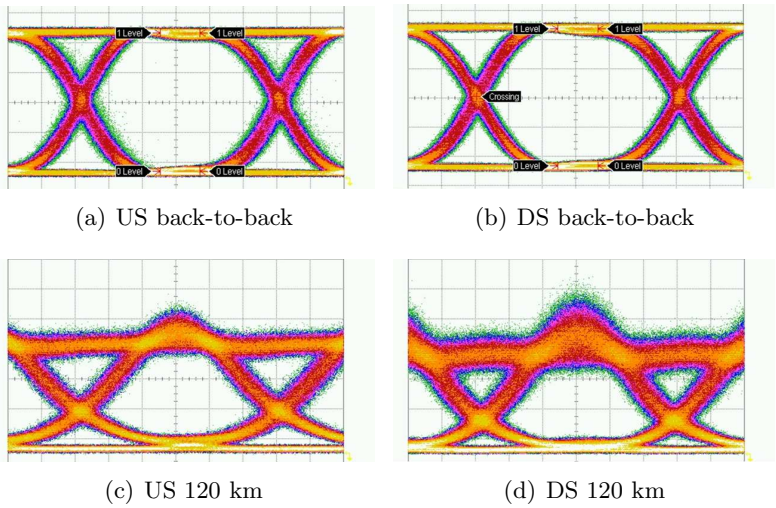

(a) US back-to-back (b) DS back-to-back

(c) US 120 km (d) DS 120 km

Figure 4.9.: Measured eye diagrams before and after transmission. Time scale is 16.3 ps/div – 17.0 ps/div.

transmission ($\sim$ 550 ps/nm) without dispersion compensation. The 1 dB penalty due to dispersion has been found to be $\sim$ 950 ps/nm for 10 Gbit/s ASK-NRZ signals [55]. Compared with the transmitted US signal in Fig. 4.9 (c), the transmitted DS signal is seen to suffer from additional 1-bit noise in Fig. 4.9 (d). This additional noise is attributed to the mild degree of SBS, which was detected in the reflected spectra of the DS channel.

Measurements of BER as a function of input power are shown in Fig. 4.10 for both channels. The channels have been characterized in the case of back-to-back (after the transmitter), after uni-directional transmission and after bi-directional transmission. The sensitivity is defined as the minimum power at which a BER of 10^{-9} can be obtained. The back-to-back sensitivities are -18.8 dBm and -19.6 dBm, for US and DS channel, respectively. After unidirectional transmission, a sensitivity penalty of 0.8 dB (US) and 0.9 dB (DS) is found. For the bidirectional case, the penalty is 0.7 dB (US) and 0.8 dB (DS), compared to back-to-back. All in all, penalties of less than 1 dB are found in all four cases and no performance degradation is found when comparing bi- to uni-directional transmission. From this, we can also conclude that the total fiber dispersion is not a problem at this reach distance.

An estimated output power of 1 dBm per channel would be required if the link were to be used in PON applications, as discussed in section 4.1.1. The present link is almost capable of this with measured channel output powers of 1.6 dBm and -0.1 dBm. Although no significant penalty

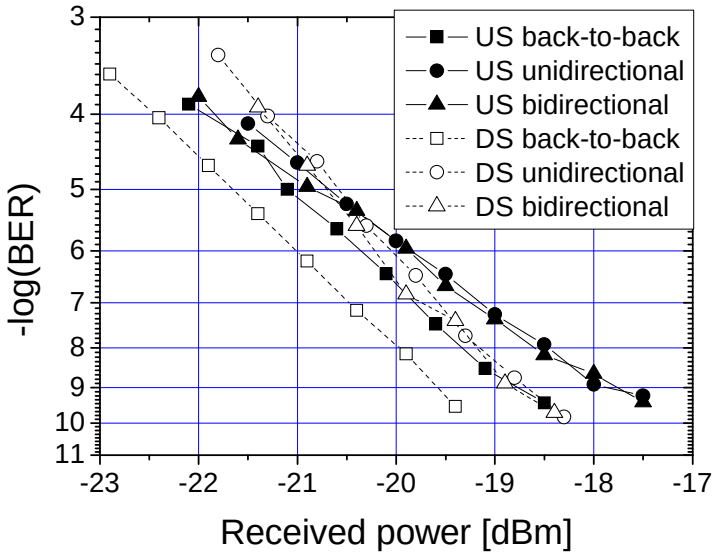

Figure 4.10.: BER as a function of received power for the up- (solid) and downstream (dashed) channels.

in receiver sensitivity is found after transmission, the measured spectra and eye diagrams indicate that SBS is a beginning problem in this particular link configuration. To reduce the effect from SBS and maintain the 120 km reach, the slope of the contours in Fig. 4.5 (e) suggests that increasing the pump power and lowering the input power will reduce the effect from SBS while still maintaining a high output power.

When comparing with the simulation results for the same fiber length and gain in Fig. 4.5 (e), it is interesting to note that the experimental demonstration at 120 km exceeds the limitations set by the $G = G_{req}$ contour with > 30 km, but with very little penalty. Assuming that the calculated values of P_{th} are close to the experimental values, this indicates that SBS-induced penalties only become significant at input powers that are several dB's larger than P_{th}.

It should be mentioned that phase modulation is a well-known technique for broadening the signal spectrum and thereby increase P_{th} for a single channel by several dB's. Because this technique requires an additional phase modulator as well as several synthesizers to generate the high-frequency modulation tones [93], we have chosen not to consider this technique in the context of the long-reach Raman PONs, where system cost is expected to be the most important parameter.

To summarize, a simple design for a long-reach PON link has been tested, based on a single bi-directional NZDSF fiber employing distributed Raman

amplification. After 120 km of transmission, without any use of dispersion compensation, we find received OSNR values in excess of 40 dB, transmission penalties limited to $\sim$ 0.8 dB and no increased penalty due to the bi-directional operation. To conclude, we find the bidirectional long-reach PON link to be an excellent candidate for future long-reach access systems with more than 100 km reach.

4.4. Dynamic performance

The long reach, or super, PON is a promising way to reduce the cost and increase the bandwidth of future access networks [86, 94]. In the previous sections, it was demonstrated how DRA can be used to extend the reach of today's PONs. Apart from the static performance of these networks, future PONs will also have to accommodate rapid changes in traffic demands from the end users, as well as the slot-based and discontinuous upstream traffic [95]. Due to cross-gain modulation (XGM), fluctuating input power of a single channel will cause output power fluctuations of neighboring channels in a saturated amplifier. These power fluctuations occur over a certain transient time and can lead to output power bursts which may result in receiver burst-errors or even damage to the receiver [96]. Systems relying on FEC will be particularly vulnerable to power transients, as the burst-error correction capability of standard interleaved Reed-Solomon code structure is insufficient to correct the resulting bit errors for typical slow amplifier transients (0.1 ms) [97].

To avoid the cost of transient control in deeply saturated amplifiers, such as EDFAs, a highly linear amplifier would therefore be an attractive candidate for future PON links. Linear amplifiers based on gain-clamped SOAs [98] and combinations of SOAs and discrete Raman amplifiers [99] have recently been proposed for PON and metro applications. Although very good burst-mode performance has been demonstrated using these amplifiers, the results have been limited to output powers up to 7.5 dBm, unrepeated reach up to 60 km and unidirectional amplification. As an alternative to these amplifiers, it is well-known that DRA features high input saturation power (see Fig. 2.11 on page 36). As a result, DRA has been proposed for metro applications by Aoki et al., due to its highly linear gain properties and flexible gain bandwidth [100].

In this section, we study the dynamic properties of a bidirectionally Raman pumped PON link, employing NZDSF and no gain control. The link is tested under burst-mode conditions, using two strong neighboring channels, which are periodically on-off modulated to "disturb" a surviving data channel in both a co- and counter-propagating configuration. The number of

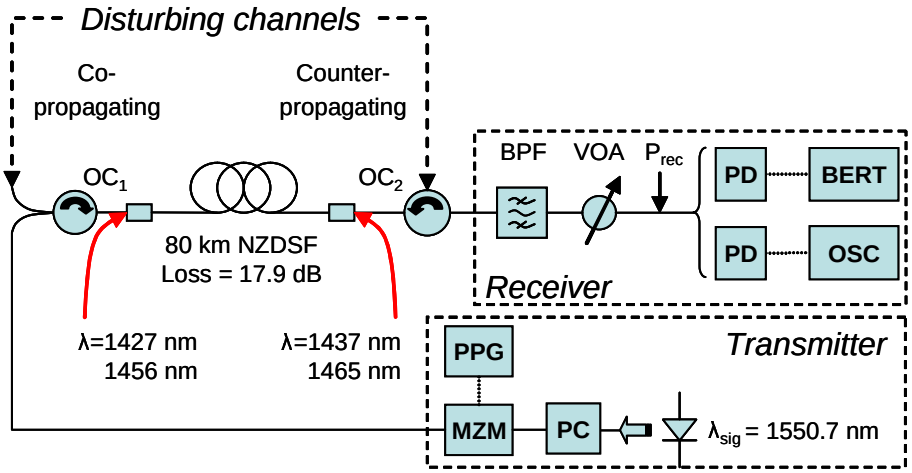

Figure 4.11.: Experimental setup used to measure BER and power transients.

disturbing channels is emulated by varying the input power of the disturbing channels. The resulting effect is characterized in terms of output power transients and receiver sensitivity penalties, for the surviving data channel. The transients are also studied using the numerical model, described in chapter 2 and the calculated results agree well with the measured power transients. The model is furthermore used to explain the reduced penalty found in the case of counter-propagating disturbance.

4.4.1. Experimental setup

The experimental setup used to measure BER and output power transients from the symmetric PON link is shown in Fig. 4.11. The link consists of 80 km of TW-RS, featuring low dispersion of 4.6 ps/nm/km at 1550 nm and high Raman gain efficiency of 0.71 $W^{-1}km^{-1}$. The Raman pump light is coupled into the link at each end using two CWDMs. The CWDMs and the fiber add up to a total link loss of 17.9 dB. The pump wavelengths are chosen so they provide gain in the entire C-band and the total pump power is 233 mW and 221 mW in the co- and counter-propagating direction, respectively. The pumps provide a small-signal on-off gain of 22.0 dB, corresponding to a small net gain of 4.1 dB. The highly linear gain of the DRA-based link is confirmed a measurement of the static 3 dB input saturation power of the link of 11 dBm.

A distributed feedback (DFB) laser at 1550.7 nm is used as the data channel source. The polarization is optimized using a polarization controller (PC) prior to entering the MZM, which is controlled by a PPG. A 10 Gbit/s

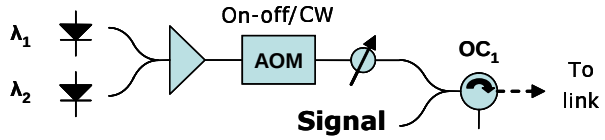

(a) Co-propagating

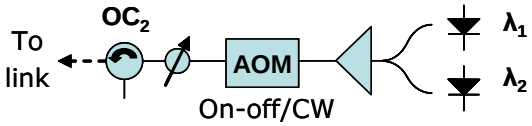

(b) Counter-propagating

Figure 4.12.: (a) Co- and (b) counter-propagating disturbing channel setup.

NRZ signal is encoded with a 2^7-1 PRBS. From here, the signal is combined with the disturbing channels using a 3 dB coupler and fed into the link via an optical circulator, OC_1. The signal input power is fixed at -2 dBm. In this work, the data channel resembles either an US or a DS channel which is subjected to XGM from the on-off switching of the neighboring channels. It should be noted that US channels typically have input powers lower than -2 dBm, due to high splitting loss in the access network, but as long as the channel input power is far below the saturation input power of the link, the conclusions will be the same in these two cases. The receiver consists of a BPF followed by a variable optical attenuator (VOA), which is used to adjust the input power to the photodiode and BERT. To characterize and save the transient waveforms, a low bandwidth (100 MHz) photodiode is used along with an oscilloscope (OSC).

The signal is disturbed using two neighboring channels positioned at $\lambda_1 =$ 1549.1 nm and $\lambda_2 =$ 1552.3 nm. The disturbing channels modulate the saturable gain through XGM. The two test configurations are shown in Fig. 4.12 (a) and (b), where the channels co- and counter-propagate with the signal, respectively. The CW channels are on-off modulated at 500 Hz with a 50% duty cycle using an acousto-optic modulator (AOM) with ns response. The two channels have similar power levels and the sum of the channel peak powers into the span, the so-called *disturbing power*, is regulated using a VOA.

4.4.2. Results and discussion

Fig. 4.13 (a) and (b) show measured and calculated output power transients of the signal channel, when co- or counter-propagating disturbance

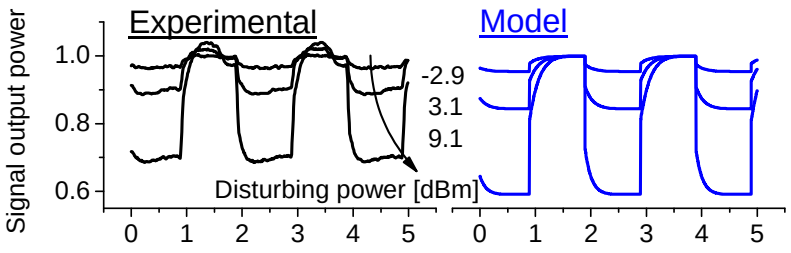

(a) Co-propagating disturbance

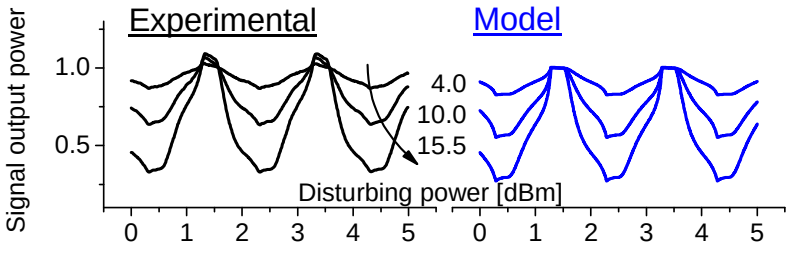

(b) Counter-propagating disturbance

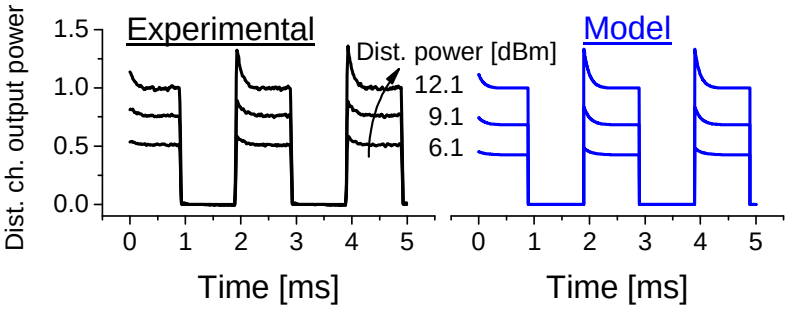

(c) Disturbing channel output

Figure 4.13.: Measured and calculated output power transients due to different levels of disturbance power. The power scale is normalized and in linear units.

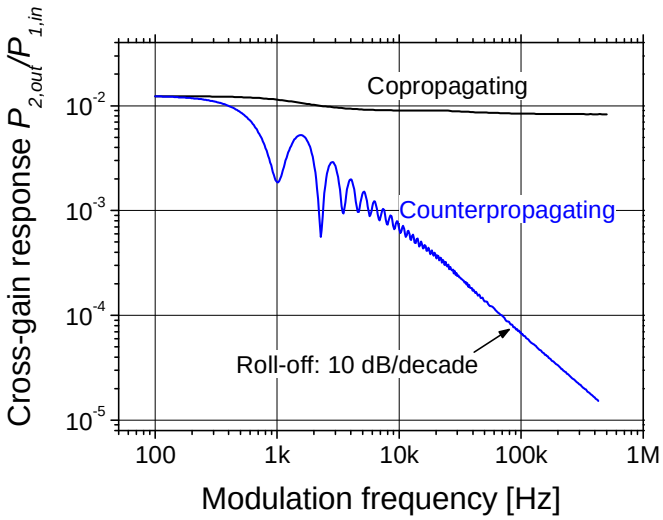

Figure 4.14.: Calculated small-signal cross-gain response for a channel with co- and counter-propagating disturbance, in a bidirectional pumped link.

is used, respectively. The levels are normalized so that unity output power corresponds to the unsaturated gain. Fig. 4.13 (c) shows the output of the co-propagating disturbing channels. In Fig. 4.13 (a), (b) and (c), the three traces correspond to different levels of disturbance power and the values in dBm are shown in the figures. The left column shows the measured traces, while the right column shows traces calculated using the numerical model and using the same disturbing powers. The model uses a single pump wavelength and the same forward pump ratio, as in the experiment. The total pump power is adjusted to match the gain in the experiment.

Apart from the small signal overshoots found in the measurements at high disturbance powers, very good agreement is found between experiment and model, for all three types of transients. There is a distinctive difference between the signal transients developed in the two cases, in Fig. 4.13 (a) and (b). In the co-propagating case, the power changes from saturated to unsaturated output power in the order of $\sim 400\mu$s. This time corresponds to the transit time of the 80 km link. In the counter-propagating case, the transients develop over twice the transit time, i.e. close to 1 ms. The resulting transient shapes can be considered to be the result of a filtering effect, as will be explained in the following.

Fig. 4.14 shows the calculated cross-gain response of a weak probe (signal) channel experiencing a gain modulation imposed by strong pump channel. The pump channel is modulated with a small sinusoidal modulation. The response is calculated using the amplifier model with the same pump and

link parameters as used in the calculation of Fig. 4.13. The cross-gain response, S_{21}, is defined as the ratio of the modulation amplitude of the probe at the output, $P_{2,out}$, and that of the pump channel at the input, $P_{1,in}$, i.e.

$$S_{21} = \frac{P_{2,out}}{P_{1,in}} \tag{4.12}$$

While the response is practically flat in the co-propagating case in Fig. 4.14, the crosstalk is seen to be effectively low-pass filtered in the counter propagating configuration, with a cut-off frequency close to 1 kHz. The low-pass filter response is a result of rapid walk-off between the counter-propagating pump and probe channel and is seen to roll-off with 10 dB/decade. If dispersion was included in the model, the co-propagating cross talk would also be filtered, but with a much higher roll-off frequency than in the counter-propagating case. The XGM roll-off frequency has been calculated for 80 km purely forward-pumped TW-RS and found to be close to 100 MHz [53], which is well beyond the frequencies considered here. The reason why the co-propagating response is not entirely flat in the considered range is most likely that the low frequency XGM response for two co-propagating channels in a counter-pumped amplifier is higher than in a co-pumped amplifier [53]. In the low frequency range, the response is therefore dominated by counter-propagating pump-mediated crosstalk, while the crosstalk mediated by the co-propagating pump dominates in the high-frequency range. The not-so-flat response is therefore a signature of bidirectional pumping. The dips and peaks in the counter-propagating response are a result of the effective gain length determined by the loss and length of the fiber and is explained in more detail in [33].

Measured eye diagrams of the data channel after transmission and filtering are shown in Fig. 4.15. Co- and counter-propagating disturbance has been used in the top and bottom row of the figure, respectively, and the disturbing power is in both cases varied between 1 dBm, 7 dBm and 10 dBm. The faster transients associated with co-propagating disturbance are seen to give rise to two separate one-bit levels in the top row of Fig. 4.15, while the slower transients in the counter-propagating case give rise to a more homogeneously broadened one-bit level, in the bottom row of Fig. 4.15. Some broadening due to dispersion can also be detected.

Four measured BER curves are shown vs. received power in Fig. 4.16. Sensitivities of -20.4 dBm and -19.4 dBm are found in the case of back-to-back and after transmission with no disturbance, respectively. At 11 dBm of co-propagating disturbance power, an error floor is observed to appear, as a result of transient-induced eye-closure. For counter-propagating disturbance, no sign of error floor is seen at 13 dBm of disturbance power.

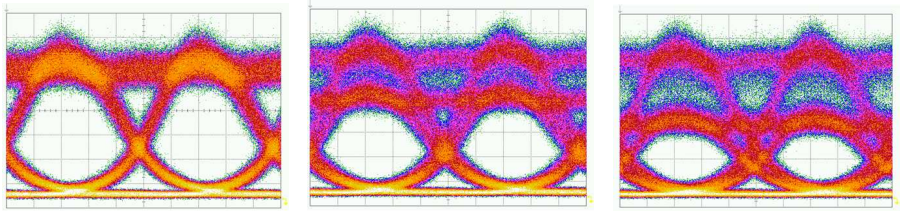

(a) Co-propagating disturbance, 1 dBm

(b) Co-propagating disturbance, 7 dBm

(c) Co-propagating disturbance, 10 dBm

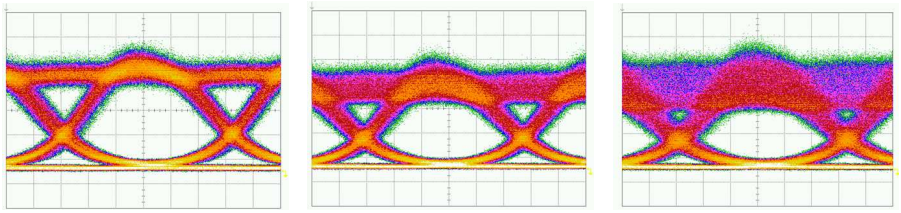

(d) Counter-propagating disturbance, 1 dBm

(e) Counter-propagating disturbance, 7 dBm

(f) Counter-propagating disturbance, 10 dBm

Figure 4.15.: Data channel eye diagrams measured after transmission with co- and counter-propagating disturbance. The disturbance power is 1 dBm, 7 dBm and 10 dBm. Time scale is 20 ps/div and 16.2 ps/div – 17.2 ps/div, when co- and counter-propagating disturbance was used, respectively.

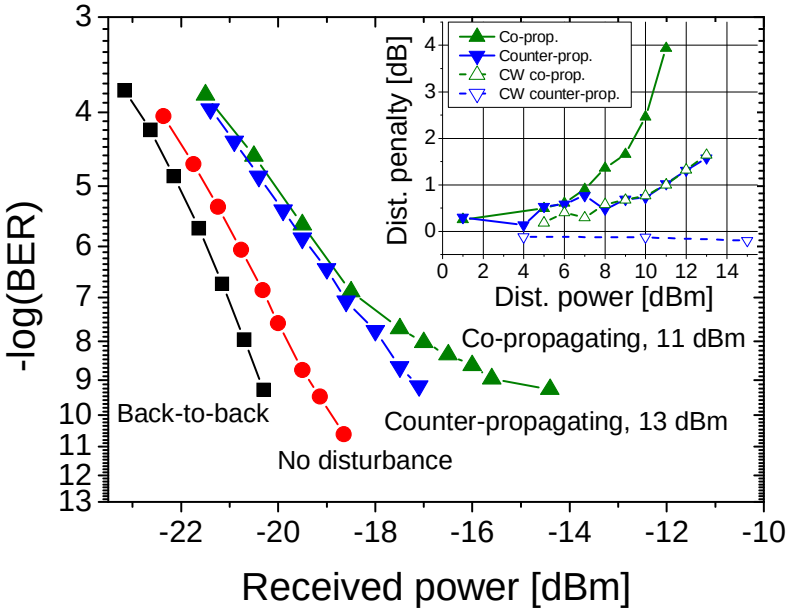

Figure 4.16.: BER vs. received power. (Inset) Receiver sensitivity penalties, measured at a BER of 10^{-9}, vs. disturbance power.

The receiver sensitivity penalties at a BER of 10^{-9} and due to transmission with co- or counter-propagating disturbing channels are shown in the figure inset as a function of disturbance power. The filled symbols mark the use of on-off disturbance, while the hollow symbols indicate that CW disturbance is used, i.e. the channels are not modulated.

Two main conclusions can be drawn from the inset. Firstly, that on-off disturbance is worse than CW disturbance and secondly, that co-propagating disturbance is worse than counter-propagating disturbance. With less than 7 dBm of disturbance power, the penalties are in all four cases less than 1 dB, which indicate the high dynamic tolerance of the link. If the 7 dBm is converted into a corresponding number of disturbing channels with -2 dBm of input power (same as the signal channel), this disturbing power corresponds to simultaneous on-off modulation of 8 out of 9 channels, with no more than 1 dB penalty.

As the disturbing power is increased up to 11 dBm, however, the penalty due to co-propagating on-off disturbance approaches is 4 dB and the co-propagating on-off disturbance scheme clearly turns out to be a worst-case scenario. The best scenario, on the other hand, is counter-propagating CW disturbance, where no, or even slightly negative, penalty can be detected. The reduced penalty in the counter-propagating case is attributed to the low-pass filtering of the transients, as previously discussed, while the penalty

due to the CW disturbance is attributed to the employed coherence control, which was used to broaden the disturbing channel spectrum to prevent SBS. The coherence control was observed to also result in some amplitude modulation of the disturbing channels and was therefore found unsuitable for use with data modulation.

All in all, we conclude that the proposed Raman PON link shows good burst-mode tolerance without any use of active gain control. We thus find the receiver sensitivity penalty to be acceptable and less than 1.0 dB, even in a worst-case scenario, corresponding to the periodic and simultaneous adding and dropping of 8 out of 9 co-propagating channels.

4.5. Summary

A new architecture for extending the reach of today's passive optical networks (PONs) by using distributed Raman amplification in the long-reach PON link has been proposed and demonstrated. The maximum reach and channel capacity of the system has been numerically modeled and it was found that more than 100 km reach can be obtained by using US pumping. Long reach combined with a large channel capacity can be obtained, if bi-directional pumping is used. DS pumping was found to be poor solution for extending the reach of these systems, due to the low overall gain and limitations from SBS, in this scheme. To emphasize the long reach of the Raman PON architecture, a 120 km bidirectionally pumped link with symmetric 10 Gbit/s traffic, was experimentally demonstrated, with high channel output powers and low transmission penalties of less than 0.8 dB.

The dynamic performance of an 80 km bidirectional Raman PON link has been experimentally tested with 10 Gbit/s burst-mode traffic. The highly linear gain properties of the link was found to make it robust towards dynamic adding and dropping of neighboring channels. As such, the disturbance penalty on a surviving channel was found to be less than 1.0 dB, in the worst-case scenario, where a co-propagating disturbing power, corresponding to 8 channels, was periodically on-off modulated.

To conclude, we believe that the proposed Raman-based PON link should be regarded a serious contender for future, high-capacity links in PONs with burst-mode traffic.

5. Inter-channel crosstalk and transient effects

In saturated amplifiers, transient crosstalk is generated between adjacent channels, when the average power into the amplifier changes abruptly. This type of crosstalk can be a serious problem in today's reconfigurable networks where reconfigurable optical add/drop multiplexers (ROADMs) and optical cross connects are used for dynamic routing and switching of individual channels. The involved switching puts severe demands on the dynamic properties of the network amplifiers, and if the amplifier gain is not well-controlled at the channel-level, dynamic channel add/drops will cause network amplifiers to respond with power transients at their outputs [9]. In general, transients are always unwanted in a system, as they impair the receiver sensitivity [92,101], can cause potential damage to system components and increase the effect from system nonlinearities during transmission.

In this chapter, the main topic is inter-channel crosstalk arising from cross-gain modulation (XGM) in fiber-based amplifiers. In particular, the focus is on a newly developed method for all-optical equalization of power transients, on a channel basis. The chapter is structured as follows: Section 5.1 describes why and how transients arise in networks with switched traffic. Section 5.2 discusses how transients, arising from crosstalk in fiber Raman amplifiers (FRAs) and erbium-doped fiber amplifiers (EDFAs), can impair the signal transmission and detection. Finally, sections 5.3, 5.4 and 5.5 describe the principle, the design and an experimental demonstration of the developed transient equalizer.

5.1. Crosstalk in saturated amplifiers

Two signal channels propagating in the same active (i.e. amplifying) waveguide can induce crosstalk through XGM. XGM is a result of the saturable gain inherent to all amplifiers and reflects that the gain experienced by each channel draws upon the same limited power reservoir. If the reservoir is depleted by one channel, the gain of the neighboring channels will also be affected. In FRAs, the gain at a specific location in the fiber depends on the instantaneous pump power at that location. Because the pump power can be co- or counter-propagating with the signal channel, the amount of pump

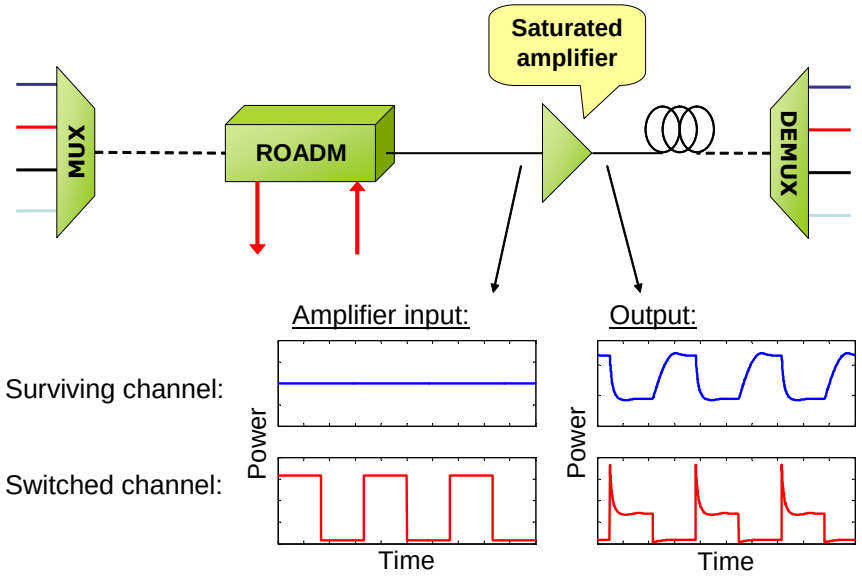

Figure 5.1.: The generation of power transients on a surviving and switched channel, in a saturated amplifier.

depletion and crosstalk will depend on the relative propagation direction of the signals and pumps.

Fig. 5.1 illustrates how transient waveforms can be generated in a network situation. The figure shows a point-to-point system with four co-propagating wavelength division multiplexed (WDM) channels. A ROADM, located prior to a saturated optical amplifier, periodically adds and drops (switches it on and off) one of the WDM channels. The resulting waveforms of the surviving and switched channels, at the amplifier input and output, are shown below the setup. The waveforms are calculated for a backward pumped dispersion compensating Raman amplifier (DCRA), where the input power of the switched channel is much larger than the input power of the surviving channels. The waveforms should be regarded as envelopes of the average signal power and contain modulated data with a bit rate that is much faster than the time scale of the waveform transient. Details of the simulation is left out here for illustrative purposes and more detailed descriptions of this type of crosstalk will be provided later in the chapter.

Due to inter-channel crosstalk through the saturated amplifier gain, the power of the surviving channel at the output of the amplifier is seen to oscillate out-of-phase with the output of the switched channel. Furthermore, the switched channel output now includes a large power spike, or overshoot, at the beginning of the envelope pulse. The spike is a result of the unsaturated amplifier gain experienced by the leading edge of the envelope pulse before

the gain starts saturating.

Transients, like the ones shown in Fig. 5.1, are generated when signals with fluctuating power is injected into a saturable amplifier. Power fluctuations can arise in reconfigurable networks, where the use of switching nodes are an inherent part of the network, or as a result of channel reconfiguration, or simply due to discontinuous traffic, as described in chapter 4. Power fluctuations can also occur due to network faults, such as e.g. cable cuts. An additional problem is that transients are known to build-up along both erbium- and Raman-amplified transmission links [102, 103], although to a much smaller extent in Raman-amplified links than in links with EDFAs [11]. It is therefore important that power transients are well-controlled and are not allowed to propagate through several amplified spans without mitigation.

The transient magnitude and shape depends to a large extent on the amplifier configuration and how well the gain is controlled. Because EDFAs tend to run in heavy saturation, small changes in the input power can result in relatively large output power spikes that give rise to burst errors at detection [101]. Automatic gain control can be used to mitigate this problem and, with constant monitoring of the total input or output power, automatic gain control in EDFAs with a response time of a few μs was demonstrated by Sun et al. in 1999 [104]. Using this technique, transient overshoots of single channel were reduced to a few tenths of a dB by control of the pump lasers. However, this way of controlling transients is not a trivial task and today, almost 10 years after these results were published, transients still seem to be a problematic issue in newly deployed 40 Gbit/s networks, in spite the use of automatic gain control [105]. One problem with automatic gain control is that it only keeps the total gain constant and not the individual channel gain. In the worst case, the channel dependence of the gain control efficiency can thus lead to oscillations and instabilities in the channel power control [106]. Furthermore, it has been shown that the optimal feedback control parameters for a single amplifier do not lead to optimal results for cascaded EDFAs [107]. For a system designer this implies that the controller parameters should not only be optimized for a single EDFA, but also for a chain of EDFAs where the transient power fluctuations have accumulated, which is challenging in a complex reconfigurable network.

For FRAs, automatic gain control has been demonstrated for both backward and forward pumped amplifiers [108, 109]. Although the literature on transient propagation in cascaded Raman-amplified links is very limited [11, 110], it indicates that transient evolution in Raman amplified links is also channel dependent [110]. This means that a simple pump control scheme, which affects many channels simultaneously in FRAs, due to its ~ 30 nm gain bandwidth, will not be an effective technique for mitigating

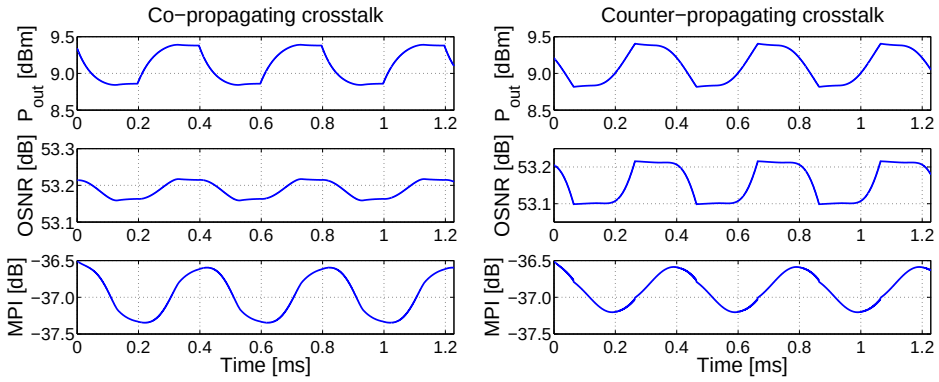

Figure 5.2.: Calculated DCRA output power, OSNR and MPI for a surviving channel subjected to crosstalk from a (a) co- and (b) counter-propagating switched channel. The DCRA consists of 14 km DCF for SSMF pumped with 250 mW of pump power. The pump is *counter*-propagating with the surviving channel and centered at 1453 nm. The peak input power of both channels is -1.8 dBm and the wavelengths of the surviving and switched channel are 1549.2 nm and 1550.8 nm, respectively.

transients on a channel basis.

5.2. Transient impairments

Much work has already been done in understanding the nature and shape of transients arising from inter-channel crosstalk in fiber-based optical amplifiers. The reader is therefore referred to the work by Desurvire, Sun and Bononi for a discussion of transient crosstalk in EDFAs [104, 111, 112] and to the work by Chen, Bononi and Karásek [113–115] for crosstalk in FRAs.

In this section, calculated and measured output power transients in DCRAs and EDFAs without gain-control are compared with regard to the transient magnitude and system impairments. In order to make an experimental comparison, we focus on the surviving channel transients, as the channel data of these channels are not bursty and therefore much easier to detect experimentally, i.e. they do not require a burst-mode receiver to be detected.

5.2.1. DCRA simulations

Fig. 5.2 (a) and (b) shows calculated waveforms of output power, optical signal-to-noise ratio (OSNR) and multi-path interference (MPI) noise, due

to double Rayleigh backscattering (DRB), for a surviving channel subjected to inter-channel crosstalk in a DCRA. The OSNR and MPI is defined according to eq. (2.42) and (2.43), respectively. In Fig. 5.2 (a) and (b), the crosstalk stems from a co- and counter-propagating on-off modulated (switched) channel, respectively. The modulation frequency of the switched channel is 2.5 kHz. The DCRA consists of 14 km dispersion compensating fiber (DCF) for standard single-mode fiber (SSMF), and this is pumped with 250 mW of pump power. In both cases, the pump is *counter*-propagating to the surviving channel and centered at 1453.0 nm. The input power of both channels is -1.8 dBm and the wavelengths of the surviving and switched channel are 1549.2 nm and 1550.8 nm, respectively.

It is clear that inter-channel crosstalk causes both the output power, OSNR and MPI to oscillate with time. The shape of the transients is a result of the complex interplay between the pump and signals and depends especially on the transit time of the fiber [114]. In both channel configurations, the maximum output power variation of the surviving channel is 0.6 dB, while the maximum variation of the OSNR and MPI are ~ 0.1 dB and ~ 0.9 dB, respectively. It is interesting to note that the variation of the OSNR is notably smaller than the power variation in these amplifiers. This shows that the amplified spontaneous emission (ASE) at the amplifier output is also modulated and its variations follow the signal power closely. Similarly, it is worth noting that the variation of the MPI is larger than the output power variation.

We have also modeled co- and counter-propagating crosstalk in DCRAs with a pump that co-propagates with the surviving channel. In these configurations, we found the maximum output power variation to be similar to the previously mentioned, while the maximum variation of the MPI and, in particular, OSNR was found to be notably smaller.

These transient variations in power, OSNR and MPI can all affect the optimum decision threshold in a receiver and, as such, impair the receiver sensitivity. For this type of crosstalk, however, we expect phase-shift-keying (PSK) modulation using balanced detection to be more robust than amplitude-shift-keying (ASK) modulation, since the decision threshold for PSK is fixed at ~ 0 V and does not depend on the received power.

5.2.2. EDFA measurements

Fig. 5.3 (a) shows crosstalk-induced power transients of a surviving channel measured at the output of a commercial power-controlled EDFA. The crosstalk is induced by a switched co-propagating channel with a peak input power that is varied between -5.8 dBm and -0.8 dBm. The input power of the surviving channel is -1.8 dBm and the switching frequency is 5 kHz.

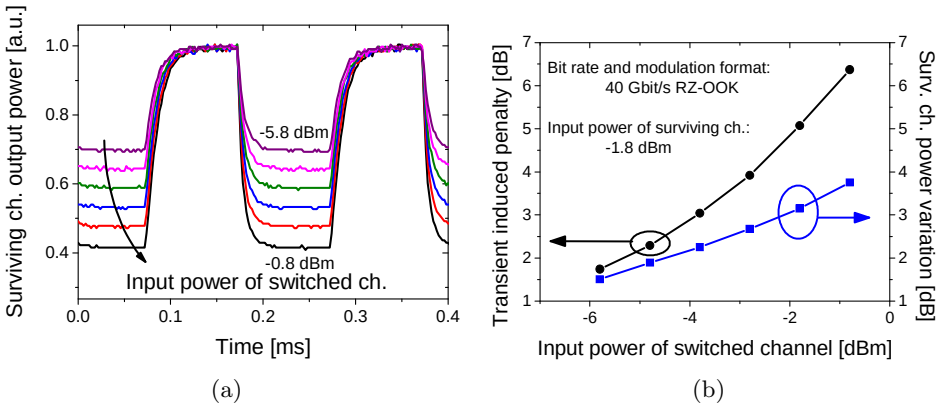

Figure 5.3.: (a) Measured transients due to crosstalk between a switched and co-propagating surviving channel in a power-controlled EDFA. The input power of the surviving channel is -1.8 dBm while the input power of the switched channel is varied.
(b) Induced penalty and transient power variation vs. input power of the switched channel.

The wavelength separation between the two channels is 6.3 nm.

The measured power variation of the surviving channel transient is extracted from Fig. 5.3 (a) and shown as a function of the switched channel input power, in Fig. 5.3 (b) (right axis). The power variation increases steadily with the switched channel input power and is 3.1 dB, when the input power of both channels is -1.8 dBm. The left axis in Fig. 5.3 (b) shows the receiver sensitivity penalty at a bit-error rate (BER) of 10^{-9}, for a 40 Gbit/s return-to-zero (RZ)-on-off-keying (OOK) signal that is impaired by the transient. The penalty (in dB) is seen to rise faster than the corresponding power variation (also in dB), as the input power of the switched channel increases. The maximum penalty found is 6.4 dB and this is associated with a power variation of 3.8 dB. The results show that transients can clearly induce large sensitivity penalties and also that the induced penalty can be substantially larger than the power variation.

Comparison The 3.1 dB output power variation from the EDFA, when the input power of both channels is -1.8 dBm, can be compared to the simulated 0.6 dB power variation obtained with the DCRA, in the previous section. The comparison suggests that EDFA induced transients are larger and more easily generated compared to the same in a FRAs under the same input power conditions. That FRAs are more robust toward switched traffic is, in fact, a general trend [116] and the main reason is the relatively low level of saturation of the FRA under normal operation. The deeply saturated gain

of the EDFA under normal operating conditions, on the other hand, means that its steady-state output power is mainly determined by the EDFA pump power and is more or less independent of the input power.

In the following, we focus entirely on EDFA-generated transients and a newly developed method for equalizing these.

5.3. Transient equalization using SPM in HNLF

As discussed in the previous sections, inter-channel crosstalk in saturated amplifiers lead to output power transients, which impair the signal quality and receiver sensitivity. Although automatic gain control is used in state-of-the-art EDFAs, it is unable to fully suppress the transients on a channel basis and also has problems when it comes to suppressing transients in links with varying span numbers, e.g. in reconfigurable networks. Combined with the fact that major industry players like AT&T, Nokia-Siemens and Alcatel-Lucent have recently taken great interest in this field [105,117,118], these findings strongly suggest that transients remain an unsolved issue in today's newly-deployed systems.

The sensitivity penalties induced by transient crosstalk are expected to be particularly significant in high bit rate systems of 40 Gbit/s and beyond, where the system OSNR margins are smaller and uncontrolled power bursts lead to a larger number of erroneously detected bits. Based on these observations, it is evident that there is a need for a robust and simple method to mitigate the influence of transients, on an individual channel basis, in high-speed WDM systems.

5.3.1. Previously demonstrated methods

The traditional way to regenerate a distorted optical signal is to detect and convert it to an electrical signal using an optical receiver, perform the signal regeneration electronically and subsequently retransmit the signal in the optical domain. The drawbacks of this technique (O-E-O conversion) are the large number of components involved, the size, the power consumption and the price of the components, all of which can be expected to increase with the bit rate and number of channels involved. Furthermore, real-time regeneration at 40 Gbit/s is expected to be a major technological challenge [119], even with the high-speed electronics available today.

As alternatives to electronic signal processing using O-E-O conversion, a few all-optical techniques have been proposed for equalizing transients. One method uses a multiple- and forward-pumped discrete FRA to compensate gain slope and residual EDFA transients by fast control of the pump powers [117]. This method does not work on a channel basis, however, but can

be used for fast adjustment of the Raman gain across a large bandwidth. Another promising technique uses a silicon-on-insulator-based device which continuously monitors the channel input power and then feeds a control signal to a high-speed variable optical attenuator (VOA) [120]. By combining several of these devices with an arrayed waveguide grating (AWG), equalization of EDFA transients on four 10 Gbit/s channels has been successfully demonstrated. The speed of the device is limited to 20 MHz, while the insertion and polarization dependent loss of the device have not been provided.

By utilizing the nonlinear gain properties of a semiconductor optical amplifier (SOA), T. Gibbon et al. from DTU Fotonik have successfully used a reflective SOA to equalize transients on a single 10 Gbit/s non-return-to-zero (NRZ) channel and thereby reduced the transient-induced sensitivity penalty from 2.3 dB to 1.7 dB [121]. The device performance was significantly improved by using a strong holding beam to clamp the gain and increase the stimulated emission rate in the device. This resulted in a reduction of the penalty to merely 0.2 dB. Although this improvement is not fully understood at this time, the technique seems promising, in particular, due to the low power required to saturate the gain. In the experiment, an optimum input power of -14 dBm was found to provide the best equalization results. The experiment, however, also showed clear signs of patterning and a BER dependence on the word length used. Although these effects were significantly reduced by the holding beam, it remains to be seen if this scheme is fast enough for 40 Gbit/s operation.

In the following, a novel and ultra-fast optical device is proposed for equalizing power transients on a channel basis.

5.3.2. Component principle

Fig. 5.4 shows the principle of the proposed transient equalizer. Essentially, the component consists of a piece of highly nonlinear fiber (HNLF) followed by a bandpass filter (BPF). The bandwidth of the filter should be similar to the bandwidth of the impaired signal and the center frequency of the filter ν_{BPF} should be equal to the center frequency of the impaired signal ν_s, i.e.

$$\nu_{BPF} = \nu_s \tag{5.1}$$

This condition is an essential part of the idea, as will be discussed in the following.

To understand the device principle, one can imagine a single signal pulse entering HNLF. If the pulse power into the HNLF is sufficiently high, the pulse spectrum will broaden due to Kerr-induced self-phase modulation

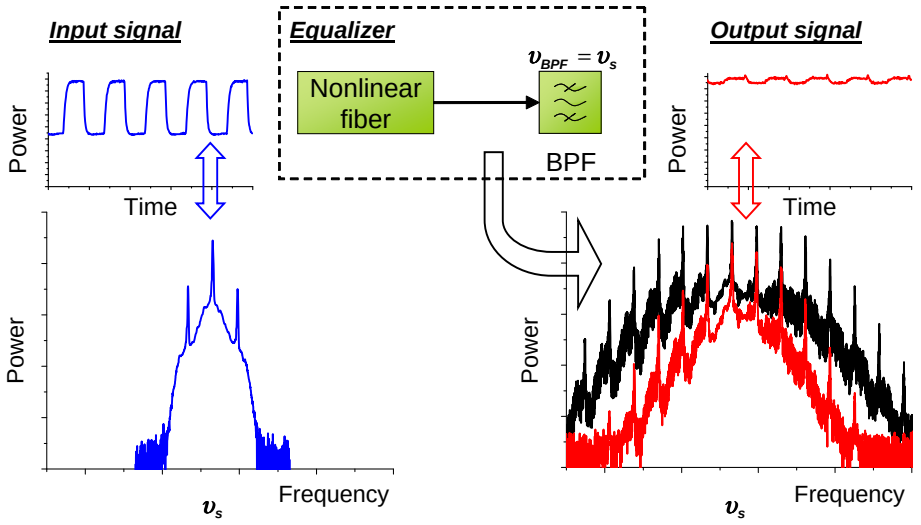

Figure 5.4.: Principle of the HNLF-based transient equalizer.

(SPM) in the fiber [20]. As the pulse passes through the filter, its spectrum is shaped by the filter and the high-frequency components of the pulse will be cut away. In this way, high power pulses will experience a large output power reduction due to filtering, while low-power pulses will pass through the filter practically unaltered.

The principle of operation is similar to the optical regenerator proposed by Mamyshev in [122]. One important difference is, however, that the output filter here is not detuned with respect to the input carrier frequency. This *on-carrier* filtering is found to work well for transient-impaired signals, where almost all of the intensity noise is located in the 1-bits. Furthermore, we have found that this method dramatically relaxes the input power requirements of the device and at the same time avoids unwanted wavelength conversion compared with off-carrier filtering. Because the device principle relies on the shift in instantaneous frequency across each pulse, the device will not work for full width pulse formats, such as NRZ. Instead, the device is effective for equalizing uneven pulse amplitudes for RZ-based formats. Compared to NRZ, RZ formats generally have better non-linear tolerance and are typically preferred in high bit rate systems ($>$ 10 Gbit/s) [123]. Due to the fundamental nature of SPM and the near-instantaneous Kerr-effect, the device is practically polarization independent and works at very high data rates. As such, SPM has, for instance, been used for all-optical wavelength conversion at a symbol rate of 160 Gbaud [124].

By changing the bandwidth of the output filter, the device can be optimized for different modulation formats and bit rates. In general, the filter

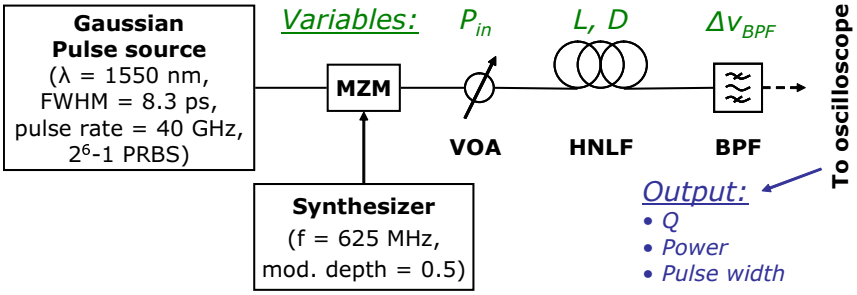

Figure 5.5.: Setup used in transient equalizer simulations.

bandwidth should be similar to the spectral width of the input signal, but this is discussed in more detail, in the following section. Aside from the filter bandwidth $\Delta\nu_{BPF}$ and transfer function, the most important optimization parameters of the device are the nonlinear coefficient γ, the length L and the dispersion coefficient D of the HNLF. The optimization of these parameters, based on a numerical model, is the topic of the following section.

5.4. Transient equalizer design

To optimize the parameters of the fiber-based transient equalizer, a numerical model was implemented using a commercial simulation tool from VPIphotonics [125]. In the following, the model setup is described followed by an explanation of how the optimized parameters are found.

5.4.1. Model description

The basic setup of the simulation model is shown in Fig. 5.5. The setup features a transmitter part, which consists of a pulse source that emits Gaussian pulses at a pulse repetition rate of 40 GHz. The pulse train is encoded with a $2^6 - 1$ length pseudo-random bit sequence (PRBS). The signal is centered at 1550 nm and the pulses have a full width at half maximum (FWHM) of 8.3 ps, corresponding to 33% of the bit slot. The sampling rate is 128 samples per bit. To boost the signal and add some intensity noise, the signal is amplified using an amplifier with a 10 dB noise figure, which is positioned after the pulse source (not in the figure).

To emulate impairments from transient crosstalk, the signal is modulated in a Mach-Zehnder modulator (MZM) with a slowly varying sinusoidal modulation frequency of 625 MHz and a modulation index of $h = 0.33$, corresponding to a 50% power variation.[1] The effect is a broadened 1-bit power

[1]The modulation index h is defined as $h = P_{amp}/P_{av}$, where P_{amp} is the power amplitude

level in the eye diagram of the equalizer input signal, as shown in Fig. 5.6 (a). Using the internal statistical functions of the software, the maximum eye-opening of the signal can be evaluated by calculating the Q parameter of the eye, defined as

$$Q = \frac{\overline{P}_1 - \overline{P}_0}{\sigma_1 + \sigma_0} \tag{5.2}$$

where $\overline{P}_1$ and $\overline{P}_0$ are the average powers and σ_1 and σ_0 are the standard deviations of the signal power, in the 2% central part of the bit slot and in the 1 and 0 bit, respectively. By assuming that the 1 and 0 bit noise has a Gaussian distribution, a Q value of 6 can be shown to correspond approximately to a BER of 10^{-9} [71]. The Gaussian approximation does not hold for transient noise, however, meaning that this relation between Q and BER does not hold in this case. For the input signal shown in Fig. 5.6 (a), Q is evaluated to 4.5.

The average signal power into the HNLF, P_{in}, is adjusted using a VOA and set in a range from 6.6 dBm to 24.6 dBm. The HNLF parameters are the same as the ones in table 2.1 on page 12. Furthermore, a fiber nonlinear index of $n_2 = 3.3 \cdot 10^{-20}$ m^2/W is used [29]. In the simulations, the dispersion coefficient D is varied between -5 ps/nm/km and 3 ps/nm/km and the fiber length L is varied between 600 m and 3000 m. The fiber model is a uni-directional split-step model [20], which takes into account fiber dispersion and slope, as well as Kerr fiber nonlinearities. ASE is included as sampled noise bins which provide the noise spectral density in a single signal polarization. Following the fiber is the output bandpass filter, which is set to be 1st order Gaussian shaped. The filter FWHM is set to a default value of $\Delta\nu_{BPF} = 100$ GHz, or 2.5 times the bit rate.

5.4.2. Design parameters

By using the model described in the previous section, we can evaluate the output Q and pulse width for a number of different fiber and filter parameters and input powers. By doing so, we want to identify a set of optimum fiber and filter parameters for a practical transient equalizer device to be used in a 40 Gbit/s system.

Fig. 5.6 (b)–(g) show calculated eye diagrams at the output of the equalizer for three different average input powers and fiber dispersion coefficient values of $D = -1$ ps/nm/km and $D = +1$ ps/nm/km, at the signal wavelength. The length of the fiber is 1800 m and the filter bandwidth is $\Delta\nu_{BPF} = 100$ GHz. The calculated Q parameters for each eye is shown in the figure captions. For a dispersion value of $D = -1$ ps/nm/km, the Q

and P_{av} is the average power of the modulated signal.

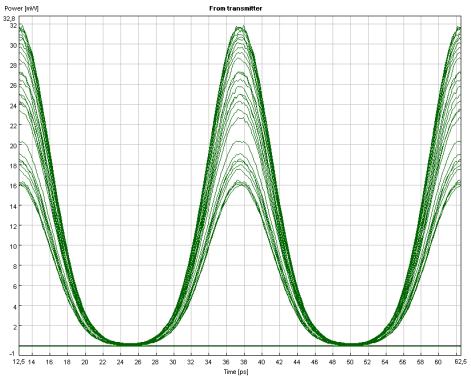

(a) Input, $Q = 4.5$

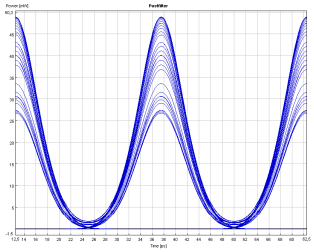

(b) $P_{in} = 11.6$ dBm, $D = -1$ ps/nm/km, $Q = 5.1$

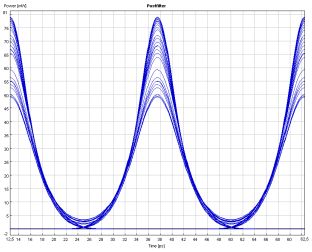

(c) $P_{in} = 14.6$ dBm, $D = -1$ ps/nm/km, $Q = 6.4$

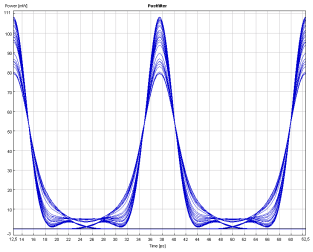

(d) $P_{in} = 17.6$ dBm, $D = -1$ ps/nm/km, $Q = 9.7$

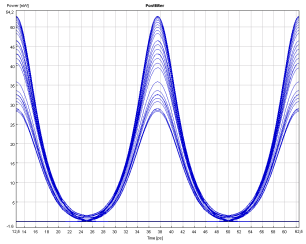

(e) $P_{in} = 11.6$ dBm, $D = 1$ ps/nm/km, $Q = 5.0$

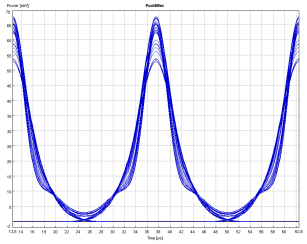

(f) $P_{in} = 14.6$ dBm, $D = 1$ ps/nm/km, $Q = 13.5$

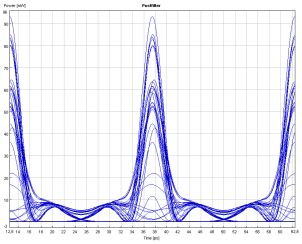

(g) $P_{in} = 17.6$ dBm, $D = 1$ ps/nm/km, $Q = 1.6$

Figure 5.6.: Calculated 40 Gbit/s eye diagrams and Q values at the (a) input and (b)–(g) output of the equalizer. The average input powers are 11.6 dBm, 14.6 dBm and 17.6 dBm, the fiber length is $L = 1800$ m, the dispersion is $D = -1$ ps/nm/km and $D = +1$ ps/nm/km and the filter bandwidth is $\Delta\nu_{BPF} = 100$ GHz. The horizontal span in the figures is 50 ps.

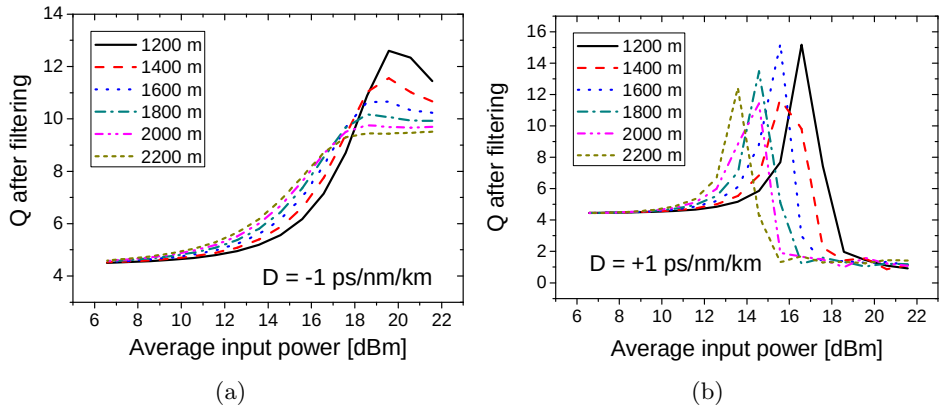

Figure 5.7.: Calculated Q parameters after filtering vs. average input power, when a HNLF with (a) negative and (b) positive dispersion is used. Fiber lengths are varied between 1200 m and 2200 m and the filter FWHM is $\Delta\nu_{BPF} = 100$ GHz.

parameter is gradually improved up to 9.7, as the input power is increased to 17.6 dBm. The power variation in the 1-bit level of the eye is clearly reduced and at the same time, the output pulse width is seen to be somewhat compressed. In the case of $D = +1$ ps/nm/km, the maximum improvement of the Q parameter is higher compared with the negative dispersion case. However, as the power is increased beyond the optimum power of 14.6 dBm, the high power pulses collapse as a result of the interplay between the SPM and positive dispersion in the fiber. The result is an immediate closing of the eye, which is quantified by a large degradation of Q from 13.5 to 1.6.

These output Q values should be compared with the input Q value of 4.5 and shows that both significant Q improvement and degradation can be obtained with this device, depending on the choice of input power and fiber dispersion.

In Fig. 5.7 (a) and (b), calculated Q parameters are plotted vs. input power for different fiber lengths and for fiber dispersion values of $D = -1$ ps/nm/km and $D = +1$ ps/nm/km, respectively. The HNLF length ranges from 1200 m to 2200 m. In general, we found very different behavior of Q vs. input power, depending on the sign of the dispersion coefficient D. The following qualitative conclusions, for these specific values of Q, has therefore been found to also hold for the other values of D, of the same sign, and in the investigated range.

For $D = -1$ ps/nm/km, Q is seen to rise steadily with power up to a maximum point and then flatten out at high input powers. For $D = +1$ ps/nm/km, the evolution of Q is much more abrupt and results in high

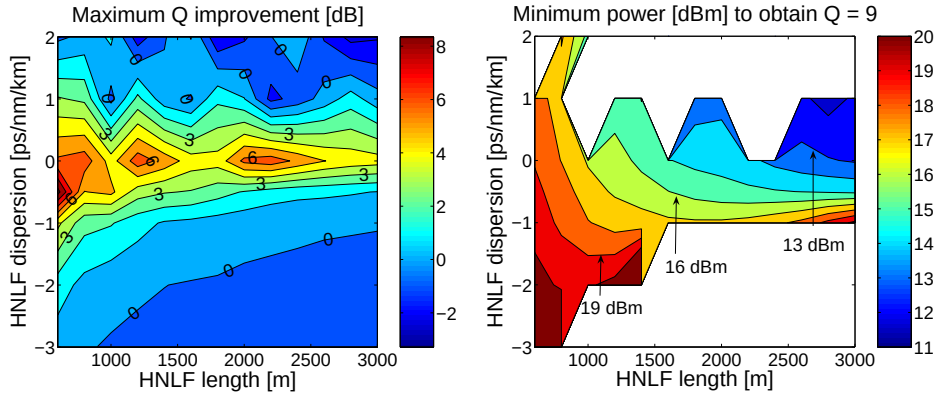

(a) (b)

Figure 5.8.: Calculated: (a) Maximum Q improvement, relative to input Q of 4.5, with a maximum input power is 24.6 dBm. (b) Minimum power needed to obtain $Q = 9.0$, or 3 dB Q improvement. Filter width is $\Delta\nu_{BPF} =$ 100 GHz.

maximum peak value, for a specific optimum input power. When the power is increased beyond this input power, Q drops very suddenly to a level which is much lower than the input value. This unstable and highly power dependent behavior of the pulse is attributed to modulation instability in the anormalous ($D > 0$) dispersion fiber [126]. From an application perspective, it is clear that the dynamic range of the device is very limited, when anormalous dispersion fibers are used. Indeed, the dynamic range of a component is a crucial parameter, if the component is to be used in a deployed system. For this reason, we require that the fiber dispersion must be normal, $D < 0$, in a practical implementation of the transient equalizer.

In Fig. 5.8 (a), the maximum improvement of the Q parameter, in the investigated input power range, is plotted in a contour plot as a function of the HNLF length L and the dispersion coefficient D. The Q improvement is relative to the input Q of 4.5 and is expressed in dB. The 0 dB, 3 dB and 6 dB contours are marked with a number for easy identification. Note, that the figure only indicates the maximum obtainable Q value, but does not say anything about the dynamic range of the device, for a specific set of fiber parameters. It is clear from the figure that the greatest improvement is obtained close to the zero-dispersion line, $D = 0$, and that the dispersion range in which a 3 dB improvement can be obtained becomes smaller with increasing fiber length.

Fig. 5.8 (b) shows the power required to obtain $Q = 9$, corresponding to a 3 dB improvement compared to Q at the input of the device. The blank

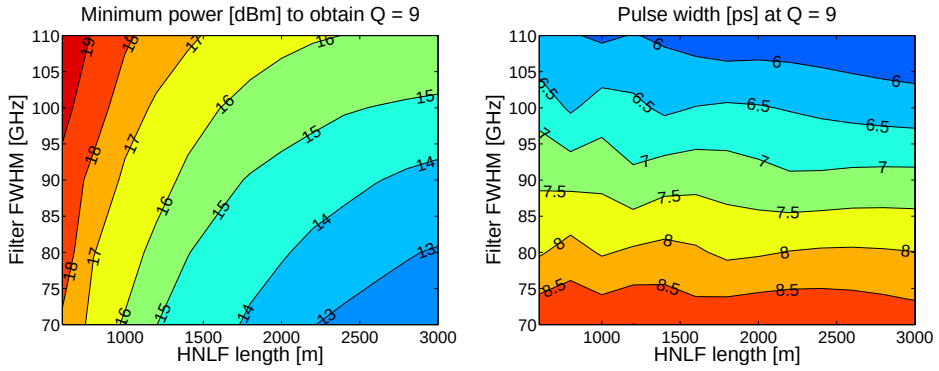

(a) (b)

Figure 5.9.: Calculated: (a) Minimum power needed to obtain $Q = 9.0$, or 3 dB improvement. (b) Output pulse width vs. filter width and HNLF length. HNLF dispersion is $D = -0.5$ ps/nm/km.

areas correspond to specific values of fiber length and dispersion, where $Q = 9$ can not be obtained in the considered input power range. The straight-line borders between the blank and colored areas should be regarded as approximate borders and are a result of the interpolation between the finite number of dispersion and length values used in the calculations. Generally, the required input power is observed to decrease with increasing fiber length and dispersion. However, if the dispersion is assumed to be limited to negative values, to maintain a high dynamic range in the device, an optimum length of around $L = 1800$ m can be observed to result in the lowest required input power. At this length, the dispersion is required to be in the narrow range $-1 \leq D < 0$.

In Fig. 5.9 (a) and (b), the dependence of the output filter bandwidth, on the required input power and output pulse width, is investigated. The dispersion coefficient here is fixed at $D = -0.5$ ps/nm/km. In sub-figure (a), the minimum power required to obtain $Q = 9$ is seen to decrease, as the fiber gets longer and the filter becomes more narrow. The reason is that the interaction length, which determines the amount of spectral broadening, increases with fiber length and that the required pulse broadening is smaller for more narrow filters. As such, the calculations predict that it should be possible to obtain $Q = 9$ with 13 dBm of channel input power and a filter width of $\Delta\nu_{BPF} = 80$ GHz. As will be shown in section 5.5, this input power value is quite close to what we found to be the optimum input power in an experimental demonstration of this device.

Fig. 5.9 (b) shows the calculated average output pulse FWHM as a function of the filter width and fiber length. In general, we would like the output

pulse to be altered as little as possible, upon passage through the device. This also means that the output pulse width should be similar to the input pulse width, which in this case is 8.3 ps. From the figure, the pulse width is seen to depend almost exclusively on the filter bandwidth, through the inverse Fourier transform relationship between the pulse width in time and frequency domain. Very little dependence on the fiber length is found. A nice observation here is that the amount of pulse compression, to a large extent, can be controlled through the filter bandwidth. In this case, the pulse width is seen to be preserved for relatively narrow filter bandwidths, between 75 ps and 80 ps, for which the required power was also found to be low.

To summarize, we found that to obtain the most power-efficient device and at the same time a large dynamic range, a HNLF with normal dispersion, preferably between -1 ps/nm/km and 0 ps/nm/km, should be used. For input pulse widths used for 40 Gbit/s 33% RZ signals, a HNLF length of $L = 1800$ m was found to work well with a minimum of required power equal to 13 dBm. Finally, a Gaussian-shaped output filter tuned to the center wavelength of the channel and having a FWHM of ~ 80 GHz should provide pulses with very little, or no pulse compression.

5.5. Equalization of 4×40 Gbit/s transient-impaired channels

In this section, an experimental demonstration of the transient equalizer is described, where four transient-impaired 40 Gbit/s 33% RZ-OOK channels are simultaneously equalized [127].

Based on the optimized fiber parameters, found in section 5.4, seven spools of HNLF have been produced and pigtailed at the production facility of OFS Fitel Denmark ApS. From the previously mentioned nonlinear index of $n_2 = 3.3 \cdot 10^{-20}$ m^2/W, an effective mode area of $A_{eff} = 12$ μm^2 (from table 2.1) and a signal wavelength of 1550 nm, the nonlinear coefficient of these fibers can be evaluated to $\gamma \approx 11$ W^{-1}km^{-1}, using the expression in [20]. The target spool length and dispersion coefficient for the experiment is $L = 1800$ m and $D = -0.5$ ps/nm/km, respectively. In order to experiment with different lengths of fiber, additional spools with lengths of 200 m, 400 m, 800 m and 1400 m have also been produced.

Fig. 5.10 summarizes the spool values of the dispersion coefficient D and dispersion slope S, including the SSMF pigtails. All values are measured at the target signal wavelength of 1550 nm. The dispersion values range from -0.33 ps/nm/km to -0.59 ps/nm/km and the ultra-low slope values range from of 0.0050 ps/nm^2/km to 0.0060 ps/nm^2/km. These values show that

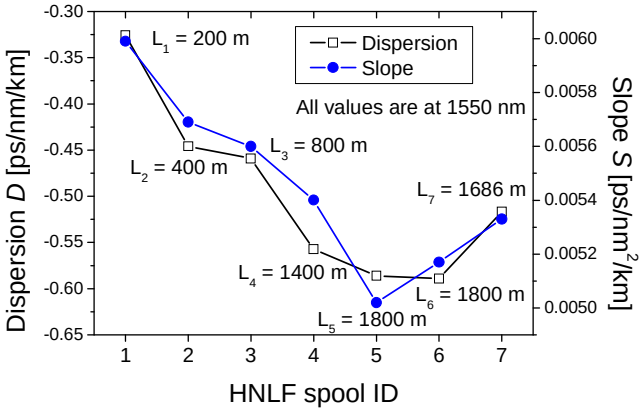

Figure 5.10.: Measured values of the dispersion coefficient D and the dispersion slope S at 1550 nm of the tailored HNLF spools. Spool combinations no. $2+4$, 5, 6 and 7 are used in the final experiment.

it is possible to produce low-dispersion spools of very short lengths (down to 200 m) with a high accuracy on D of only ± 0.2 ps/nm/km. This is clearly important for the practical realization of future devices.

5.5.1. Experimental setup

The setup used to simultaneously equalize the 4×40 Gbit/s 33% RZ-OOK channels, is shown in Fig. 5.11. Four laser sources with numbers 1, 2, 3 and 4 are positioned with 200 GHz spacing at 1552.4 nm, 1554.0 nm, 1555.6 nm and 1557.2 nm and combined in a multiplexer (MUX). The 40 Gbit/s, 33% RZ-OOK signal is encoded with a PRBS of $2^{31}-1$ using two cascaded MZMs. The first MZM is used for 33% RZ pulse carving and the other is used for the OOK modulation. After subsequent amplification, the channels are demultiplexed and combined, so that channel no. 1 and 3 are fed into an acousto-optic modulator (AOM) and on-off modulated with a repetition frequency of 2.5 kHz and with a 50% duty cycle. These switched, or disturbing, channels are hereafter referred to as Dist_1 and Dist_2. The non-switched, or surviving, channels are consequently referred to as Surv_1 and Surv_2. All four channels are recombined in a demultiplexer (DEMUX) and from there fed into a current/power-controlled EDFA. The channel input powers are adjusted so the peak power into the amplifier is the same for all channels. In the EDFA (indicated by a dark red color in the figure), inter-channel transient crosstalk is generated as a result of the time-varying input power from the switched channels, as discussed in section 5.1.

In this WDM demonstration, the filter part of the transient equalizer consists of two Gaussian-shaped AWGs with a specified filter FWHM of

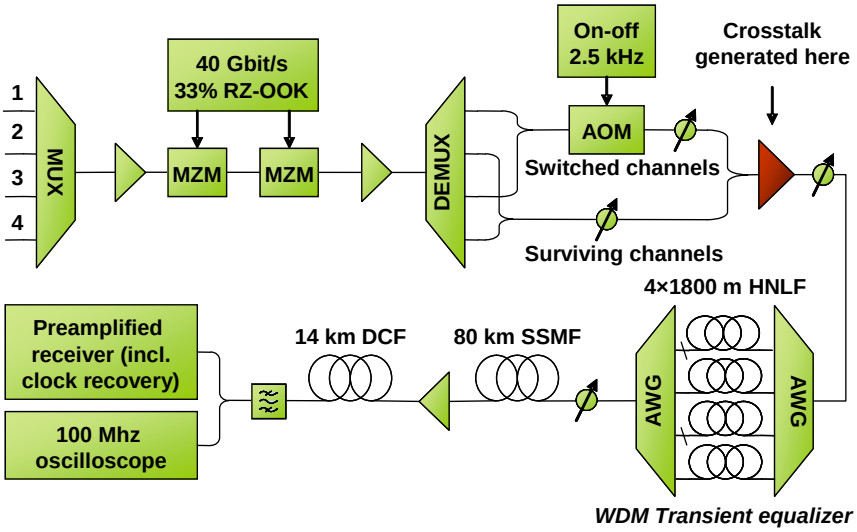

Figure 5.11.: Experimental setup used for simultaneous equalization of four transient-impaired 40 Gbit/s, 33% RZ-OOK channels.

approximately 90 GHz. The channel ports of the two AWGs are interconnected with roughly 1800 m of HNLF, consisting of spool sets $2 + 4$, 5, 6 and 7 from Fig. 5.10. The exact spool lengths are shown in the figure. In this device design, the output AWG both serves as equalizing filter for each channel, as well as a channel multiplexer. The input power into the equalizer HNLF is controlled using a VOAs in front of the equalizer. As the pre-equalizer attenuation is changed, the peak input power per channel is measured at the channel output port of the first AWG. Consequently, this power equals the power actually entering the HNLF pigtail and is hereafter referred to as the HNLF input power, or simply the HNLF power.

After equalization, the surviving channels are transmitted through 80 km of SSMF and then re-amplified using an inline power-controlled EDFA. This is done by disconnecting the disturbing channels at the output AWG, as indicated in the setup. The channels are then fed into 14 km of DCF, to compensate the chromatic dispersion of the SSMF span. The channel power into the SSMF and DCF is set to 5 dBm/ch and 0 dBm/ch, respectively. The detected channel is demultiplexed using a tunable BPF positioned in front of the preamplified receiver. Clock recovery is used to stabilize the receiver clock. The BER is measured as a function of the received power and OSNR and the respective sensitivities at a BER of 10^{-9} are evaluated. The transient waveforms are measured using a 100 MHz oscilloscope connected to a low-bandwidth photodiode.

Fig. 5.12 (a) shows the spectrum measured at the output of the transient-

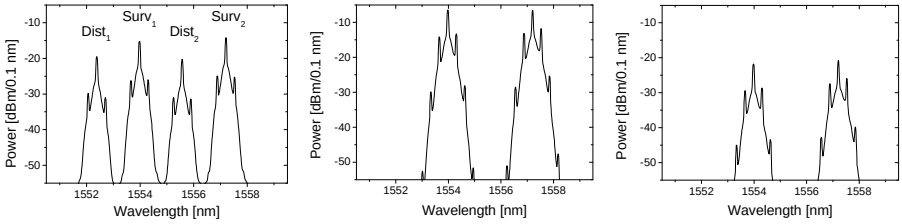

(a) Pre-equalizer (b) Post-equalizer, 0 km (c) Post-equalizer, 80 km

Figure 5.12.: (a) WDM spectrum measured before equalization. (b) and (c): Channel spectra of Surv_1 and Surv_2 measured after equalization and before and after 80 km transmission, respectively.

generating EDFA. The powers of the disturbing channels are ∼4 dB lower than the data channels and this is mainly due to the on-off modulation of the disturbing channels. Fig. 5.12 (b) and (c) show the spectra of the two surviving channels before and after 80 km transmission, respectively. The channels have been equalized prior to transmission using 13 dBm of HNLF input power. The equalization causes some broadening of the channel spectra, which is also seen by observing the more pronounced higher-order clock tones after equalization. Note that this broadening is determined by the output AWG filter width and thus can be controlled by using a different filter. At an average HNLF input power of 13 dBm/ch, the average output power from the equalizer was measured to 7.1 dBm and 7.3 dBm for Surv_1 and Surv_2, respectively. This indicates a combined loss of ~ 6 dB from fiber input to filter output, in this specific implementation.

5.5.2. Results and discussion

Fig. 5.13 (a) shows power transients of the two center channels Surv_1 and Dist_2, measured right before and after the crosstalk-generating EDFA. For clarity reasons, the two other channels are not shown, but they behave almost identically to their sibling channels. The switching frequency of the AOM is seen to be sufficiently low to allow the gain of the EDFA to reach steady state within half a modulation period. At the EDFA output, crosstalk from switched channels has been transferred to Surv_1, which now suffers from a 2.8 dB power variation. Also, significant overshoots of 1.9 dB are now apparent in the output power of Dist_2.

Fig. 5.13 (b) shows the equalizer output power of the same channels for three different levels of average channel power into the HNLF. At 15.1 dBm of HNLF power, the fluctuations of Surv_1 are reduced to 0.3 dB, while the overshoots of Dist_2 are seen to have been almost entirely removed around

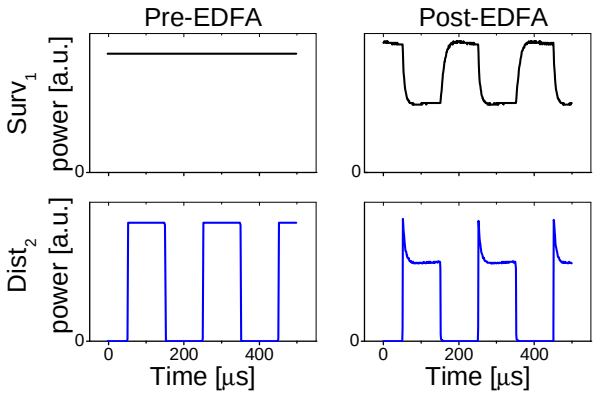

(a) Pre-equalizer

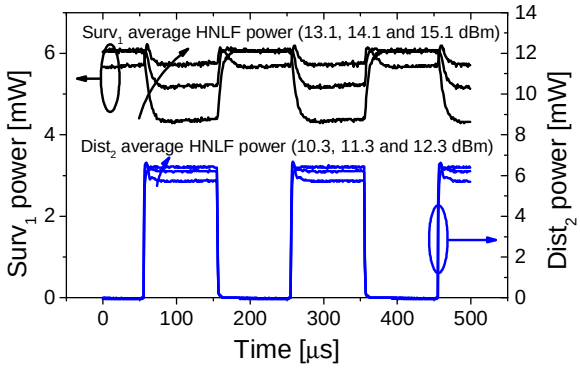

(b) Post-equalizer

Figure 5.13.: (a) and (b) Transient waveforms of neighboring channels $Surv_1$ and $Dist_2$, measured before and after equalization, respectively.

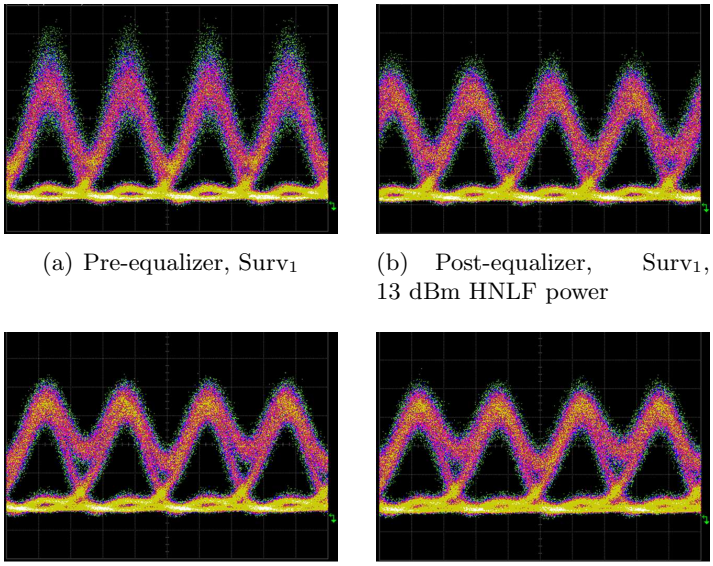

(a) Pre-equalizer, $Surv_1$

(b) Post-equalizer, $Surv_1$, 13 dBm HNLF power

(c) Post-equalizer, $Surv_2$, 0 km, 13 dBm HNLF power

(d) Post-equalizer, $Surv_2$, 80 km, 13 dBm HNLF power

Figure 5.14.: (a) and (b): Eye diagrams of $Surv_1$ before and after equalization with 13 dBm of HNLF input power.
(c) and (d): Eye diagrams of $Surv_2$ before and after 80 km transmission, respectively. The channel was equalized using 13 dBm of HNLF input power prior to transmission.

12 dBm of average input power. The equalizer is clearly capable of removing both types of transients.

Measured eye diagrams of $Surv_1$ and $Surv_2$ are shown in Fig. 5.14 (a)-(d). Fig. 5.14 (a) and (b) shows eye diagrams of $Surv_1$ measured before and after the equalizer with 13 dBm of HNLF input power. The fluctuations in the 1-bit have clearly been reduced. However, as the HNLF input power was further increased, the 0-bit noise became more dominant and no visible improvement of the eye was found. Fig. 5.14 (c) and (d) show eye diagrams of $Surv_2$, measured before and after 80 km transmission, respectively. The channel transients were equalized with 13 dBm of HNLF input power prior to transmission. The eye diagrams are very similar and very little added noise from transmission and amplification can be detected.

Measured BER of $Surv_1$ and $Surv_2$ are shown in Fig. 5.15 as a function of received OSNR and in different cases. In general, the two channels are seen to perform very similarly. Prior to equalization, the transient-impaired channels perform poorly and the OSNR sensitivity of both channels is close to 28 dB, as indicated by the blue lines in the inset. These values should be

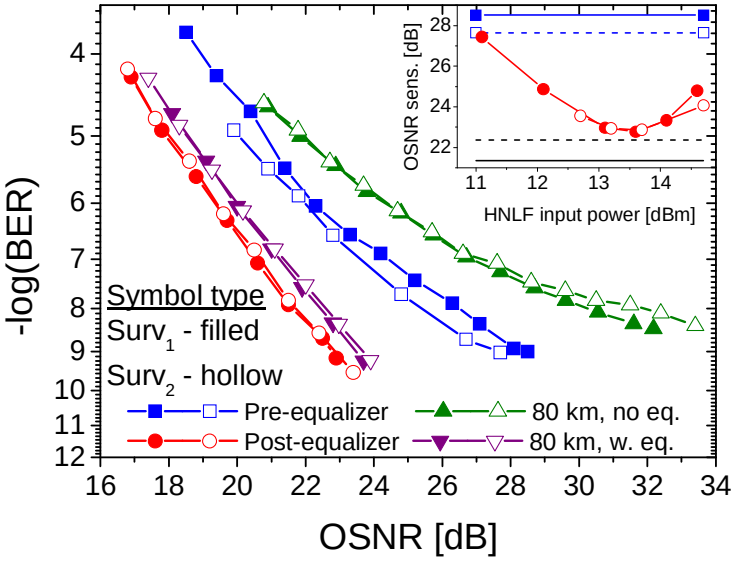

Figure 5.15.: Measured bit-error rate of $Surv_1$ and $Surv_2$ vs. OSNR. The curves are measured before and after the equalizer with optimum input power, as well as after 80 km transmission with and without prior equalization using 13 dBm HNLF power.
Inset shows the OSNR sensitivity of both channels and the solid and dashed black lines indicate the back-to-back sensitivity of $Surv_1$ and $Surv_2$, respectively.

compared with the back-to-back OSNR sensitivities of 21.4 dB and 22.4 dB (indicated by the black lines in the lower part of the inset), for Surv_1 and Surv_2, respectively. After equalization, the OSNR sensitivity is 22.8 dB and is thus improved by more than 5 dB for both channels.

When the two impaired channels are transmitted without prior use of the equalizer, an error floor is seen to appear in the BER measurements and error-free detection is no longer possible. However, when the equalizer is used before transmission, the transmission penalty is reduced to be less than 1 dB for both channels, which clearly shows the large advantage of equalizing the transients before transmission. The large transmission penalty is attributed to a combination of enhanced nonlinear impairments from the power variations and enhanced inter-channel crosstalk in the inline EDFA that is positioned before the DCF.

5.5.3. Device evaluation and perspectives

The above demonstration clearly shows that the principle of the transient equalizer works and that it easily can be parallelized to operate simultaneously on several channels. The experiment shows that it is efficient in equalizing power transients, as well as in improving large transient induced penalties, in this case by more than 5 dB. It was also found that transmission penalties from amplified spans are significantly reduced if the transients are equalized prior to transmission. The reasons are that nonlinear impairments are increased by the presence of transients and that uncontrolled amplifiers in the link will cause existing power excursions and crosstalk to be further enhanced.

The main advantages of the technique are its simple, stable and polarization insensitive operation principle. Furthermore, the device benefits from being ultra-fast, which means that it is not inclined to patterning and that it can be extended to operate simultaneously on an arbitrary number of channels, provided that enough power is available. We believe the device could also work for differential phase-shift-keying (DPSK) modulation, since the phase-shift induced by the device would be very similar for two neighboring pulses, but this still remains to be demonstrated.

The main drawback of the technique is the required optical channel power, which is relatively high in this demonstration (13 dBm per channel for optimum operation). It is unclear how much the required power can be lowered through device optimization, but we expect that optimizing the output filter (in particular the filter bandwidth) could lower the power requirements, possibly by several dB. Another possibility is to optimize the fiber. As an example, a recent design proposal for an extremely HNLF with flat dispersion and low loss is predicted to have a nonlinear coefficient of

$\gamma = 27\ \ \mathrm{W}^{-1}\mathrm{km}^{-1}$ [128]. Simulations also indicated that longer fibers were able to reduce the required power.

New development in high-power amplifiers can also help to make this device more attractive for use in future networks. As an example of this, a gain-flat EDFA with 30 dBm output power was recently demonstrated [129], which uses uncooled, multi-mode and potentially low-cost pump units.

5.6. Summary

Inter-channel crosstalk in saturated amplifiers can lead to burst-errors during detection and, in extreme cases, even cause damage to vital system components. Because EDFAs are typically run in heavy saturation, these amplifiers are more inclined to generate crosstalk than typical fiber-based Raman amplifiers. As an example of this, the output power variation of a surviving channel in a typical backward-pumped DCRA was calculated to 0.6 dB, when a switched and surviving channel were input with a channel power of 1.8 dBm. When the same channel powers were input to an EDFA, the output power variations of the surviving channel were measured to 3.1 dB, i.e much higher than the value found in the DCRA.

In spite of effective gain control in state-of-the-art amplifiers, transient crosstalk remains an unsolved problem and one that is expected to grow as more networks become dynamically reconfigurable, the channel loading increases and the bit rate gradually increases from 10 Gbit/s to 40 Gbit/s.

As a way to deal with existing transients in a system, an all-optical and polarization-insensitive device for equalizing transients and restoring the signal quality of transient-impaired signals has been proposed. Through numerical modeling, optimum device parameters for 40 Gbit/s 33% RZ channels were derived. Using a device based on the derived fiber and filter parameters, successful equalization of four 40 Gbit/s WDM channels was performed with an improved penalty after equalization in excess of 5 dB. The transmission penalty after 80 km transmission was greatly reduced when the impaired channels were equalized before transmission.

6. Conclusion and outlook

To meet the increasing bandwidth demands from new fiber-to-the-premises (FTTP) customers and bandwidth services, such as high-definition television and video-on-demand, new optical amplifier technologies are urgently needed, to take advantage of the large amount of unexploited bandwidth in the transmission fibers [6]. With their flexible bandwidth and good noise properties, fiber Raman amplifiers (FRAs) are expected to be a key technology in reaching this goal.

6.1. Obtained results

In this project, FRAs have been investigated with the purpose of identifying new applications and limitations for its use in future optical communication systems. The following specific results have been obtained.

6.1.1. Dynamic FRA model

To better understand the static and dynamic properties of FRAs, an accurate and efficient numerical amplifier model has been developed. The model has been validated by comparing its results with results from a reference amplifier model, Raman-OASIX, as well as with experimental data. When both static and dynamic input powers were used, the model was found to agree well with the reference data and has been able to reproduce experimentally measured output power transients with good accuracy. Throughout this thesis, the model has been used to supplement the experimental results and in some cases also used to generate new results, where experimental measurements would have been too time-consuming or complicated to conduct. As examples of the latter, the model was used to calculate the maximum available gain in backward-pumped dispersion compensating Raman amplifiers (DCRAs), to predict the maximum reach and channel capacity of Raman-based passive optical network (PON) links and to calculate the time-varying optical signal-to-noise ratio (OSNR) and multi-path interference (MPI) noise ratio, of a DCRA subjected to fluctuating input powers.

6.1.2. Dispersion compensating Raman amplifiers

Three different applications of DCRAs have been investigated. In the first application, a DCRA was used for terminal compensation of a 240 km link. In this setup, all dispersion compensation is handled by the DCRA, which is placed in the receiver terminal of the link. This method provides a simple way to upgrade low bit-rate links, e.g. from 2.5 Gbit/s to 10 Gbit/s, without performing link alterations. Also, the potentially long and lossy modules used in the terminals can make efficient use of the Raman pump light and thereby improve the efficiency of the Raman pumping. In the second application, DCRAs were used to extend the gain and dynamic range of commercially deployed inline erbium-doped fiber amplifiers (EDFAs) to provide flat gain with up to 33 dB average gain in the entire C-band. By exchanging the mid-stage dispersion compensating fiber (DCF) with a multiple-pump DCRA, the EDFA was able to provide flat gain with average values up to 33 dB and thereby extend their usage to 120 km spans. In the third application, calculations of a combined EDFA/DCRA were used to demonstrate how the bandwidth of future inline amplifiers can be increased to 60 nm, while maintaining a high output power of 22 dBm. Combined with a low noise figure of less than 4.5 dB, the hybrid EDFA/DCRA shows promising results for future inline wide-band amplifiers with bandwidths of 60 nm and beyond. However, there are issues related to the dynamic range of the amplifier which still need further investigation.

6.1.3. Raman-based passive optical networks

A new architecture for extending the reach of today's passive optical networks (PONs) by using distributed Raman amplification in the long-reach PON link has been proposed and demonstrated. The maximum reach and channel capacity of the system have been numerically modeled and it was found that more than 100 km reach can be obtained by using bidirectional, or upstream (US) pumping. The potential long reach of the Raman PON architecture was experimentally demonstrated with a 120 km bidirectionally pumped link, where symmetric 10 Gbit/s traffic was used. With this link, high channel output powers close to 1 dBm and low transmission penalties of less than 0.8 dB were obtained.

The dynamic performance of an 80 km bidirectional Raman PON link has been experimentally tested with 10 Gbit/s burst-mode traffic. The highly linear gain properties of the link was found to make it robust towards dynamic adding and dropping of neighboring channels. As such, the disturbance penalty on a surviving channel was found to be less than 1.0 dB, in a worst-case scenario, where a co-propagating disturbing power, corre-

sponding to 8 channels, was periodically on-off modulated. Based on these findings, it was concluded that the proposed Raman-based PON link is a serious candidate for future, high-capacity links in PONs with burst-mode traffic.

6.1.4. Inter-channel crosstalk and equalization

Inter-channel crosstalk in saturated fiber amplifiers can generate output power transients on a micro-second timescale, which can lead to burst-errors during detection and cause potential damage to vital system components. Because EDFAs are typically operated in heavy saturation, these amplifiers are more inclined to generate crosstalk and transients, than typical fiber Raman amplifiers.

Transient crosstalk remains a big challenge in newly deployed networks, as the automatic gain control used in state-of-the-art optical amplifiers is unable to control the gain on an individual channel level. The problems related to transient crosstalk is one that is expected to grow as more networks become dynamically reconfigurable and as the bit rate gradually increases from 10 Gbit/s to 40 Gbit/s. Phase-shift-keying (PSK) formats are expected to perform better than amplitude-shift-keying (ASK) formats in connection with transient crosstalk, as the decision threshold of PSK signals only depends slightly on the received power.

As a way to mitigate transient impairments on an individual channel-basis, an all-optical and polarization-insensitive device for equalizing transients and restoring the signal quality of transient-impaired signals, has been proposed. Through numerical modeling, the optimum device parameters for 40 Gbit/s 33% return-to-zero (RZ) channels were derived and it was shown that by choosing the fiber length and filter bandwidth carefully, it is possible to avoid unwanted pulse compression with this device. Using a device based on the derived fiber and filter parameters, successful equalization of four 40 Gbit/s wavelength division multiplexed (WDM) channels was performed, which resulted in an improved penalty after equalization in excess of 5 dB. The transmission penalty after 80 km transmission was greatly reduced, when the impaired channels were equalized before transmission. We expect that the optimum operation input power of 13 dBm, found in the experiment, can be reduced by a few dB through further optimization of the fiber and output filter bandwidth.

6.2. The future of FRAs in optical communications

In the near future, we expect Raman amplification to find use in long-haul systems using high bit rates of 40 Gbit/s or more, where OSNR margins are

small and distributed Raman amplification (DRA) can be effectively used to improve this margin and the reach of the system [28]. In 2–5 years, Raman amplification could also start to find use in metro and access networks, such as the long-reach PONs, described in chapter 4. A main motivation for using Raman amplification in these networks, besides the possibility of a large bandwidth, is the high saturation input power of the FRA and its resulting robustness toward fluctuating and discontinuous traffic. This type of traffic is expected to increase in amount, as networks become more reconfigurable, and it is therefore likely that problems arising from inter-channel crosstalk will also increase.

The main challenges of Raman amplification in the coming years will continue to be the low power efficiency of the amplifier, the high cost of the pumps and issues related to safety and risks of having high optical powers in the field. The latter could be a major problem in access and FTTPs networks, where optical fibers are located in much more accessible areas (cable masts and interior boxes in houses) and human interaction with the fiber is more likely. Security and monitoring of these systems will be essential for a more widespread use of the FRA in the coming years.

Bibliography

[1] N. Bergano. "Next generation undersea lightwave systems", in *IEEE International Conference on Communications, World Prosperity Through Communications,* pp. 1525–1530 vol.3, 1989.

[2] AT&T. "Milestones in AT&T History". `http://www.corp.att.com/history/milestones.html`, 2008.

[3] Wikipedia. "TAT-8 — Wikipedia, The Free Encyclopedia". `http://en.wikipedia.org/w/index.php?title=TAT-8&oldid=204285396`, 2008.

[4] TeleGeography. "Trans-Pacific Express deal signed for US-China cable". `http://www.telegeography.com/cu/article.php?article_id=15965`, Dec 2006.

[5] E. Mutafungwa. "S-72.3340 Optical Networks Course Lecture 10: Deployment Considerations". `http://www.comlab.hut.fi/studies/3340/Lecture%2010_Deployment%20Considerations.pdf`, Apr 2007.

[6] E. B. Desurvire. "Capacity Demand and Technology Challenges for Lightwave Systems in the Next Two Decades", *Journal of Lightwave Technology*, vol. 24, no. 12, pp. 4697–4710, Dec. 2006.

[7] A. K. Srivastava and Y. Sun. *Optical Fiber Telecommunications IVA*, Chapter 4. Advances in Erbium-Doped Fiber Amplifiers, pp. 174–212, Academic Press, 2002.

[8] P. Bayvel and R. Killey. *Optical Fiber Telecommunications IVB - Systems and Impairments*, Chapter 13. Nonlinear Optical Effects in WDM Transmission, pp. 611–641, Academic Press, 2002.

[9] D. Menashe, A. Shlifer, and U. Ghera. "Optical Amplifiers for Modern Networks", in *International Conference on Transparent Optical Networks (ICTON) 2006,* Nottingham, UK, Paper Tu.C1.2, June 2006.

[10] H. Kidorf, K. Rottwitt, M. Nissov, M. Ma, and E. Rabarijaona. "Pump Interactions in a 100-nm Bandwidth Raman Amplifier", *IEEE Photonics Technology Letters*, vol. 11, no. 5, pp. 530–532, 1999.

[11] E. Schulze, M. Malach, and F. Raub. "All-Raman Amplified Links in Comparison to EDFA Links in Case of Switched Traffic", in *European Conference on Optical Communication (ECOC),* Paper S3.08, 2002.

[12] P. Hofmann, E. E. Basch, S. Gringeri, R. Egorov, D. A. Fishman, and W. A. Thompson. "DWDM Long Haul Network Deployment For The Verizon GNI Nationwide Network", in *Proc. of the conference on Optical Fiber Communications,* Paper OtuP5, 2005.

[13] D. Z. Chen, T. J. Xia, G. Wellbrock, P. Mamyshev, S. Penticost, G. Grosso, A. Puc, P. Perrier, and H. Fevrier. "New Field Trial Distance Record of 3040 km on Wide Reach WDM With 10 and 40 Gb/s Transmission Including OC-768 Traffic Without Regeneration", *Journal of Lightwave Technology*, vol. 25, no. 1, pp. 28–37, 2007.

[14] C. V. Raman. "A new radiation", *Indian Journal of Physics*, vol. 2, pp. 387–398, 1928.

[15] G. Landsberg and L. Mandelstam. "Scattering of light in crystals", *Zeitschrift für Physik*, vol. 50, pp. 769–780, 1928.

[16] J. Bromage. "Raman Amplification for Fiber Communications Systems", *Journal of Lightwave Technology*, vol. 22, pp. 79–93, 2004.

[17] E. Hecht. *Optics.* Addison-Wesley, Pearson Education, Inc., San Franscisco, CA, USA, Fourth edition, 2002.

[18] M. A. Farahani and T. Gogolla. "Spontaneous Raman scattering in optical fibers with modulated probe light for distributed temperature Raman remote sensing", *Journal of Lightwave Technology*, vol. 17, no. 8, pp. 1379–1391, 1999.

[19] J. W. Schopf, A. B. Kudryavtsev, D. G. Agresti, T. J. Wdowiak, and A. D. Czaja. "Laser-Raman imagery of Earth's earliest fossils", *Nature*, vol. 416, pp. 73–76, 2002.

[20] G. P. Agrawal. *Nonlinear Fiber Optics.* Optics and Photonics. Academic Press, Third edition, 2001.

[21] F. L. Galeener, J. C. Mikkelsen, R. H. Geils, and W. J. Mosby. "The relative Raman cross sections of vitreous SiO_2, GeO_2, B_2O_3, and P_2O_5", *Appl. Phys. Lett.*, vol. 32, no. 1, pp. 34–36, 1978.

[22] K. Rottwitt and A. J. Stenz. *Optical Fiber Telecommunications IV A*, Chapter Raman Amplification in Lightwave Communication Systems, pp. 213–257, Academic Press, 2002.

[23] W. P. Urquhart and P. J. Laybourn. "Effective core area for stimulated Raman scattering in single-mode optical fibres", *IEE Proceedings J (Optoelectronics)*, vol. 132, no. 4, pp. 201–204, 1985.

[24] A. Mori, H. Masuda, K. Shikano, K. Oikawa, K. Kato, and M. Shimizu. "Ultra-wideband tellurite-based Raman fibre amplifier", *Electron. Lett.*, vol. 37, pp. 1442–1443, 2001.

[25] Z. Yusoff, J. H. Lee, W. Belardi, T. M. Monro, P. C. Teh, and D. J. Richardson. "Raman effects in a highly nonlinear holey fiber: amplification and modulation", *Optics Letters*, vol. 27, no. 6, pp. 424–426, 2002.

[26] L. Grüner-Nielsen, Y. Qian, and P. B. Gaarde. "Dispersion Compensating Fibers for Raman Applications", Expected to be published in 2007. Chapter 5 of "Fiber Based Dispersion Compensation", Siddharth Ramachandran, Editor, Springer Verlag.

[27] S. Jiang, B. Bristiel, Y. Jaouën, P. Gallion, E. Pincemin, and S. Capouilliet. "Full characterization of modern transmission fibers for Raman amplified-based communication systems", *Optics Express*, vol. 15, no. 8, pp. 4883–4892, 2007.

[28] L. Nelson and B. Zhu. *Raman Amplifiers for Telecommunications 2*, Chapter 19. 40 Gb/s Raman-Amplified Transmission, pp. 673–721, Springer Series in Optical Sciences, Springer Berlin / Heidelberg, 2004.

[29] L. Grüner-Nielsen and B. Pálsdóttir. "Highly nonlinear fibers for very wideband supercontinuum generation", in *Proceedings of SPIE – Volume 6873,* p. 68731B, Feb. 2008.

[30] OFS Fitel Denmark ApS. "Internal experimental data", May 2008.

[31] S. Namiki and Y. Emori. "Ultrabroad-band Raman amplifiers pumped and gain-equalized by wavelength-division-multiplexed high-power laser diodes", *IEEE Journal of Selected Topics in Quantum Electronics*, vol. 7, no. 1, pp. 3–16, 2001.

[32] R. H. Stolen. *Raman Amplifiers for Telecommunications*, Chapter 2. Fundamentals of Raman Amplification in Fibers, pp. 35–60, Springer-Verlag, New York, Inc., 2004.

[33] C. R. S. Fludger, V. Handerek, and R. J. Mears. "Pump to Signal RIN transfer in Raman Fiber Amplifiers", *Journal of Lightwave Technology*, vol. 19, pp. 1140–1148, Feb. 2001.

[34] R.-J. Essiambre, P. Winzer, J. Bromage, and C. H. Kim. "Design of Bidirectionally Pumped Fiber Amplifiers Generating Double Rayleigh Backscattering", *IEEE Photonics Technology Letters*, vol. 14, no. 7, pp. 914–916, 2002.

[35] A. Puc, G. Grosso, P. Gavrilovic, H. Fevrier, A. Kaminski, S. Burtsev, D. Chang, M. Foster, W. Pelouch, and P. Perrier. "Ultra-wideband 10.7 Gb/s NRZ terrestrial transmission beyond 3000km using all-Raman amplifiers", in *Proceedings of the European Conference on Optical Communications (ECOC),* Glasgow, Scotland, Paper Mo3.2.5, 2005.

[36] C. Rasmussen, T. Fjelde, J. Bennike, F. Liu, S. Dey, B. Mikkelsen, P. Mamyshev, P. Serbe, P. van der Wagt, Y. Akasaka, D. Harris, D. Gapontsev, V. Ivshin, and P. Reeves-Hall. "DWDM 40G Transmission Over Trans-Pacific Distance (10 000 km) Using CSRZ-DPSK, Enhanced FEC, and All-Raman-Amplified 100-km UltraWave Fiber Spans", *Journal of Lightwave Technology*, vol. 22, no. 1, pp. 203–207, 2004.

[37] A. Kaminski et al. "All-Raman Unrepeatered Transmission over 440 km of Standard PSCF", in *Proc. of European Conference on Optical Communications (ECOC),* Glasgow, Paper Mo.4.2.7, 2005.

[38] L. Labrunie, P. Bousselet, V. Karpov, S. Papernyi, V. Protopopov, and V. Faraci. "4×10 Gbit/s WDM Unrepeatered Transmission over 525 km with Third-Order Cascaded Pumping", in *Proc. of European Conference on Optical Communications (ECOC),* Glasgow, Scotland, Paper Mo4.2.4, 2005.

[39] H. S. Seo, J. T. Ahn, W. J. Chung, and B. J. Park. "Novel Er/Raman Fibre Amplifier Covering S + C + L Bands with 100 nm Bandwidth", in *Proceedings of ECOC 2005,* Paper We4.P.135, 2005.

[40] S. Namiki, K. Seo, N. Tsukiji, and S. Shikii. "Challenges of Raman Amplification", *Proceedings of the IEEE*, vol. 94, no. 5, pp. 1024–1035, 2006.

[41] Y. Emori, S. Matsushita, and S. Namiki. "Cost-effective depolarized diode pump unit designed for C-band flat-gain Raman amplifiers to control EDFA gain profile", in *Optical Fiber Communication Conference (OFC) 2000, Vol. 4,* pp. 106–108, March 2000.

[42] S. Kado, Y. Emori, S. Namiki, N. Tsukiji, J. Yoshida, and T. Kimura. "Broadband flat-noise Raman amplifier using low-noise bidirectionally

pumping sources", in *Proc. of European Conference on Optical Communications (ECOC),* Amsterdam, The Netherlands, Paper PD.F.1.8, 2001.

[43] P. B. Hansen, L. Eskildsen, A. J. Stentz, T. A. Strasser, J. Judkins, J. J. DeMarco, R. Pedrazzani, and D. J. DiGiovanni. "Rayleigh Scattering Limitations in Distributed Raman Pre-Amplifiers", *IEEE Photonics Technology Letters*, vol. 10, no. 1, pp. 159–161, Jan. 1998.

[44] M. Nissov, K. Rottwitt, H. D. Kidorf, and M. X. Ma. "Rayleigh crosstalk in long cascades of distributed unsaturated Raman amplifiers", *Electronics Letters*, vol. 35, no. 12, pp. 997–998, 1999.

[45] D. M. Baney, P. Gallion, and R. S. Tucker. "Theory and measurement techniques for the noise figure of optical amplifiers", *Opt. Fib. Tech.*, vol. 6, pp. 122–154, 2000.

[46] R. G. Smith. "Optical Power Handling Capacity of Low Loss Optical Fibers as Determined by Stimulated Raman and Brillouin Scattering", *Applied Optics*, vol. 11, no. 11, pp. 2489–2494, 1972.

[47] P. Bayvel and P. M. Radmore. "Solutions of the SBS equations in single mode optical fibres and implications for fibre transmission systems", *Electronics Letters*, vol. 26, pp. 434–436, 1990.

[48] A. Kobyakov, M. Mehendale, M. Vasilyev, S. Tsuda, and A. F. Evans. "Stimulated Brillouin Scattering in Raman-Pumped Fibers: A Theoretical Approach", *Journal of Lightwave Technology*, vol. 20, no. 8, pp. 1635–1643, Aug. 2002.

[49] C. J. Chen and W. S. Wong. "Transient effects in Raman optical amplifiers", in *Proc. of Optical Amplifiers and their Applications (OAA),* Paper OMC2, 2001.

[50] M. L. Nielsen. *Experimental and Theoretical Investigation of Semiconductor Optical Amplifier (SOA) based All-Optical Switches.* Ph.D. thesis, Reseach Center COM, Technical University of Denmark, Kgs. Lyngby, Denmark, Apr. 2004.

[51] C. R. S. Fludger. *Raman Amplifiers for Telecommunications*, Chapter 4. Linear Noise Characteristics, pp. 91–120, Springer-Verlag, New York, Inc., 2004.

[52] Y. Chen, L. Lunardi, D. Al-Salameh, and S. Lumish. "Raman Tilt and non-ideal tilt control function of C-band Erbium-doped fiber ampli-

fiers", in *Proceedings of APOC 2002:Optical Components and Transmission Systems,* pp. 185–192, Oct. 2002.

[53] C. R. S. Fludger. *Raman Amplifiers for Telecommunications*, Chapter 8. Noise due to Fast-Gain Dynamics, pp. 213–252, Springer-Verlag, 2004.

[54] L. Grüner-Nielsen and Y. Qian. *Raman Amplifiers for Telecommunications*, Chapter 6. Dispersion-Compensating Fibers for Raman Applications, pp. 161–189, Springer-Verlag, 2004.

[55] L. Grüner-Nielsen, M. Wandel, P. Kristensen, C. Jørgensen, L. V. Jørgensen, B. Edvold, B. Pálsdóttir, and D. Jakobsen. "Dispersion-Compensating Fibers", *Journal of Lightwave Technology*, vol. 23, pp. 3566–3579, Nov. 2005.

[56] A. J. Lucero, D. G. Foursa, D. Kovsh, M. Nissov, and A. N. Pilipetskii. "Long-Haul Raman-Assisted EDFA Systems with Ultra-Long Spans", in *Proceedings of OFC 2007,* Anaheim, CA, USA, Paper JThA39, 2007.

[57] P. B. Hansen, G. Jacobovitz-Veselka, L. Grüner-Nielsen, and A. J. Stentz. "Raman amplification for loss compensation in dispersion compensating fibre modules", *Electronics Letters*, vol. 34, pp. 1136–1137, 1998.

[58] Y. Emori, Y. Akasaka, and S. Namiki. "Broadband lossless DCF using Raman amplification pumped by multichannel WDM laser diodes", *Electron. Lett.*, vol. 34, pp. 2145–2146, 1998.

[59] A. C. O. Chan and M. Premaratne. "Dispersion-Compensating Fiber Raman Amplifiers With Step, Parabolic, and Triangular Refractive Index Profiles", *Journal of Lightwave Technology*, vol. 25, no. 5, pp. 1190–1197, May 2007.

[60] Y. Qian, J. Povlsen, S. Knudsen, and L. Grüner-Nielsen. "Fiber Raman amplifications with single-mode fibers", *Trends in Optics and Photonics Series TOPS*, vol. 44, pp. 128–134, 2000.

[61] J. Jeon, H. Seo, and Y. Lee. "Wide-band High Negative Dispersion-Flattened Fiber", in *European Conference on Optical Communications (ECOC),* Paper P1.35, 2002.

[62] S. P. N. Cani et al. "Requirements for Efficient Raman Amplification and Dispersion Compensation Using Microstructured Optical Fibers", *Fiber and Integrated Optics*, vol. 26, pp. 255–270, 2007.

[63] K. Digweed-Lyytikainen et al. "Photonic crystal optical fibers for dispersion compensation and Raman amplification: Design and experiment", *Microwave and Optical Technology Letters*, vol. 49, no. 4, pp. 872–874, 2007.

[64] M. Tang, P. Shum, and Y. Gong. "Design of double-pass discrete Raman amplifier and the impairments induced by Rayleigh backscattering", *Optics Express*, vol. 11, no. 16, pp. 1887–1893, Aug. 2003.

[65] M. Tang, Y. D. Gong, and P. Shum. "Design of Double-Pass Dispersion-Compensated Raman Amplifiers for Improved Efficiency: Guidelines and Optimizations", *Journal of Lightwave Technology*, vol. 22, no. 8, pp. 1899–1908, 2004.

[66] S.-K. Liaw, L. Dou, and A. Xu. "Fiber-bragg-grating-based dispersion-compensated and gain-flattened Raman fiber amplifier", *Optics Express*, vol. 15, no. 19, pp. 12356–12361, 2007.

[67] Z. Tong, H. Wei, and S. Jian. "Optimal Design of Multistage Discrete Raman Amplifiers Incorporating Midway Isolators", *IEEE Photonics Technology Letters*, vol. 16, no. 10, pp. 2230–2232, 2004.

[68] M. O. van Deventer. "Polarization properties of Rayleigh backscattering in single-mode fibers", *Journal of Lightwave Technology*, vol. 11, pp. 1895–1899, 1993.

[69] V. Smokovdin, S. Lewis, and S. Chernikov. "Direct comparison of electrical and optical measurements of double Rayleigh scatter noise", in *European Conference on Optical Communications (ECOC),* Paper S3.5, 2002.

[70] C. H. Kim, J. Bromage, and R. M. Jopson. "Reflection-induced penalty in Raman amplified systems", *IEEE Photonics Technology Letters*, vol. 14, no. 4, pp. 573–575, 2002.

[71] G. P. Agrawal. *Fiber optic communication systems.* J. Wiley, Third edition, 2002.

[72] Y. Frignac and S. Bigo. "Numerical optimization of residual dispersion in dispersion-managed systems at 40 gbit/s", in *Proceedings of OFC 2000,* Paper TuD3-1, 2000.

[73] R. I. Killey, H. J. Thiele, V. Mikhailov, and P. Bayvel. "Reduction of intrachannel nonlinear distortion in 40-Gb/s-based WDM transmission over standard fiber", *IEEE Photonics Technology Letters*, vol. 12, no. 12, pp. 1624–1626, 2000.

[74] L. E. Nelson, C. G. Jørgensen, M. Du, T. Loadholt, and D. Peckham. "Terminal-Only Compensation of a 6 × 80 km 10-Gb/s WDM Metro Link Using Raman-Pumped Dispersion-Compensating Fiber Amplifiers", *IEEE Photonics Technology Letters*, vol. 18, pp. 139–141, 2006.

[75] R. Kjær, M. Galili, L. K. Oxenløwe, C. G. Jørgensen, and P. Jeppesen. "Raman-assisted transmission of 16×10 Gbit/s over 240 km using post-compensation only", in *Proceedings of Conference on Lasers and Electro-Optics, CLEO '06,* Long Beach, CA, USA, Paper CThP4, May 2006.

[76] H. Masuda and S. Kawai. "Wide-Band and Gain-Flattened Hybrid Fiber Amplifier Consisting of an EDFA and a Multiwavelength Pumped Raman Amplifier", *IEEE Photonics Technology Letters*, vol. 11, no. 6, pp. 647–649, 1999.

[77] B. Bakhshi, S. Papernyi, M. Manna, G. Mohs, P. Corbett, B. Shum-Tim, and E. Golovchenko. "320 Gb/s (32 x 12.3 Gb/s) 410 km Repeaterless WDM System Ready for Field Deployment", in *ECOC 2005 Proceedings - Vol. 1,* Glasgow, Paper Mo4.2.5, 2005.

[78] H. H. Lee, J. M. Oh, D. Lee, J. Han, H. S. Chung, and K. Kim. "A Variable-Gain Optical Amplifier for Metro WDM Networks With Mixed Span Losses: A Gain-Clamped Semiconductor Optical Amplifier Combined With a Raman Fiber Amplifier", *IEEE Photonics Technology Letters*, vol. 17, no. 6, pp. 1301–1303, 2005.

[79] R. Kjær, B. Palsdottir, C. G. Jørgensen, L. K. Oxenløwe, and P. Jeppesen. "Hybrid Erbium/Raman Fiber Amplifier with High Dynamic Range and Low Gain Ripple in Entire C-band", in *Proceedings of Optical Amplifiers and Their Applications, OAA '06,* Whistler, British Columbia, Canada, Paper JWB40, June 2006.

[80] I.-T. T. standardization sector of ITU. "G.692 Optical interfaces for multichannel systems with optical amplifiers". Recommendation, ITU, 10 1998.

[81] C. Chang, L. Wang, and Y. Chiang. "A dual pumped double-pass L-band EDFA with high gain and low noise", *Optics Communications*, vol. 267, pp. 108–122, 2006.

[82] Y. B. Lu, P. L. Chu, A. Alphones, and P. Shum. "A 105-nm Ultrawide-Band Gain-Flattened Amplifier Combining C- and L-Band Dual-Core EDFAs in a Parallel Configuration", *IEEE Photonic Technology Letters*, vol. 16, pp. 1640–1642, 2004.

[83] H. Masuda and S. Kawai. "Wide-band and gain-flattened hybrid fiber amplifier consisting of an EDFA and a multiwavelength pumped Raman amplifier", *IEEE Photonics Technology Letters*, vol. 11, pp. 647–649, 1999.

[84] D. Nesset et al. "10 Gbit/s Bidirectional Transmission in 1024-way Split, 110 km Reach, PON System using Commercial Transceiver Modules, Super FEC and EDC", in *ECOC 2005,* Paper Tu 1.3.1, 2005.

[85] T. Koonen. "Fibre-optic techniques for broadband access networks", *Telektronikk*, vol. 2, pp. 49–65, 2005.

[86] R. Davey et al. "DWDM Reach Extension of a GPON to 135 km", *Journal of Lightwave Technology*, vol. 24, pp. 29–31, 2006.

[87] J. A. Lázaro, J. Prat, P. Chanclou, G. M. T. Beleffi, A. Teixeira, I. Tomkos, R. Soila, and V. Koratzinos. "Scalable Extended Reach PON", in *Proc. of Optical Fiber Communication Conf. (OFC),* San Diego, CA, USA, Paper OThL2, 2008.

[88] H. H. Lee, K. C. Reichmann, P. P. Iannone, X. Zhou, and B. Pálsdóttir. "A hybrid-amplified PON with 75-nm downstream bandwidth, 60 km reach, 1:64 split and multiple video services", in *Proc. of Optical Fiber Communication Conf. (OFC),* Anaheim, CA, USA, Paper OWL2, 2007.

[89] I. T. Monroy, R. Kjær, A. M. J. Koonen, B. Palsdottir, and P. Jeppesen. "10 Gb/s bidirectional single fibre long reach PON link with distributed Raman amplification", in *Proceedings of European Conference on Optical Communication, ECOC' 06,* Cannes, France, Paper We3.P.166, September 2006.

[90] R. Kjær, I. T. Monroy, B. Palsdottir, L. K. Oxenløwe, and P. Jeppesen. "Bi-directional 120 km long-reach PON link based on distributed Raman amplification", in *Proceedings of IEEE Lasers and Electro-Optics Society Annual Meeting, LEOS' 06,* Montreal, Canada, p. WEE3, October 2006.

[91] Y. Aoki, K. Tajima, and I. Mito. "Input power limits of single-mode optical fibers due to stimulated Brillouin scattering in optical communication systems", *Journal of Lightwave Technology*, vol. 6, pp. 710–719, May 1988.

[92] R. Kjær, I. T. Monroy, L. K. Oxenløwe, P. Jeppesen, and B. Palsdottir. "Impairments due to Burst-Mode Transmission in a Raman-based Long Reach PON Link", *IEEE Photonics Technology Letters*, vol. 19, no. 19, pp. 1490–1492, Oct. 2007.

[93] S. K. Korotky, P. B. Hansen, L. Eskildsen, and J. J. Veselka. "Efficient phase modulation scheme for suppressing stimulated Brillouin scattering", in *Conf. on Integrated Optics and Optical Communications,* Hong Kong, Paper WD2-1, 1995.

[94] G. Talli and P. D. Townsend. "Feasibility Demonstration of 100km Reach DWDM SuperPON with Upstream Bit Rates of 2.5Gb/s and 10Gb/s", in *Proc. of Optical Fiber Communication Conf. (OFC),* Paper OFI1, Mar. 2005.

[95] L. G. Kazovsky. "Burst-Mode Metro and Access Networks", in *Proc. of Optical Fiber Communications Conference (OFC),* Anaheim, CA, USA, Paper OWC1, 2007.

[96] P. Lundquist, M. Levesque, J. Morrier, and D. Zaccarin. "Optical transients in cascaded EDFAs: Effects on transmission system performance", in *Optical Amplifiers and Their Applications (OAA),* pp. 70–72, 2003.

[97] M. C. Fischer, G. C. Gupta, L. L. Wang, K. Kojima, O. Mizuhara, and V. Swaminathan. "FEC Performance Under Optical Power Transient Conditions", *IEEE Photonic Technology Letters*, vol. 15, no. 11, pp. 1654–1656, Nov. 2003.

[98] N. Suzuki and J. Nakagawa. "First Demonstration of Full Burst Optical Amplified GE-PON Uplink with Extended System Budget of up to 128 ONU splits and 58 km reach", in *European Conference on Optical Communication (ECOC),* Glasgow, Scotland, Paper Tu1.3.3, Sep. 2005.

[99] H. H. Lee, J. M. Oh, D. Lee, G. W. Lee, and S. T. Hwang. "Performance of 16×10 Gb/s WDM Transmissions Over 4×40 km of SMF Using Linear Optical Amplifiers Combined With Raman-Pumped Dispersion Compensation Fibers Under Dynamic Add-Drop Situations", *IEEE Photonic Technology Letters*, vol. 16, pp. 1576–1578, June 2004.

[100] Y. Aoki and S. Kinoshita. *Transient response characteristics of Raman amplified optical add/drop multiplexing network*, In *Optical Transmission and Equipment for WDM Networking,* pp. 129–136, 2002.

[101] S.-H. Yam, C.-J. Chen, G. Kalogerakis, I. White, Y. Akasaka, A. Srivastava, Y. Sun, Y.-J. Cheng, R. Monnard, G. Wilson, M. Marchic, and L. Kazovsky. "Transient control study of erbium-doped fiber amplifiers for reconfigurable DWDM networks", in *Proc. of Conference on Lasers and Electro-Optics, 2004. (CLEO),* Paper CTuV4, 2004.

[102] Y. Sun, A. K. Srivastava, J. L. Zyskind, J. W. Sulhoff, C. Wolf, and R. W. Tkach. "Fast power transients in WDM optical networks with cascaded EDFAs", *Electronics Letters*, vol. 33, pp. 313–314, 1997.

[103] A. R. Grant and D. C. Kilper. "Signal transient propagation in an all Raman amplified system", in *Proc. of Optical Fiber Communications Conference (OFC),* Paper ThT3, 2004.

[104] Y. Sun, A. K. Srivastava, J. Zhou, and J. W. Sulhoff. "Optical fiber amplifiers for WDM optical networks", *Bell Labs Technical Journal*, vol. 4, no. 1, pp. 187–206, 1999.

[105] Nokia-Siemens. "Guest presentation at COM•DTU, Technical University of Denmark", Oct 2007.

[106] D. C. Kilper, C. A. White, and S. Chandrasekhar. "Control of Channel Power Instabilities in Constant-Gain Amplified Transparent Networks Using Scalable Mesh Scheduling", *Journal of Lightwave Technology*, vol. 26, no. 1, pp. 108–113, 2008.

[107] S. Pachnicke, M. Obholz, E. Voges, P. M. Krummrich, and E. Gottwald. "Electronic EDFA gain control for the suppression of transient gain dynamics in long-haul transmission systems", in *Proc. of Optical Fiber Communications Conference (OFC),* Anaheim, CA, USA, Paper JWA15, 2007.

[108] C.-J. Chen et al. "Control of transient effects in distributed and lumped Raman amplifiers", *Electronics Letters*, vol. 37, no. 21, pp. 1304–1305, 2001.

[109] X. Zhou, M. Feuer, and M. Birk. "A Simple Feed-Forward Control Algorithm for Fast Dynamic Gain Profile Control in a Multiwavelength Forward-Pumped Raman Fiber Amplifier", *IEEE Photonic Technology Letters*, vol. 18, pp. 1004–1006, May 2006.

[110] D. C. Kilper, A. R. Grant, T. K. Ho, T. Salamon, and C. A. White. "Wavelength-dependent channel power transient response in broadband Raman-amplified transmission", *Journal of Optical Networking*, vol. 7, pp. 132–141, 2008.

[111] E. Desurvire. "Analysis of Transient Gain Saturation and Recovery in Erbium-Doped Fiber Amplifiers", *IEEE Photonics Technology Letters*, vol. 1, no. 8, pp. 196–198, 1989.

[112] A. Bononi and L. A. Rusch. "Doped-Fiber Amplifier Dynamics: A System Perspective", *Journal of Lightwave Technology*, vol. 16, no. 5, pp. 945–956, 1998.

[113] C.-J. Chen and W. Wong. "Transient effects in saturated Raman amplifiers", *Electronics Letters*, vol. 37, no. 6, pp. 371–373, 2001.

[114] A. Bononi, M. Papararo, and M. Fuochi. "Transient gain dynamics in saturated Raman amplifiers", *Optical Fiber Technology*, vol. 10, pp. 91–123, 2004.

[115] M. Karásek and M. Menif. "Channel Addition/Removal Response in Raman Fiber Amplifiers: Modeling and Experimentation", *Journal of Lightwave Technology*, vol. 20, no. 9, pp. 1680–1687, 2002.

[116] M. N. Islam, M. Freeman, and J. Kim. "Raman Amplifier Simulations with Bursty Traffic". `http://www.eecs.umich.edu/OSL/Islam/BurstyTraffic-WP.pdf`. White paper.

[117] X. Zhou, M. Feuer, and M. Birk. "Fast control of inter-channel SRS and residual EDFA transients using a multiple-wavelength forward-pumped discrete Raman amplifier", in *Proc. of Optical Fiber Communications Conference (OFC),* Anaheim, CA, USA, Paper OMN4, 2007.

[118] D. C. Kilper, A. R. Grant, T. K. Ho, T. Salamon, and C. A. White. "Surviving channel dependence of fast power transients in a 109 channel Raman-amplified transmission experiment", in *European Conference on Lasers and Electro-Optics (CLEO-EU),* Munich, Germany, Paper CI7-1-THU, 2007.

[119] A. Scavennec and O. Leclerc. "Toward High-Speed 40-Gbit/s Transponders", *Proceedings of the IEEE*, vol. 94, no. 5, pp. 986–996, 2006.

[120] Y. Liu, C. W. Chow, C. H. Kwok, H. K. Tsang, and C. Lin. "Optical Burst and Transient Equalizer for 10Gb/s Amplified WDM-PON", in *Proc. of Optical Fiber Communications Conference (OFC),* Anaheim, CA, USA, Paper OThU7, 2007.

[121] T. B. Gibbon, A. V. Osadchiy, R. Kjær, J. B. Jensen, and I. T. Monroy. "Gain transient suppression for WDM PON networks using semiconductor optical amplifier", *Electronics Letters*, vol. 44, no. 12, pp. 756–758, June 2008. doi:10.1049/el:20080978.

[122] P. V. Mamyshev. "All-optical data regeneration based on self-phase modulation", in *European Conference on Optical Communication (ECOC), Vol. 1,* pp. 475–476, 1998.

[123] D. Breuer, K. Ennser, and K. Petermann. "Comparison of NRZ- and RZ-modulation format for 40 Gbit/s TDM standard-fiber systems", in *Proc. of European Conference on Optical Communication (ECOC),* Oslo, Norway, Paper TuD3.3, Sep. 1996.

[124] M. Galili, L. K. Oxenløwe, D. Zibar, A. T. Clausen, and P. Jeppesen. "160 gb/s raman-assisted spm wavelength converter", in *European Conference on Optical Communication, ECOC' 04, Post Deadline papers,* Stockholm, Sweden, pp. 28–29, Paper Th4.3.1 (postdeadline paper), Sep 2004.

[125] VPIphotonics. "Home page". `http://www.vpiphotonics.com/`, 2008.

[126] B.-E. Olsson and D. J. Blumenthal. "Pulse Restoration by Filtering of Self-Phase Modulation Broadened Optical Spectrum", *Journal of Lightwave Technology*, vol. 20, no. 7, pp. 1113–1117, Jul. 2002.

[127] R. Kjær, L. K. Oxenløwe, B. Palsdottir, and P. Jeppesen. "All-optical equalization of power transients on four 40 Gbit/s WDM channels using a fiber-based device", in *Proceedings of European Conference on Optical Communication, ECOC '08,* Brussels, Belgium, Paper Th.1.B.6, Sep 2008.

[128] S. M. A. Razzak and Y. Namihira. "Proposal for Highly Nonlinear Dispersion-Flattened Octagonal Photonic Crystal Fibers", *IEEE Photonics Technology Letters*, vol. 20, no. 4, pp. 249–251, 2008.

[129] F. Koch, B. Pálsdóttir, J. O. Olsen, T. Veng, B. Flintham, and R. Keys. "30dBm Wideband Air-Clad EDFA Using Two Pump Lasers", in *Proc. of Optical Fiber Communications Conference (OFC),* San Diego, CA, USA, Paper OWU3, 2008.

A. Validation of numerical model

This appendix presents experimental validation for the amplifier model presented in section 2.3. In the following, the model is compared to static results generated by an experimentally validated amplifier model (Raman-OASIX), as well as static experimental data. An experimental comparison of the dynamic model gain was presented in chapter 4 and found to be in good agreement with the experimental data.

A note on Raman-OASIX The in-house amplifier simulation software of OFS Fitel, Raman-OASIX, is an experimentally validated model for calculating static (not time-resolved) gain, noise figure and multi-path interference (MPI) for different pump configurations, fiber types and lengths. Raman-OASIX is also capable of accurate modeling of erbium-doped fiber amplifiers (EDFAs). Raman-OASIX does not support counter-propagating signals. The primary motivation for making our own model has therefore been a wish to investigate dynamic effects from gain and noise transients. Because our model uses the same fiber parameters as Raman-OASIX, static comparisons between the two models is straightforward. Experimental validation of Raman-OASIX can be found in the published literature [54, 55].

A.1. Small-signal parameters

In Fig. A.1 and A.2, our model is compared with Raman-OASIX in the small-signal case where the total input power is less than -20 dBm. 41 channels are used with an input power of -37 dBm/ch and in the wavelength range from 1530 nm to 1570 nm. A single pump at 1453 nm is used with 300 mW input power to backward pump an 80 km TrueWave®REACH (TW-REACH) fiber.

Fig. A.1 compares the small-signal calculated using the two amplifiers. Agreement between the models is quite good and the maximum gain deviation is 0.3 dB. In Fig. A.2 the small-signal noise figure and MPI noise ratio is compared. Here the maximum noise figure and MPI difference is less than 0.1 dB and 0.3 dB, respectively.

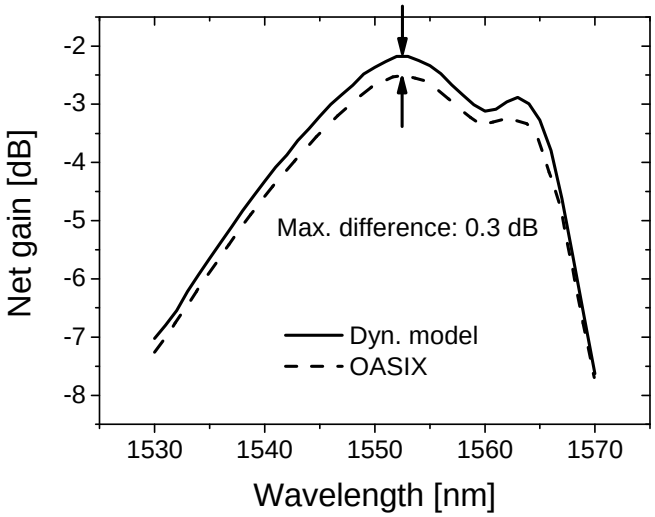

Figure A.1.: Comparison of calculated net gain vs. wavelength in 80 km TW-REACH. The fiber is backward-pumped with 300 mW pump at 1453 nm.

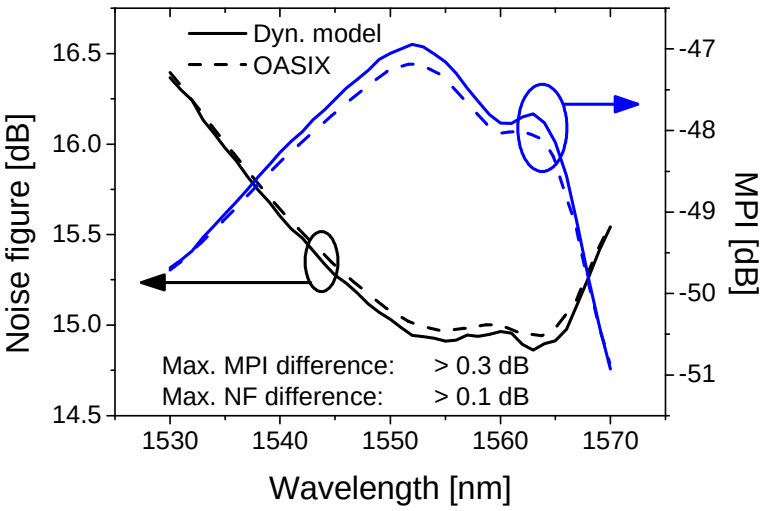

Figure A.2.: Comparison of calculated noise figure and MPI vs. wavelength in 80 km TW-REACH. The fiber is backward-pumped with 300 mW pump at 1453 nm.

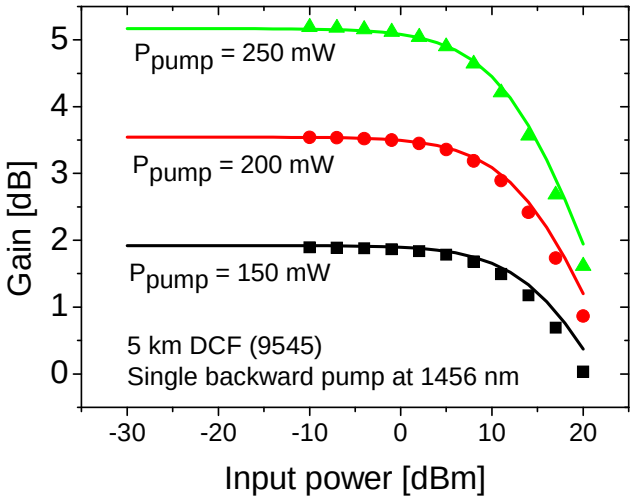

Figure A.3.: Measured (symbols) and modeled (lines) gain vs. input power in a 5 km DCF for SSMF.

A.2. Gain saturation

Fig. A.3, A.4 and A.5 shows plots of saturated gain vs. input power in a 5 km and 10 km dispersion compensating fiber (DCF) for standard single-mode fiber (SSMF). The model data (lines) is compared with experimental data (symbols) for different pump powers and directions. The model pump powers has been fitted so the small-signal gain in the model matches the measured small-signal gain. The model pump powers are generally 20% lower than the experimental pump powers. This difference is most likely due to additional coupling loss in the experimental setup, which is not accounted for. The experimental pump powers are labeled on the figures. No other parameters have been fitted.

Good agreement is found in all three cases between the modeled and measured data.

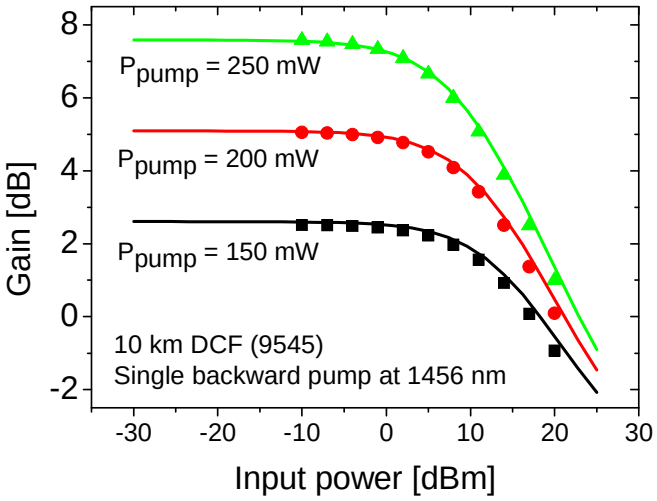

Figure A.4.: Measured (symbols) and modeled (lines) gain vs. input power in a 10 km DCF for SSMF.

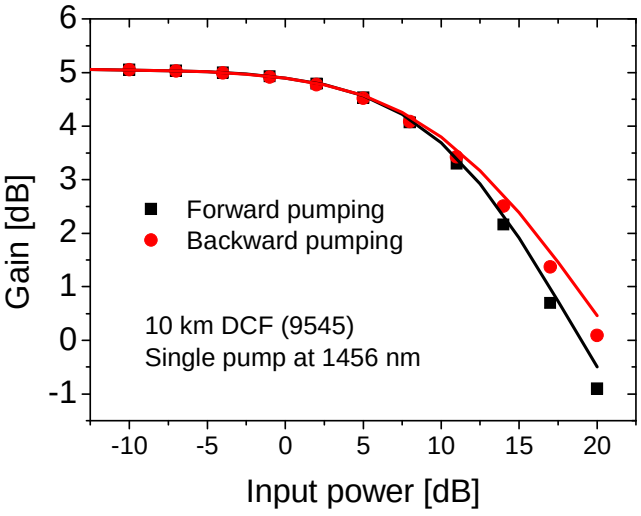

Figure A.5.: Measured (symbols) and modeled (lines) gain vs. input power in a 10 km DCF for SSMF. Black and red lines/symbols correspond to forward and backward pumping, respectively.

B. Fiber parameters

This appendix includes plots of the fiber parameters used in the numerical model, which is described in section 2.3. All parameters are kindly provided OFS Fitel Denmark ApS and have been experimentally characterized at their production facility in Brøndby, Denmark.

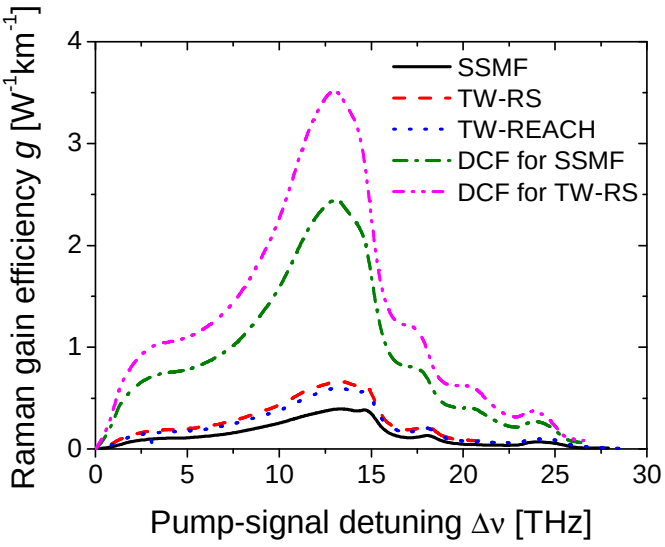

Figure B.1.: Raman gain efficiency vs. pump-signal detuning.

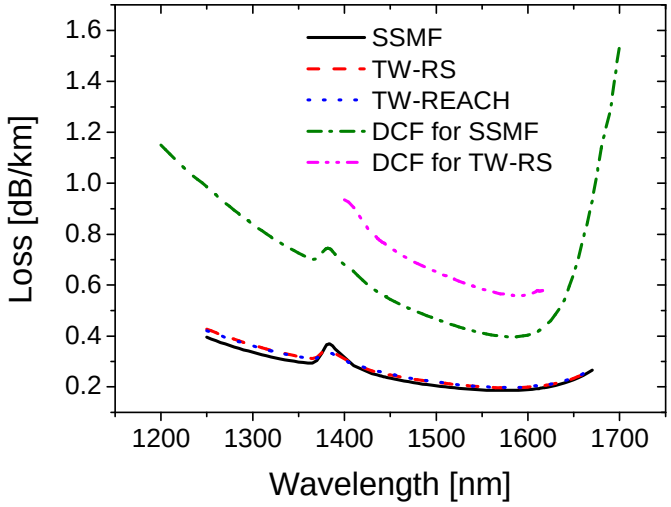

Figure B.2.: Fiber loss vs. wavelength.

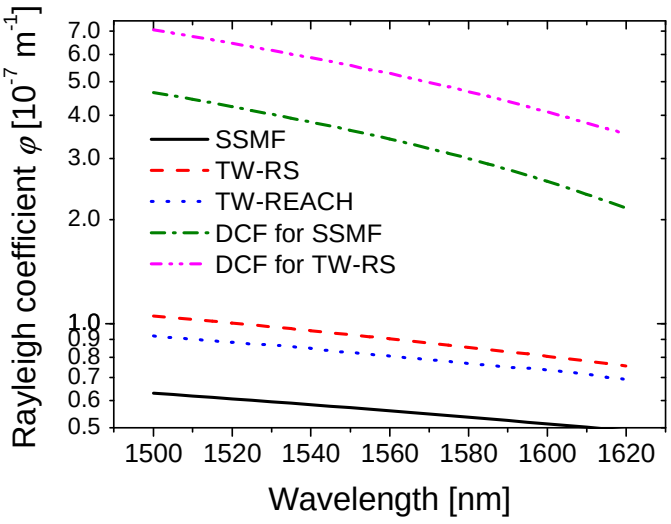

Figure B.3.: Rayleigh backscattering coefficient vs. wavelength.

C. List of acronyms

AOM	acousto-optic modulator
ASE	amplified spontaneous emission
ASK	amplitude-shift-keying
AWG	arrayed waveguide grating
BER	bit-error rate
BERT	bit-error rate testset
BPF	bandpass filter
CLEO	the Conference on Lasers and Electro-Optics
CW	continuous wave
CWDM	coarse wavelength division multiplexer
DCF	dispersion compensating fiber
DCRA	dispersion compensating Raman amplifier
DEMUX	demultiplexer
DFB	distributed feedback
DPSK	differential phase-shift-keying
DRA	distributed Raman amplification
DRB	double Rayleigh backscattering
DS	downstream
EDC	electronic dispersion compensation
EDFA	erbium-doped fiber amplifier
FEC	forward error correction

FRA	fiber Raman amplifier
FSK	frequency-shift-keying
FTTP	fiber-to-the-premises
FWHM	full width at half maximum
GFF	gain flattening filter
GNU	gain non-uniformity
HNLF	highly nonlinear fiber
ITU	the International Telecommunication Union
MPI	multi-path interference
MUX	multiplexer
MZM	Mach-Zehnder modulator
NRZ	non-return-to-zero
NZDSF	non-zero dispersion-shifted fiber
OAA	Optical Amplifiers and Their Applications
ONU	optical network unit
OOK	on-off-keying
OSA	optical spectrum analyzer
OSC	oscilloscope
OSNR	optical signal-to-noise ratio
PC	polarization controller
PD	photodiode
PON	passive optical network
PPG	pulse pattern generator
PRBS	pseudo-random bit sequence
PSD	power spectral density
PSK	phase-shift-keying

Raman-OASIX	reference fiber amplifier model
RIN	relative intensity noise
ROPA	remote optically pumped amplifier
ROADM	reconfigurable optical add/drop multiplexer
RZ	return-to-zero
SBS	stimulated Brillouin scattering
SNR	signal-to-noise ratio
SOA	semiconductor optical amplifier
SPM	self-phase modulation
SRS	stimulated Raman scattering
SSMF	standard single-mode fiber
TF	transmission fiber
TW-RS	TrueWave®RS
TW-REACH	TrueWave®REACH
US	upstream
VOA	variable optical attenuator
WDM	wavelength division multiplexed
XGM	cross-gain modulation

D. List of constants, variables and symbols

D.1. Fundamental constants

Constant	Name	Value
c	Light speed in vacuum	$2.998 \cdot 10^{8}$ m/s
h	Planck's constant	$6.626 \cdot 10^{-34}$ J $\cdot$ s
k_B	Boltzmann's constant	$1.381 \cdot 10^{-23}$ J/K
q	Electron charge	$1.602 \cdot 10^{-19}$ C

D.2. Variables and symbols

α	Loss coefficient (in units of 1/m)
α_{dB}	Propagation loss (in units of dB/km)
γ	Nonlinear coefficient (in units of $\mathrm{W^{-1}km^{-1}}$)
γ_B	Dimensionless parameter
γ_R	Raman gain coefficient (in units of m/W)
λ	Optical wavelength in vacuum (in units of m)
ν	Optical frequency (in units of Hz)
ν_a	Brillouin frequency shift between Stokes and signal beam (in units of Hz)
σ	Standard deviation of intensity noise (in units of W)
ρ_{ASE}	Optical power spectral density of the ASE (in units of W/Hz)
φ	Rayleigh back-scattering coefficient (in units of 1/m)
$\Delta\nu$	Pump-signal detuning (in units of Hz)

$\Delta\nu_B$	FWHM of Brillouin gain (in units of Hz)
$\Delta\nu_{BPF}$	FWHM of band-pass filter (in units of Hz)
$\Delta\nu_n$	Pump and spontaneous emission detuning (in units of Hz)
Δf	Noise bin width (in units of Hz)
g	Raman gain efficiency (in units of $\mathrm{W^{-1}km^{-1}}$)
g_B	Brillouin gain coefficient (in units of m/W)
h	Modulation index
n_2	Nonlinear index of fiber (in units of $\mathrm{m^2/W}$)
r	Radial distance (in units of m)
z	Longitudinal fiber coordinate (in units of m)
A_{eff}	Effective mode area (in units of $\mu\mathrm{m}^2$)
A^R_{eff}	Raman spatial overlap - between pump and signal (in units of $\mu\mathrm{m}^2$)
B	Noise bandwidth for OSNR evaluation (in units of Hz)
C	Constant
D	Chromatic dispersion coefficient (in units of ps/nm/km)
E	Energy (in units of J)
F	Noise figure
G	Amplifier net gain
G_i	Single-pass gain of section i
G_0	Small-signal gain
G_{on-off}	Amplifier on-off gain
I	Irradiance or intensity (in units of $\mathrm{W/m^2}$)
L	Length of fiber (in units of m)
L_{eff}	Raman effective length (in units of m)
L^R_{eff}	Effective nonlinear Raman length (in units of m)

L_{opt}	Optimum Raman length of fiber (in units of m)
N	No. of spans
P	Power (in units of W)
P_{th}	Brillouin threshold input power (in units of W)
Q	Parameter
R	Reflectivity of fiber connection
S	Chromatic dispersion slope (in units of ps/nm^2/km)
S_{21}	Cross-gain response parameter
T	Temperature (in units of K)
FOM_R	Raman figure-of-merit (in units of $W^{-1}dB^{-1}$)
$OSNR$	Optical signal-to-noise ratio
SNR	Electrical signal-to-noise ratio

D.3. List of sub- and superscripts

i	Amplifier section
n	Noise bin
p	Pump-wave
s	Signal- or Stokes-wave
t	Sampling time
amp	Amplitude
av	Average
bi	Bi-directional
in	At amplifier/fiber input
min	Minimum
max	Maximum
out	At amplifier output

rec	At receiver
ref	Reflected
sat	Saturation power
uni	Uni-directional
BPF	Of band-pass filter
$+$	Forward propagating
$-$	Backward propagating
1	One bit
0	Zero bit

E. List of publications

[I] R. Kjær and L. K. Oxenløwe. A method for equalization of transients in an input optical signal. *Submitted EU and US patent application*, August 2008.

[II] Timothy B. Gibbon, Alexey V. Osadchiy, Rasmus Kjær, Jesper B. Jensen, and Idelfonso Tafur Monroy. Gain Transient Control in Optical Networks using Semiconductor Optical Amplifiers. Submitted to Journal of Optical Networking, May 2008.

[III] R. Kjær, L. K. Oxenløwe, B. Palsdottir, and Palle Jeppesen. All-optical equalization of power transients on four 40 Gbit/s WDM channels using a fiber-based device. In *Proceedings of European Conference on Optical Communication, ECOC '08*, paper Th.1.B.6, Brussels, Belgium, September 2008.

[IV] T. B. Gibbon, A. V. Osadchiy, R. Kjær, J. B. Jensen, and I. T. Monroy. Gain transient suppression for WDM PON networks using semiconductor optical amplifier. *Electronics Letters*, 44(12):756–758, June 2008.

[V] Idelfonso Tafur Monroy, Rasmus Kjær, Filip Öhman, Kresten Yvind, and Palle Jeppesen. Distributed fiber Raman amplification in long reach PON bidirectional access links. *Optical Fiber Technology*, 14(1):41–44, 2008.

[VI] Rasmus Kjær, Bera Palsdottir, Leif K. Oxenløwe, and Palle Jeppesen. Applications of Dispersion Compensating Raman Amplifiers. In *Proceedings of SPIE*, volume 6781, page 67810W, Wuhan, China, Nov. 2007. SPIE. APOC 07, Invited.

[VII] Idelfonso Tafur Monroy, Rasmus Kjær, Jorge Seoane, Filip Öhman, Kresten Yvind, Kamau Prince, and Palle Jeppesen. Long reach PON links for metro and access convergence. In *Proceedings of Asia-Pacific Optical Communications (APOC)*, pages 6783–94, Wuhan, China, Nov. 2007. SPIE. Invited.

[VIII] Rasmus Kjær, Idelfonso Tafur Monroy, Leif K. Oxenløwe, Palle Jeppesen, and Bera Palsdottir. Impairments due to Burst-Mode Transmission in a Raman-based Long Reach PON Link. *IEEE Photonics Technology Letters*, 19(19):1490–1492, Oct. 2007.

[IX] Rasmus Kjær, Idelfonso Tafur Monroy, Jesper Bevensee Jensen, Leif K. Oxenløwe, Palle Jeppesen, and Bera Palsdottir. Performance Impairments due to Gain Transients in a Raman-based Bi-directional Long-reach PON Link. In *Proceedings of CLEO®/Europe - IQEC 2007*, Munich, Germany, paper CI7–2–THU, June 2007.

[X] Jesper Bevensee Jensen, Idelfonso Tafur Monroy, Rasmus Kjær, and Palle Jeppesen. Reflective SOA re-modulated 20 Gbit/s RZ-DQPSK over distributed Raman amplified 80 km long reach PON link. *Optics Express*, 15(9):5376–5381, April 2007.

[XI] Rasmus Kjær, Idelfonso Tafur Monroy, Bera Palsdottir, Leif K. Oxenløwe, and Palle Jeppesen. Bi-directional 120 km long-reach PON link based on distributed Raman amplification. In *Proceedings of IEEE Lasers and Electro-Optics Society Annual Meeting, LEOS' 06*, paper WEE3, Montreal, Canada, October 2006.

[XII] Idelfonso Tafur Monroy, Filip Öhman, Kresten Yvind, Rasmus Kjær, Christophe Peucheret, A. M. J. Koonen, and Palle Jeppesen. 85 km long reach PON system using a reflective SOA-EA modulator and distributed Raman fiber amplification. In *Proceedings of IEEE Lasers and Electro-Optics Society Annual Meeting, LEOS' 06*, paper TuDD4, Montreal, Canada, October 2006.

[XIII] Filip Öhman, Rasmus Kjær, Lotte Jin Christiansen, Kresten Yvind, and Jesper Mørk. Steep and Adjustable Transfer Functions of Monolithic SOA-EA 2R-Regenerators. *IEEE Photonics Technology Letters*, 18:1067–1069, 2006.

[XIV] Idelfonso Tafur Monroy, Rasmus Kjær, A. M. J. Koonen, Bera Palsdottir, and Palle Jeppesen. 10 Gb/s bidirectional single fibre long reach PON link with distributed Raman amplification. In *Proceedings of European Conference on Optical Communication, ECOC' 06*, paper We3.P.166, Cannes, France, September 2006.

[XV] Rasmus Kjær, Bera Palsdottir, Carsten G. Jørgensen, Leif K. Oxenløwe, and Palle Jeppesen. Hybrid Erbium/Raman Fiber Amplifier with High Dynamic Range and Low Gain Ripple in Entire C-band. In *Proceedings of Optical Amplifiers and Their Applications, OAA 2006*, paper JWB40, Whistler, Canada, June 2006.

[XVI] Rasmus Kjær, Michael Galili, Leif K. Oxenløwe, Carsten G. Jørgensen, and Palle Jeppesen. Raman-assisted transmission of 16×10 Gbit/s over 240 km using post-compensation only. In *Proceedings of Conference on Lasers and Electro-Optics, CLEO '06*, paper CThP4, Long Beach, USA, May 2006.

[XVII] Jesper Mørk, Rasmus Kjær, Mike van der Poel, and Kresten Yvind. Slow light in a semiconductor waveguide at gigahertz frequencies. *Optics Express*, 13:8136–8145, 2005.

[XVIII] Jesper Mørk, Filip Öhman, Rasmus Kjær, and Kresten Yvind. Nonlinear saturation dynamics and its application to all-optical regeneration and light slow-down. In *Workshop on Nonlinear Dynamics in Photonics*, Berlin, Germany, 2005.

[XIX] Jesper Mørk, Rasmus Kjær, Mike van der Poel, Leif K. Oxenløwe, and Kresten Yvind. Experimental demonstration and theoretical analysis of slow light in a semiconductor waveguide at GHz frequencies. In *Proceedings of Conference on Lasers and Electro-Optics, CLEO '05*, paper CMCC5, Baltimore, MD, USA, May 2005.

[XX] Jesper Mørk, Rasmus Kjær, Mike van der Poel, and Kresten Yvind. Light slow-down in semiconductor waveguides due to population pulsations. In *CLEO/Europe-EQEC '05*, Munich, Germany, paper EA3–5–WED, 2005.

[XXI] Lotte Jin Christiansen, Filip Öhman, Rasmus Kjær, Jesper Mørk, and Kresten Yvind. Measurement and Modeling of the Transfer Function of a Monolithic SOA-EA 2R-Regenerator. In *Proceedings of Conference on Lasers and Electro-Optics, CLEO '05*, paper CMGG5, Baltimore, MD, USA, May 2005.